Synthesis and Application of Porphyrin, Phthalocyanine and Perylene Chromophores for Solar Energy Conversion

by

Jesse J. Bergkamp

A Dissertation Presented in Partial Fulfillment
of the Requirements for the Degree
Doctor of Philosophy

Approved July 2013 by the
Graduate Supervisory Committee:

Ana Moore, Co-Chair
Ernesto Mariño-Ochoa, Co-Chair
Devens J. Gust
Ian Gould

ARIZONA STATE UNIVERSITY

August 2013

ABSTRACT

Photosynthesis, one of the most important processes in nature, has provided an energy basis for nearly all life on Earth, as well as the fossil fuels we use today to power modern society. This research aims to mimic the photosynthetic process of converting incident solar energy into chemical potential energy in the form of a fuel via systems capable of carrying out photo-induced electron transfer to drive the production of hydrogen from water. Herein is detailed progress in using photo-induced stepwise electron transfer to drive the oxidation of water and reduction of protons to hydrogen. In the design, use of more blue absorbing porphyrin dyes to generate high-potential intermediates for oxidizing water and more red absorbing phthalocyanine dyes for forming the low potential charge needed for the production of hydrogen have been utilized. For investigating water oxidation at the photoanode, high potential porphyrins such as, bis-pyridyl porphyrins and pentafluorophenyl porphyrins have been synthesized and experiments have aimed at the co-immobilization of this dye with an IrO_2-nH_2O catalyst on TiO_2. To drive the cathodic reaction of the water splitting photoelectrochemical cell, utilization of silicon octabutoxy-phthalocyanines have been explored, as they offer good absorption in the red to near infrared, coupled with low potential photo-excited states. Axially and peripherally substituted phthalocyanines bearing carboxylic anchoring groups for the immobilization on semiconductors such as TiO_2 has been investigated. Ultimately, this work should culminate in a photoelectrochemical cell capable of splitting water to oxygen and hydrogen with the only energy input from light. A series of perylene dyes bearing multiple semi-conducting metal oxide anchoring groups have been synthesized and studied. Results have shown

interfacial electron transfer between these perylenes and TiO_2 nanoparticles encapsulated within reverse micelles and naked nanoparticles. The binding process was followed by monitoring the hypsochromic shift of the dye absorption spectra over time. Photoinduced electron transfer from the singlet excited state of the perylenes to the TiO_2 conduction band is indicated by emission quenching of the TiO_2-bound form of the dyes and confirmed by transient absorption measurements of the radical cation of the dyes and free carriers (injected electrons) in the TiO_2.

DEDICATION

I dedicate this dissertation to my wonderful parents, Pam and Delmar.

ACKNOWLEDGMENTS

There are so many people I would like to acknowledge for helping me through my graduate career. I must start with my advisors, Ana Moore, Tom Moore, Devens Gust and Ernesto Marino-Ochoa. Your wisdom, patience, and thought provoking questions have been catalysts for my success in graduate school. Thank you for your constant motivation, not just to get scientific results from the laboratory but also to improve myself as a scientist.

I must thank Mike Hambourger and Gary Moore for helping me in my beginning days of graduate school. You guys made the transition from undergraduate to graduate school smooth for me. Special thanks to Mike Hambourger who taught me how to be an open-minded scientist and find the elegance in all areas of science. I must acknowledge Gary Moore for being a spokesperson between The Evergreen State College and Arizona State University to aid in my acceptance here.

A very special thanks to Smitha Pillai, my "Big Sister." Your kindness and understanding is greater than that of anyone else I've ever met. You made the lab an enjoyable, exciting and productive place to be. Thank you for the many conversations, not only about chemistry but family, friends, past stories and more. Some of my favorite times were when we would share different foods from one side of the lab to the other, followed by discussions about the nutritional value and prices. Your humbleness helped motivate me as a young chemist by providing me with an environment where I could help a senior scientist and in turn help mature my confidence. Thank you for being a stand-in alarm clock and waking me up in time for class after the long nights in lab. Smitha, I'm off for teasers!

When I think of Dr. Peter J. Pessiki I think of a man, who in a sense, saved me. The road I was on before joining your class/lab was bumpy but because your love and enthusiasm for chemistry is so contagious I was able to get on the path of success. For this, I am forever indebted. The teachings of chemistry and work ethics you passed on to me have been invaluable during my time in graduate school; what a long strange trip it's been!

I would like to thank my physics/mathematics professor Mario Gadea for taking extra time to help me. Your dedication to your students is exceptional. I would have never found out that physics and IPA go together so well if it weren't for you. Thanks for the many glasses of wine, beer and cigars that we shared.

I would like to thank Paul Liddell for helping me with so many chemistry questions throughout the years. Your expertise in organic synthesis is exceptional and has motivated me to push myself as a synthetic chemist. You have taught me how to execute and appreciate elegant chemistry. I enjoyed trying to guess the "tool of the week" and talking metal shop with you.

Thank you Yuichi Terazono, Gerdenis Kodis and Sandip Shinde, for your intellectual aid ranging from synthesis to photo-physics, and biochemistry. I learned so much from you guys that I would not of otherwise, if I had not spent time with you.

I would like to extend my gratitude to my collaborators Gonzalo Cosa and Rodrigo Palacios for years of fruitful research.

A special thanks goes to Matthieu Koepf for honing my chemistry skills. Your knowledge is impressive and I strive to attain as much. Thank you for helping me through the many long days and nights with fruitful conversations and good cheese or at least

telling me about good cheese. I enjoyed working through difficult synthetic schemes and testing them in the lab. You have taught me many synthetic skills that I utilized and will continue to use in the future. I will always consider you as a true friend.

I want to extend my deepest thanks to Ben Sherman, Chris Madden, Michael and Natalie Vaughn, Dustin Patterson, Jim Bridgewater, Jeff Crisman, Anindya Roy, Manuel Portolés, and Kim Rendek for being the greatest friends that one can have. You all have made graduate school bearable with your support, kindness, and understanding, as well as your excellent beer drinking capabilities. I have really enjoyed learning the many different topics of chemistry and life that each of you has to offer. I consider all of you part of a new family and hope that we will always stay in touch.

I would like to thank Chelsea Brown for being such a helpful lab partner. You have helped me fine-tune my teaching of chemistry. Your willingness and excitement to learn chemistry indirectly helped motivate me to learn more chemistry. You helped me to find time for myself and to get out of lab every once in awhile. For this, I thank you. Thank you to all the current and past members of the Gust/Moore/Moore group.

Julie Holder, I would like to thank you for your steadfast support and encouragement throughout my graduate carrier.

I want to give a very, very special thanks to my parents, Pam and Delmar for their unending support, compassion and encouragement. Thank you for your constant curiosity about what I'm doing even though you don't understand all of the scientific mumble. Your extremely unscientific suggestions/view-points regarding science have kept me grounded and aware that science is filled with unscientific solutions. I want to thank my brother Jude and his wife Emma for being such wonderful role models in my life. My

family in India has always been such high supporters of me. For this, I thank you all. Thank you Uncle Tim for our early morning/lunch phone conversations about anything under the sun/son. I love you all!

TABLE OF CONTENTS

APPENDIX Page

LIST OF TABLES

Table Page

LIST OF FIGURES

Figure Page

Figure Page

Chapter 1

BACKGROUND

1.1 Natural Photosynthesis

Oxygenic photosynthesis is a natural energy transduction process observed in plants, algae and cyanobacteria. This process converts solar energy into chemical energy through multiple light absorption and electron transfer steps, resulting in the formation of carbohydrates and other energy rich molecules. One of the byproducts of photosynthesis is oxygen (O_2). The release of O_2 into the atmosphere had great effects on the biology of earth since it converted the atmosphere from anaerobic to aerobic. The efficiency of metabolism increased dramatically with the presence of oxygen, since aerobic respiration provides approximately 18-fold more cellular energy than anaerobic respiration [1]. An aerobic atmosphere also allowed the formation of the ozone layer, which protects the earth's surface from harmful UV radiation. Moreover, oxygenic photosynthesis allows sunlight to serve as the primary energy input for life on planet Earth, as well as the primary energy source for the fuels used to power human societies. Nature has engineered multiple enzymes, protein complexes and small molecules in such a way that photoinduced electron transfer steps can take place within protein matrices and form carbohydrates (sugar) and oxygen from water and carbon dioxide with the only energy input coming from the sun [2].

At the heart of these photoinduced electron transfer processes are two enzymes know as Photosystems one (PSI) and two (PSII). Both of these enzymes are made up of multiple subunits, which form a scaffold for the reaction centers within PSI and PSII.

Both PSI and PSII have separate chromophores known as P680 and P700, respectively, which are responsible for the primary photochemical events leading to redox chemistry. The essence of photosynthetic energy conversion is the transfer of an electron from the excited P680 and P700 reaction centers to acceptor molecules in the PSII and PSI pigment-protein complexes[3]. In each case, the protein matrix holds specific cofactors in precise positions and orientations to facilitate these processes. The photon absorption required to drive photosynthesis occurs through antenna systems housed in both PSII and PSI complexes, as well as associated antenna proteins. Antenna chromophores serve to gather sunlight and transfer the energy to the reaction center via singlet-singlet energy transfer [4-6]. Upon photo excitation, the reaction center produces a charge-separated state consisting of an oxidized electron donor molecule and a reduced electron acceptor molecule [7]. The arrangement of cofactors within PSII and PSI allows subsequent dark electron transfer reactions to stabilize the charge-separated state both spatially and temporally. This charge stabilization facilitates sequential electron transfers through PSII, the cytochrome b6f complex, and PSI, allowing photon energy to drive dark redox processes that result in stored chemical energy.

An initial understanding of photosynthetic electron transfer can begin from examining PSII. PSII contains a redox active chlorophyll known as P680. Upon absorption of a photon, P680 is excited from the ground state to produce $P680^*$ and subsequently transfers an electron to acceptors, these acceptors being pheophytin and quinones, resulting in $P680^+$. The electron provided by P680 in PSII is transferred via quinone and plastocyanine electron carriers to PSI for the reduction of the oxidized $P700^+$ reaction center [3]. Within PSI excitation of P700 is followed by electron transfer in much

the same way as in PSII. However, downstream from PSI the electron is used to reduce $NADP^+$ (nicotinamide adenine dinucleotide phosphate) to NADPH, and subsequently to fix CO_2. This stands in contrast to the electron transfer pathway in PSII, where the oxidized $P680^+$ is used to abstract an electron from a tyrosine-histidine pair, then from a tetra-manganese cluster, and ultimately from water.

The electrons that reduce $P680^+$ ultimately come from the oxidation of water, the overall chemical equation that describes the oxidation of water is given in (eqn. 1) [8].

$2H_2O \rightarrow O_2 + 4H^+ + 4e^-$ (Eqn. 1)

Upon reduction of $P680^+$ back to its ground state, the system is capable of repeating the above light absorption and electron transfer steps.

Photosystem II

Within the thylakoid membranes of plants, algae and cyanobacteria is embedded the multi-subunit enzyme, photosystem II. Photosystem II has existed for approximately 2.5 billion years and has stood up to the test of time with its function and structure remaining nearly constant. Its remarkable photoinduced water oxidation capabilities have changed the biology of earth over time [1]. Before PSII, biology was forced to utilize less abundant hydrogen/electron donors such as H_2S, NH_3, organic acids and Fe^{2+} for cellular metabolism [1]. With an almost unlimited supply of water coming from the earth's oceans, PSII found a plentiful substrate to use as an electron donor. Utilizing the energy from light this enzyme catalyzes the chemically and thermodynamically demanding reaction of water splitting. PSII uses the electrochemical potential generated by absorption of four photons to oxidize the very stable water molecule, which requires 810 mV per electron under standard state conditions (pH 7.0) vs. NHE [9].

The dimeric PSII supercomplex contains monomers made of approximately 19 different subunits (depending on species) and containing 57 different cofactors [1] . The oxygen evolving complex (OEC) contains a cluster of four Mn ions and a Ca^{2+} ion, surrounded by amino acid side chains that most likely form direct ligands to the Mn ions. The structure of the Mn cluster is an intensely studied topic in the field of photosynthesis, as deciphering the structure in the natural system would aid in the ability to mimic the water splitting reaction for artificial solar energy conversion.

PSII has multiple co-factors housed at precise locations within a multi-subunit protein structure. It has two plastoquinones Q_A and Q_B (figure 1, green), two pheophytins *a* $Pheo_{D1}$ and $Pheo_{D2}$ (figure 1, brown), two chlorophyll *a* monomers Chl_{D1} and Chl_{D2} (figure 1, cyan), and a chlorophyll *a* dimer $P_{D1}P_{D2}$ (figure 1, cyan), two redox active tyrosines Y_Z and Y_D and histidine residues (figure 1, yellow, Y_D is not shown) and a tetranuclear manganese cluster (figure 1, gray, red and pink).

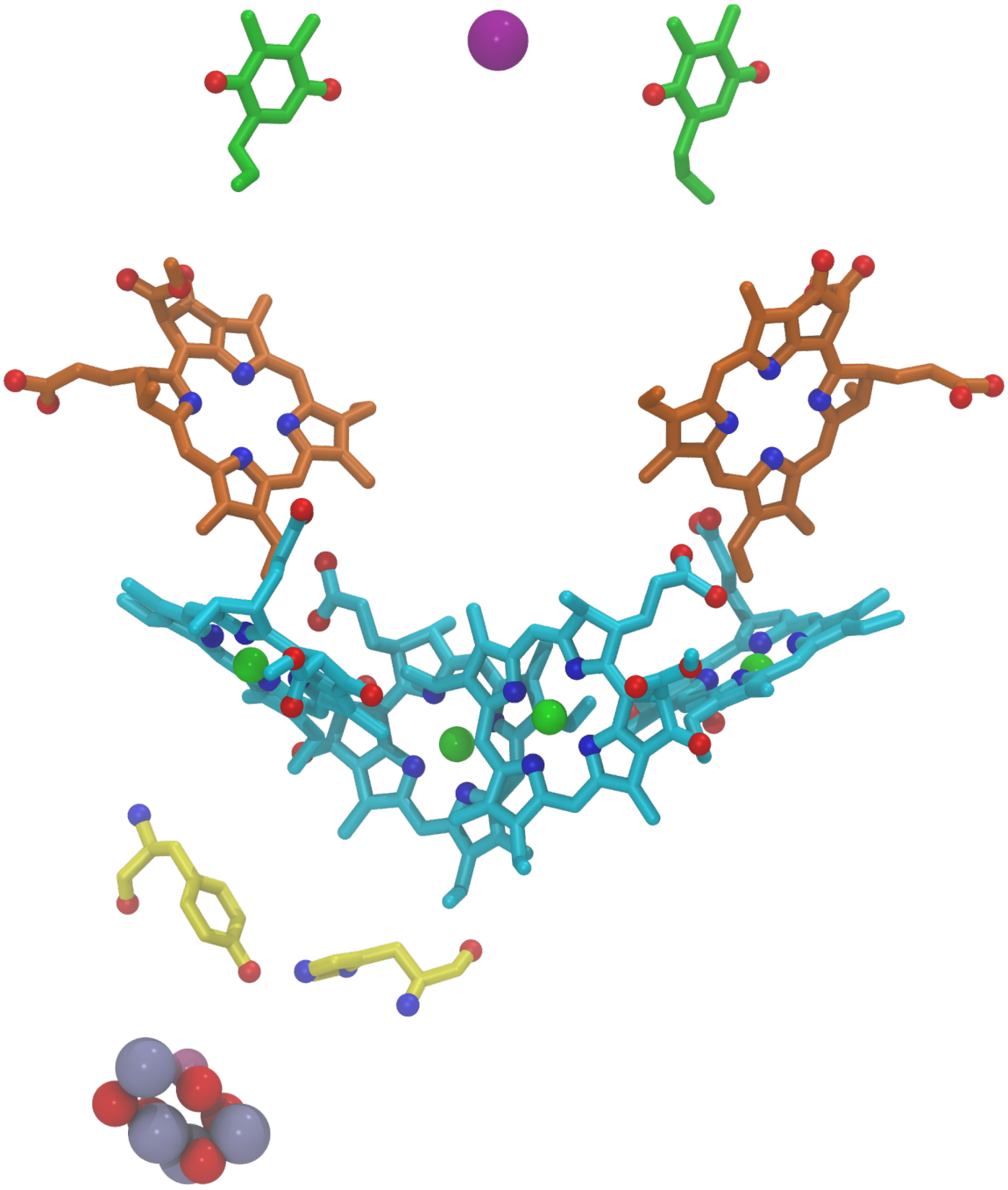

Figure 1: Molecular model of the PSII reaction center. The reaction center has a vertical pseudo-C_2 axis of symmetry. The purple sphere represents the non-heme iron. The two plastoquinones (Q_A and Q_B) are seen in green with their aliphatic chains removed for clarity. In brown are two pheophytins *a* ($Pheo_{D1}$ and $Pheo_{D2}$) with their aliphatic chains

removed for clarity. In cyan, are the two chlorophyll *a* monomers (Chl_{D1} and Chl_{D2}), and a chlorophyll *a* dimer ($P_{D1}P_{D2}$), these two chlorophylls are often referred as the special pair or P680. The redox active tyrosine (Tyr160) and histidine (His190) are seen in yellow, for clarity the tyrosine and histidine found on the D2 side (right side) have been omitted. Manganese atoms (gray), oxygen atoms (red) and one calcium atom (pink) make up the Mn_4CaO_5 cluster. Molecular model made by Michael Vaughn.

All of these cofactors reside in two homologous proteins known as D1and D2 (D for 'diffuse' bands on polyacrylamide gels), which each have five transmembrane α-helices [10]. These two proteins are similar to the L and M subunits that make up the reaction center (RC) in purple photosynthetic bacteria [10,11]. The D1 subunit contains the Mn cluster (figure 1, grey) that is the site for water oxidation [12]. A photon is absorbed by a redox-active chlorophyll dimer (P680, figure 1, cyan), exciting the chlorophyll from its ground state to a higher energy state known as the excited state. The electron is now a strong reductant and subsequently transferred to a nearby acceptor and some argue this acceptor is the $Pheo_{D1}$ (figure 1, brown, left side) based on spectroscopic signals (ENDOR, Resonance Raman and FTIR) [13,14]. The $Pheo_{D1}$ is in close proximity to the quinone Q_A (figure 1, green, left side). There is disagreement on the question of which chlorophyll absorbs the photon, P_{D1} or Chl_{D1} although several groups have proposed that the charge separation is initiated on Chl_{D1} rather than on either P_{D1} or P_{D2}. [9,15,16]. One result that supports this idea is the detection of $Pheo^-$, formed in the initial radical pair state, prior to the detection of P_{680}^+ [17,18]. The resulting charge separation is most likely stabilized by successive electron transfer steps in which multiple redox centers are used. The oxidation of water to oxygen is a four-electron process while the charge separation described above is a one-electron process, therefore a charge storage mechanism is required in PSII. The accumulation of four oxidizing equivalents takes place in the OEC. This catalytic site contains four Mn ions, a Ca^{2+} ion and oxygen atoms given by the formula (Mn_4CaO_5). It also contains chloride ions, as determined by Umena et al. who reported a 1.9Å crystal structure for the Mn cluster [12]. The Mn atoms and one Ca ion are coordinated by μ-oxo bridges and amino-acid residues [12]. Once four oxidative

equivalents are collected on the Mn cluster, the four-electron oxidation of water to oxygen can occur.

The charge storage mechanism was studied by Kok et al. who first reported a model consisting of five oxidation states of the OEC (S_0, S_1, S_2, S_3, S_4) [19,20]). Four successive light reactions are responsible for the four oxidations between the S_0 and S_4 states. When the S_4 state is achieved, an oxygen molecule is produced and released, thereby regenerating the S_0 state. The early experiments conducted by Joliot and Kok et al. showed that the S_1 state is the dark stable state. They achieved this by using extremely sensitive electrochemical methods that could detect the presence of oxygen produced in a single flash of light. The result that they observed showed that PSII required three flashes of light to produce oxygen. After the first cycle, it then took four flashes of light to produce oxygen. These results support the five state mechanism. As the S states proceed from S_0 to S_4 the OEC is successively more oxidized until sufficient oxidizing equivalents are achieved for the oxidation of water. The redox-active tyrosine (Y161) Y_Z also plays a critical role in the charge build-up of the Mn cluster as it participates in the shuttling of the electrons that reduce $P680^{+\cdot}$. Y_Z also plays a role in proton-coupled electron transfer in certain S state transitions. This is supported by experimental evidence, including the pH-dependence of the redox active Y_Z and nearby residues. This pH dependence is caused by the protonation and deprotonation of the residues, which alters the redox potentials of the residues [8]. After the P680 is oxidized by the initial photochemical step it is re-reduced in tens of nanoseconds by electron transfer from the Y161 of the D1 protein, thus forming a Y_Z radical [3]. The $P680^+$ is the strongest known biological oxidant with a reduction potential around +1.3V vs NHE [8]. Upon photo

excitation of the Chl_{D1}, an electron transfer process takes place forming the radical pair $Chl_{D1}^{+}Pheo_{D1}^{-}$. The $Pheo_{D1}^{-}$ can then donate an electron to the plastoquinone Q_A which shuttles the electron to the second plastoquinone Q_B. Once the plastoquinone gets reduced two times, and accumulates two protons, it leaves the complex as plastoquinol. A non-heme iron (figure 1, purple) with bicarbonate acting as a ligand, is in between these two plastoquinones.

Photosynthesis has been fine tuned throughout history to provide an efficient powerhouse for living organisms. There are a few limitations to this system: (1) when low light conditions exist the photosystems can have a difficult time capturing photons, making the efficiency of fuel production lower, (2) when high light conditions are present, the photosystems can be overloaded with excitation energy leading to the production of deleterious reactive oxygen species (ROS). Nature has developed systems capable of protecting itself from the conditions above, but not necessarily capable of maximizing solar energy harvesting efficiencies. The fuels produced by photosynthesis are sufficient for plants to use for energy, but if one was to look at the fundamental processes of photosynthesis, i e. the electron transfer and charge storage mechanisms we could develop a mimic of a system to produce a more suitable fuel for humans. The fuels we humans use today, such as oil and coal are the decomposed plant materials from millions of years of photosynthesis. Our society is living off of this material and has managed to burn a sizeable percentage of that in a few hundred years. We can't maintain our lifestyle with the low efficiency of natural photosynthesis [21]. Therefore, we must re-engineer the basic concepts of nature to develop artificial systems with efficiencies that are capable of keeping up with societies energy demands.

1.2 Introduction to Research:

The research herein centers on using the fundamental principles of photosynthesis as a blueprint for building artificial constructs that can mimic the natural system for solar energy conversion. Solar energy conversion has been a research topic of interest for quite some time [22], as our dependence on fossil fuels has led to increased atmospheric pollutants such as carbon dioxide, nitrous oxide and others [23] as well as geopolitical disputes. Also, since fossil fuels will not last forever we, as humans, need to find clean, abundant and renewable forms of energy [24]. Solar energy is the most abundant source of energy available to fulfill these needs. In one hour, of the sunlight that strikes the Earth's surface provides $4.3x10^{20}$ J of energy while mankind's current annual consumption is $4.1x10^{20}$ J of energy [25]. This research aims to take the conventional silicon-based solar cell to the next level by having the electrons produced to synthesize a fuel. Silicon solar cells convert solar energy into electrical energy, which is beneficial during the day, but at night, humans still need to power their activities. Silicon-based solar cells are expensive due to the high purity of silicon they require, so switching from silicon to organic based pigments to capture light and inorganic, earth abundant, materials to shuttle electrons, one could achieve similar results but at a lower cost. Grätzel has pioneered this research with the development of a photoelectrochemical cell [26-28] known as the Grätzel cell. If one can store the electron that is generated by such a solar cell, then humans could use it when needed. A possible solution to the storage problem is in the form of chemical bonds. If solar energy can be transformed into chemical potential, it can then be stored within the bonds of a high energy molecule such as hydrogen. This would then provide

humans with a means of obtaining storable and transportable fuels. In order to achieve this, one must consider many redox reactions all working together. As seen in figure 2, it is necessary to choose what kind of organic dyes and semi-conductors to use based on their redox properties in order to drive the catalysis of water oxidation and proton reduction. The use of high potential dyes to drive the catalyst for water oxidation can be seen in figure 2, colored in magenta. One sacrifice by using such dyes is that one is forced to utilize tin oxide (SnO_2) as the semi-conductor, which has fast charge recombination times, instead of titanium dioxide (TiO_2), which has been more widely studied and used for such systems with slower charge recombination times [29-31]. In contrast, with a lower potential porphyrin (as seen in figure 2 colored purple), one can use TiO_2, but now the oxidized porphyrin cannot drive the catalyst seen in blue in figure 2.

Shown in figure 3 is the development of a photoelectrochemical cell that mimics the two photosystems of photosynthesis that is underway. Engineered into the cell (figure 3) are two photocells, one anodic and one cathodic. The anodic side (figure 3, left side) of the cell utilizes more blue absorbing dyes capable of water oxidation, much like PSII. The cathodic side (figure 3, right side) of the cell utilizes a more red absorbing dye capable of driving proton reduction, mimicking PSI.

The design of the water oxidizing cell seen in figure 3 is based on that of Mallouk et al. who used a film of 2,2-bipyridine ruthenium dye stabilized $IrO_2 \cdot nH_2O$ particles on TiO_2 for the light driven oxidation of water [32,33]. Ruthenium dyes have good absorption properties but suffer from some issues, such as low turnover numbers, nucleophilic attack of the oxidized dye, use of rare and expensive metals and fast recombination rates.

Therefore we set out to use porphyrins in place of ruthenium dyes that could remedy these maladies. Porphyrins have high extinction coefficients in the blue region of the solar spectrum, are not susceptible to nucleophilic attack of metal centers. The use of two different chromophores that possess different absorption and electrochemical potentials is one of the main design aspects that make this cell attractive for converting solar energy into a fuel. This design mimics the photosystems found in natural photosynthesis. The dye is adsorbed onto a semi-conducting metal oxide (SnO_2) and to a water oxidation catalyst (IrO_2), all of this is on a 2-D conductive glass plate (FTO). High potential dyes are needed in order to drive the catalyst for photo-induced water oxidation. For this, pyridyl, pentafluorophenyl, and palladium inserted porphyrins have been synthesized [34,35]. A challenge that still remains is in the preparation of the IrO_2-porphyrin complex. Traditionally water-soluble capping molecules, such as malonate, citrate etc., have been used to displace chloride ligands from the precursor K_2IrCl_6 to form IrO_2 colloids.

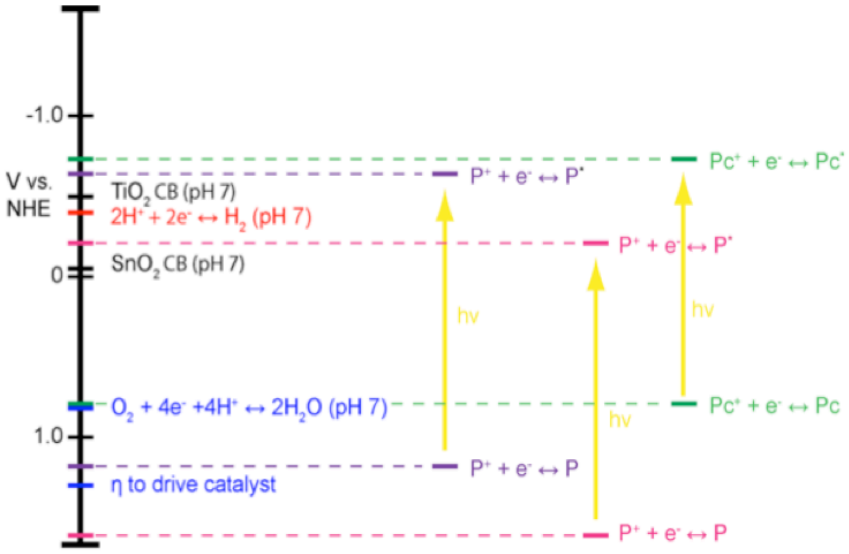

Figure 2: Energy level of the multiple components of the dual-threshold photoelectrochemical cell. Seen in purple are the energy levels for a standard potential porphyrin dye (tetra-malonate porphyrin) [34]. In magenta are the energy levels for a high potential porphyrin dye (pyridyl porphyrin, ~1.4 V vs SCE, unpublished, Bergkamp). In green are the energy levels of a standard octabutoxy phthalocyanine dye (~0.55 V vs SCE) [36]. In black are the conduction bands of TiO_2 and SnO_2 at pH 7 (Potentials re-calculated for pH 7 from pH 1 in reference [26]. The reduction of protons is represented in red and the reduction of oxygen is in blue as well as, the potential needed to drive the IrO_2 catalyst, cyclic voltammetric (CV) measurements (see Fig.2 Pg. 57) where carried out to determine the approximate potential shown and see ref .

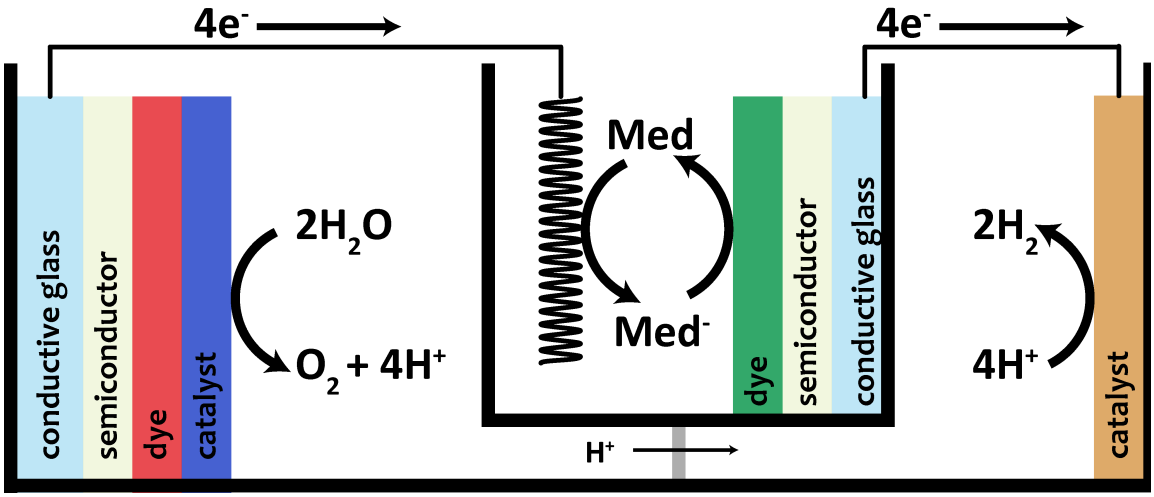

Figure 3: Schematic representation of the desired dual-threshold photoelectrochemical cell. The red bar represents a short wavelength absorbing (~420 nm), high potential porphyrin for driving a water oxidation catalyst (IrO_2) represented by the blue bar. The green bar represents a long wavelength absorbing (~800 nm), low potential phthalocyanine for driving the reduction of protons. The first iteration of the cell will use platinum for the proton reduction catalyst; the gold bar represents this. The mediator in the center cell (Grätzel type) is iodine/triiodide, although one could substitute this with a more negative mediator such as cobalt bipyridyl complexes [37]. Figure made by Benjamin Sherman.

The challenge lies in synthesizing water soluble, high potential porphyrins that will undergo the same reaction as malonate and other small molecule capping groups. We have utilized pyridyl porphyrins to solve this issue. The pyridyl functionality provides both electron withdrawing and, if alkylated, water solubility properties. The synthetic procedure to produce such a porphyrin is seen in scheme 1, unpublished section. It has been shown that phosphonate groups preferentially bind to TiO_2 and the malonate shows binding preference to $IrO_2 \cdot nH_2O$ [32,38]. Therefore, compounds **1**-**7** (scheme 1, Chapter 5) were the starting materials to yield porphyrin **8** (Chapter 5) that bears both phosphonate and malonate functionalities.

For the proton reduction side of the cell, (cathodic, figure 3, right side) red absorbing (~800 nm) and low potential phthalocyanines (figure 2, green) are being utilized. Phthalocyanines (Pc) are similar to porphyrins in that they are classified as a tetrapyrrole, but Pcs have extended aromatic rings on the pyrrolic carbons as well as, nitrogen's at the meso positions. Octabutoxy Pcs were chosen for this application for two main reasons, (1) the butoxy groups at the non-peripheral positions are electron donating making the Pc low potential, (2) butoxy groups in the ortho position help to red-shift the absorption of the Pc out into the near IR region of the solar spectrum [36].

Two different types of semi-conducting metal oxides will be used in the cell. On the anodic side, SnO_2 will provide a more positive conduction band [39] for forward electron transfer from the high potential porphyrin, which in turn, will drive the water oxidation catalyst IrO_2. Unfortunately, this injected electron is not sufficiently reducing to reduce protons to hydrogen. Therefore, we need to increase the energetics of the electron by using TiO_2 that has a more negative conduction band [39]. The cathodic side

will utilize TiO_2 because the Pc dyes will be capable of forward electron injection and subsequently driving the platinum catalyst for proton reduction.

1.3 Journal of Photosynthesis Research Review Paper

Evolution of reaction center mimics to systems capable of generating solar fuel

Benjamin D. Sherman, Michael D. Vaughn, Jesse J. Bergkamp, Devens Gust, Ana L. Moore, Thomas A. Moore.

Department of Chemistry and Biochemistry, Arizona State University, Tempe, AZ 85287

Center for Bio-Inspired Solar Fuel Production, Arizona State University, Tempe, AZ 85287

Center for Bioenergy and Photosynthesis, Arizona State University, Tempe, AZ 85287

Citation:

Sherman, B. D.; Vaughn, M. D.; Bergkamp, J. J.; Gust, D.; Moore, A. L.; Moore, T. A. Evolution of reaction center mimics to systems capable of generating solar fuel. *Photosyn. Res.* **2013**, 1–12.

Phone: 480-965-4547, 480-965-2953, 480-965-3308

Fax: 480-965-5927

Email: gust@asu.edu, amoore@asu.edu, tmoore@asu.edu

URL: http://solarfuel.clas.asu.edu/

My contributions to this work involved figure design, literature research, help with writing the manuscript and aiding in the editing process.

Keywords: Artificial photosynthesis, solar energy conversion, biomimicry, sustainability

Abstract:

Capturing and converting solar energy via artificial photosynthesis offers an ideal way to limit society's dependence on fossil fuel and its myriad consequences. The development and study of molecular artificial photosynthetic reactions centers and antenna complexes and the combination of these constructs with catalysts to drive the photochemical

production of a fuel helps build the understanding needed for development of future scalable technologies. This review focuses on the study of molecular complexes whose design is inspired by the components of natural photosynthesis, and covers research from early triad reaction centers developed by the group of Gust, Moore, and Moore to recent photoelectrochemical systems capable of using light to convert water to oxygen and hydrogen.

Abbreviations:

NPP	net primary production of photosynthesis
HANPP	human appropriation of net primary production of photosynthesis
OEC	oxygen evolving complex
NADPH	nicotinamide adenine dinucleotide phosphate
ATP	adenosine triphosphate
ADP	adenosine diphosphate
P_i	inorganic phosphate
P-Q	porphyrin-quinone
C-P-Q	carotenoid-porphyrin-quinone
C-P-C_{60}	carotenoid-porphyrin-fullerene
BPEA	bis(phenylethynyl)anthracene
NPQ	non-photochemical quenching
DHI	dihydroindolizine
BT	betaine
Tyr_Z-His190	$tyrosine_Z$-histidine190
PCET	proton coupled electron transfer

BiP	benzimidazolephenol
TCNP	tetracyanoporphyrin
FTO	fluorine doped tin oxide
PEC	photoelectrochemical cell
CEPA	2-dicarboxyethylphosphonic acid
Pg	Petagram

Introduction

Human activity and especially our reliance on burning fossil fuels has affected planet wide systems, resulting in a precarious future for the global ecosystem [40]. The magnitude of the energy reaching the Earth from the sun makes solar energy conversion a likely part of any alternative energy future that does not rely on the use of fossil fuel yet still satisfies society's energy demand [41]. The immense scale of solar irradiance, however, means little without an efficient means of converting it to useful forms such as electricity or an energy-dense and transportable fuel. Developing a system for converting an abundant and readily available precursor into a fuel using solar radiation as the sole energy input is the primary goal of artificial photosynthesis [42,43].

The motivation for and possible impact of the wide scale use of artificial photosynthesis to meet human societal energy needs can be illustrated with reference to Fig. 1. Taking into account reflection and absorption of light by the atmosphere, around 65,000 TW reaches the hydrosphere and 15,600 TW reaches land [44]. Photosynthesis converts a portion of this irradiance into energy stored in reduced carbon, with the net amount of biomass produced in a year (net primary production, NPP) totaling ~112 Pg of fixed carbon [45]. Converting this amount of reduced biomass produced per year to a rate of

energy conversion using the conversion factor of 41.3 KJ g^{-1} of fixed carbon [46] yields an average rate of ~156 TW, evenly distributed between terrestrial and marine production [45,47,48]. This biomass in turn supports nearly all life on the planet. Humans consume an increasing portion, currently ~25% [49]. An important issue we face is that human appropriation of net primary production (HANPP) comes at the expense of the remainder of biology, and continued population growth will increase the human demand on NPP for food and material. The conversion of land to support HANPP is thought to be driving several Earth systems over boundaries established by natural cycles operating on the geological time scale [40,50].

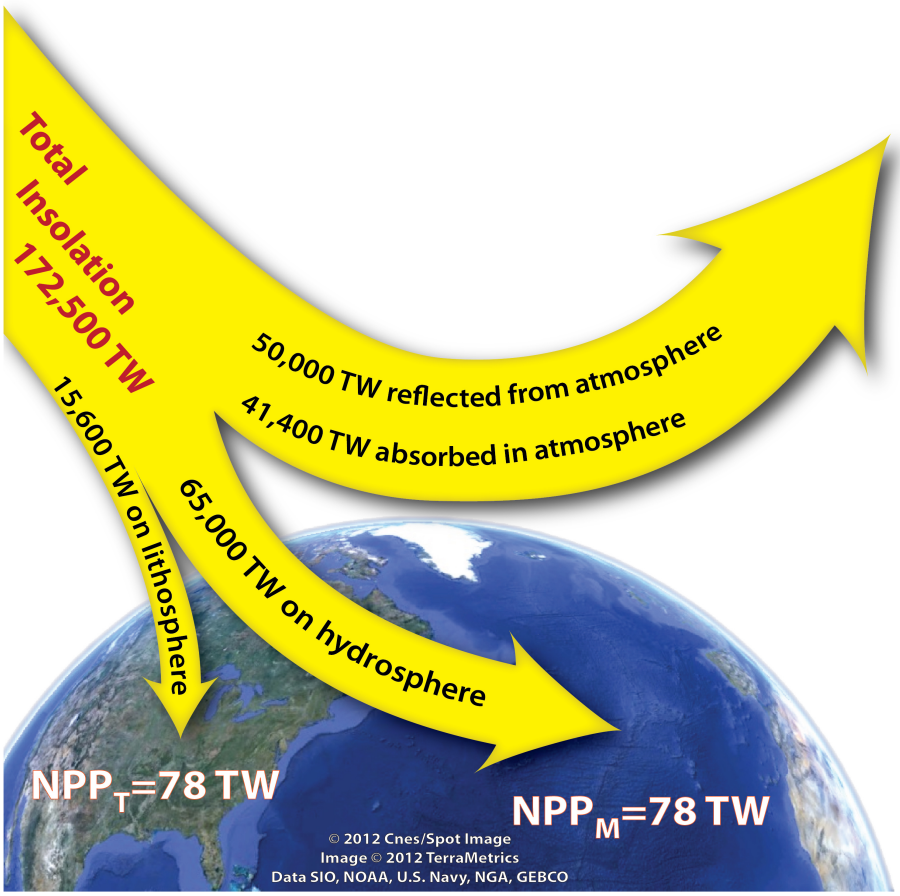

Figure 1: Solar radiation and photosynthetic conversion. Rates of solar energy reaching various portions of the Earth system [44]. While ~80,000 TW reach the surface of the Earth, only 15,600 TW fall on land. About half is within the wavelength range of the photosynthetic pigments; a small fraction of this is stored as chemical energy for the biosphere, i.e. NPP, at an average rate of ~156 TW.

Therefore, any solar-to-fuel system must be vetted against its impact on HANPP; an increase will accentuate an already tenuous ecological situation [40,50]. Figure 2 (see appendix A) outlines energy accounts comparing terrestrial NPP, HANPP, the remainder of NPP after human harvest, and the current non-food energy consumption of modern society. Part (a) illustrates the current state: the human requisition of NPP sums to 20 TW [49]. Driving the global gross domestic product currently consumes ~17 TW, mainly supplied by fossil fuels [51]. Fully displacing fossil fuels with crop-derived biofuel, as shown in (b), must come directly out of NPP. Though carbon neutral, such a scenario is not sustainable as HANPP would increase to nearly 50% NPP. Such a substantial consumption of the total available terrestrial biomass would likely upend the balance of life on the planet as it has been known for the entirety of human existence. Alternatively, as shown in (c), an artificial photosynthetic system (possibly including a synthetic biological organism or photosynthetic microbe whose culture does not displace native organisms or crops) could supply human energy needs while not depleting the biomass needed to support the global ecosystem. We term this converted solar energy APP or artificial photosynthetic production. This situation would have to satisfy several caveats.

For instance any such system should occupy surface area already altered by human activity and minimize the amount of additional land converted for human use. This basic argument seeks not only to focus just on the surface footprint needed to convert solar irradiance to forms of energy usable by humans, but also to consider that any system should not compete for sunlight or land currently used for food production or accessible to nature. To do so will only increase HANPP and further endanger the stability of the global ecosystem.

In order to exceed current productivity without increasing HANPP, the field of artificial photosynthesis seeks the development of solar-to-fuel systems capable of converting light energy to chemical energy stored in a dense, transportable fuel with efficiencies much greater than those of natural photosynthesis. Such a system, as opposed to that of solar-to-electricity (photovoltaic cells), allows for the storage of solar energy and separates its points of generation and utilization in both time and space. As such, artificial photosynthesis can provide a direct substitute for fossil fuels, which are ideal energy carriers with respect to their high energy densities and easy transport. Although designing and constructing such a system comes with enormous challenges, the natural process of oxygenic photosynthesis offers us a guide.

Oxygenic photosynthesis uses the energy of visible light to carry out the oxidation of water and reduction of carbon dioxide to form oxygen and reduced carbon fuel. Absorption of actinic photons by antennas and reaction center pigments of the photosynthetic machinery initiates charge separation and migration in the reaction center, generating spatially separated oxidizing and reducing equivalents. This conversion of solar energy into electrochemical energy is followed by the production of oxygen from water at the oxygen evolving complex (OEC), the generation of reduced nicotinamide adenine dinucleotide phosphate (NADPH), and creation of a proton gradient across the thylakoid membrane. Dissipation of this proton motive force across the membrane produces adenosine triphosphate (ATP) via ATP synthase, and ATP and NADPH then power the dark reactions of the Calvin-Benson cycle leading to the assimilation of CO_2.

Artificial photosynthesis does not seek to reproduce the natural process, but rather to adapt its basic science to meet the needs of humans. Akin to the process of

photosynthesis, an artificial reaction center for solar fuel production needs to absorb light in the visible and near-infrared, generate a charge separated state upon photo-excitation, spatially separate and stabilize the charge separated state, and then transport the photo-generated oxidizing and reducing equivalents to catalysts to carry out the chemical reactions necessary for the production of a fuel (e.g. oxidation of H_2O and production of H_2). Additionally, efficient solar-to-fuel systems incorporating abundant materials are paramount. The study of the underlying photophysical and photochemical processes of model constructs and photoelectrochemical cells will inform the design and aid in the development of such systems.

Much of the research of the Gust, Moore, and Moore group has centered on the development and study of artificial reaction centers with the ultimate objective of constructing solar-to-fuel systems. Here we provide an overview of this work from the first triad reaction centers to the solar water splitting photochemical systems currently under study. The focus of this review is intended as a concise summary of how the group has approached the major challenge of developing sustainable solar energy to fuel technologies, a task that needs input from and is being addressed by many research groups.

Molecular Reaction Centers

An artificial reaction center seeks to perform the same photochemical processes as those observed in the natural system. With the ultimate goal of using light energy to form a fuel, the key functions include: absorption of light across the visible and near-infrared spectra, rapid and efficient transfer of excitation energy from antenna pigments to the reaction center, fast photoinduced charge separation with quantum yields near

unity, and prevention of photodamage. Artificial constructs capable of emulating many aspects of the photosynthetic process have been studied, but developing complete systems capable of efficient conversion of light energy into a fuel remains a challenge. The work outlined below shows a research trajectory aimed at this ultimate goal.

Triad Reaction Centers

Covalently linking two molecular analogues of the cofactors involved in the photosynthetic reaction center (e.g. chlorophylls, carotenoids, pheophytins, quinones) produces some of the simplest artificial reaction centers. Study of porphyrin-quinone (P-Q) constructs in particular guided early work in the field carried out by many different researchers. While a P-Q dyad could form the $P^{\bullet+}$-$Q^{\bullet-}$ charge-separated state with proper illumination, the extremely fast decay of this state limits its usefulness [52]. In the natural system, sequential electron transfer steps following photo-induced charge separation spatially separate positive and negative charges across a substantial distance, which greatly slows recombination. Following this design principle, incorporating a third component, one thermodynamically competent for carrying out a second electron transfer after photo-induced charge transfer, proved essential for prolonging the lifetime of the charge separated state. Synthesis and subsequent study of a carotenoid-porphyrin-quinone triad (C-P-Q) [53] marked a major improvement in stabilizing charge separation in an artificial reaction center and established a platform for engineering improved artificial reaction centers as well as studying other processes characteristic of photosynthesis.

This first triad reaction center, compound **1**, consisted of a ditolylporphyrin covalently bonded via amide linkages to a benzoquinone electron acceptor and a carotenoid secondary electron donor. Molecule **1** and subsequent carotenoporphyrin-

acceptor triads characteristically adopt a linear conformation in solution without folding of the appended groups back over the plane of the porphyrin [53,54]. Transient spectroscopic studies of C-P-Q show that illumination with visible light (600 nm) generates the porphyrin first excited singlet state, C-^{1}P-Q, with a portion of this species then decaying to the first charge separated state, C-P$^{\bullet+}$-Q$^{\bullet-}$. Competing with recombination, a second electron transfer from the carotenoid to the porphyrin radical cation produces the final charge separated state C$^{\bullet+}$-P-Q$^{\bullet-}$. Monitoring the transient absorbance of the oxidized carotenoid moiety (in the 970 nm region) shows that the final charge separated state has a lifetime of 170 ns in dichloromethane, increasing to 2.5 μs in electrolyte-saturated solvent. Table 1 (see Appendix A) contains a summary of the results for **1** and several other reaction centers described herein. The final state preserves 1.1 eV of the 1.9 eV of the porphyrin first excited singlet state [4]. The improved stability of the final charge separated state of this complex relative to those of the preceding dyads resides in the greater spatial separation, and therefore electronic decoupling, of the separated charges and

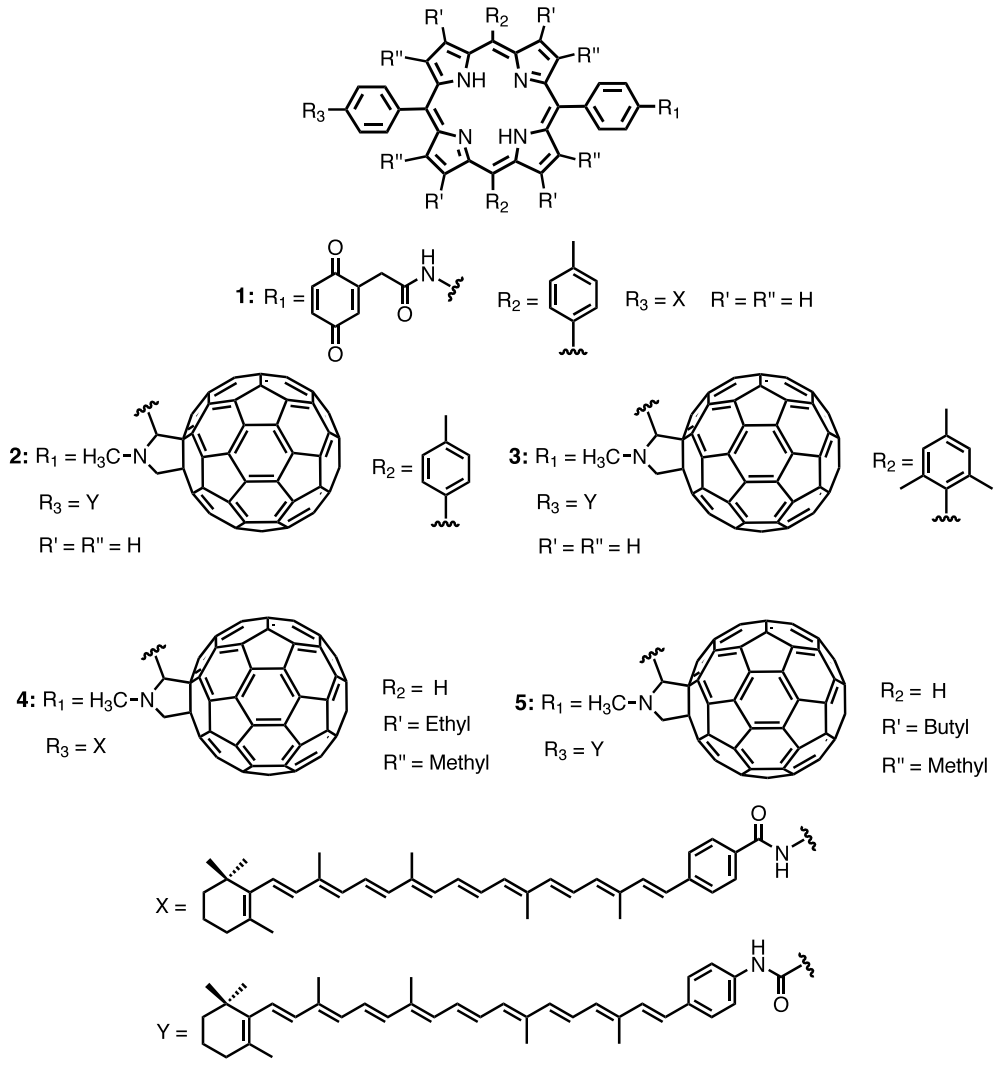

Figure 3: Chemical structures for triad reaction centers **1**-**5**.

the endergonic steps hindering the overall energetically favorable charge recombination.

The C-P-Q triad in turn provided a foundation for further elaboration and improvement in reaction center design and function. Several iterations of the triad reaction center are shown in Fig. 3. Alterations of the electronic coupling, as in changing the orientation of the amide linker in **4** and **5** [55], redox properties [56], and type of acceptor moiety [57,58] in the reaction center led to triad complexes with improved lifetimes and yields of the final charge separated state. The extension of the triad design led to the creation of tetrad and pentad complexes which demonstrated the feasibility of carrying out multiple electron transfer steps across larger complexes resulting in greater spatial separation of the charges and long lifetimes for the charge separated state [59-62].

The introduction of a fullerene electron-accepting unit in place of a quinone advanced the performance of the artificial reaction centers [58]. Although, not observed in any known biological system, the use of a fullerene acceptor moiety offers definite advantages in imitating the photochemical processes observed in natural photosynthesis. With small solvent and internal reorganizational energies upon reduction and relative insensitivity of the radical anion to the solvent dielectric constant compared to quinones, fullerenes perform remarkably well in reaction center constructs [58,63,64]. In comparison with triad complexes employing quinones, those with fullerene acceptor moieties in general show more rapid photoinduced charge separation and slower charge recombination, can perform charge separation in a variety of solvents and even at low temperature in glasses [55,58], and can recombine to triplet excited states rather than the ground state [56,58]. Such behavior is characteristic of the natural system, making fullerenes

an ideal example where compounds alien to biology can substantially aid in the development and performance of overall biomimetic artificial systems [65].

The first iteration of the C-P-C_{60} based triad featuring a β-alkyl substituted porphyrin, **4**, formed the final $C^{\bullet+}$-P-$C_{60}^{\bullet-}$ state with a yield of 0.14 in 2-methyltetrahydrofuran [58]. Spectroscopic studies showed that the decay of this state, with a lifetime of 170 ns, led to the formation of the carotenoid triplet state, ^{3}C-P-C_{60}. Progressive molecular engineering of the complex by introduction of a lower potential carotenoid (compare **4** and **5)** [55], introduction of a ditolylporphyrin in **2** [66], and then dimesitylporphyrin in **3** [56] steadily improved the performance of the reaction center, producing complexes capable of obtaining quantum yields for the final charge separated state near unity. The trajectory of triad reaction centers from the first C-P-Q complexes to the later fullerene-containing analogues demonstrated the ability of synthetic molecular constructs to transform efficiently light energy to chemical potential with charge-separated state lifetimes long enough for conversion of the conserved excitation energy to a useful form, for example by formation of chemical bonds or generation of a pH gradient across a membrane [67,68].

Antenna-Reaction Centers

The single chromophore in a triad reaction center limits the total usable region of the spectrum; nature, by contrast, employs several different pigment molecules such as chlorophylls, carotenoids, cyanobilins, and erythrobilins for wide coverage of the solar spectrum. In the photosynthetic process, antenna pigment-protein complexes absorb most of the actinic light and channel the resultant excitation energy to the reaction center leading to charge separation [3].

In an artificial context, multiporphyrin antenna reaction center complexes provided the basis for later multichromophore arrays and also established a means of studying energy transfer to a reaction center. An antenna moiety consisting of four Zn(II)tetrarylporphyrins - a central Zn(II)porphyrin connected to the meso positions of three peripheral porphyrins - was attached to a free base porphyrin-fullerene reaction center ($(P_{ZP})_3$-P_{ZC}-P-C_{60}, **6**). This system established the feasibility of specifically exciting the antenna to induce charge separation in the attached reaction center (Fig. 4) [69]. Optimizing the design of the $(P_{ZP})_3$-P_{ZC}-P-C_{60} reaction center by replacing the diarylporphyrin of **6** with tetraarylporphyrin in **7**, and thereby increasing the potential of the electron donating porphyrin, provided more thermodynamic driving force for electron transfer from the antenna porphyrins to the radical cation of the freebase porphyrin and led to a hole delocalization in the antenna and longer lifetime of the final charge separated state [65]. The structural differences between **6** and **7** also led to different HOMO orbital types in the freebase porphyrin moieties: the β-alkyl substituents of the freebase porphyrin in **6** induce an a_{1u}-type HOMO with nodes at the meso positions, whereas the freebase porphyrin of **7** without β substituents and mesityl groups at the 10,20-meso positions exhibits an a_{2u}-type HOMO with lobes at the meso positions. These differences in the HOMO orbital structure combined with the steric influence of the β-alkyl groups of **6,** which results in an increased average dihedral angle and less π-π overlap between the meso aryl group and the porphyrin macrocycle, also create a substantial increase in the rate of singlet-singlet energy transfer rates, better antenna function, and increased quantum yield of final charge separation for **7** as compared to **6** [65].

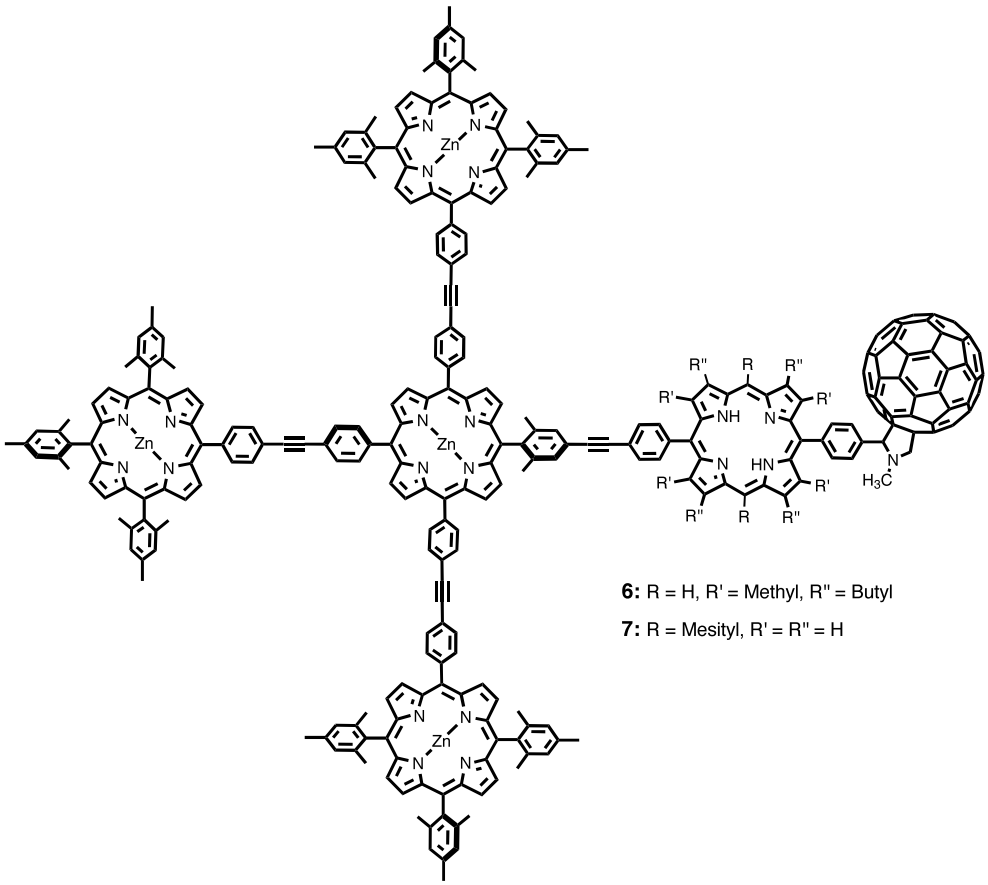

Figure 4: Chemical structures for antenna-reaction centers **6** and **7**.

Extending the concept of this design, an antenna-reaction center complex comprised of five bis(phenylethynyl)anthracene (BPEA) antenna molecules linked to a hexaphenylbenzene core and covalently linked to a porphyrin-fullerene complex **8** (Fig. 5), carried out efficient charge separation with better coverage of the spectrum from 430 to 480 nm [70].

Further elaboration of the antenna-reaction center came with the development of complex **9** (Fig. 6), consisting of several different chromophore moieties. Centered on a hexaphenylbenzene core, two bis(phenylethynyl)anthracene, two borondipyrromethene, and two Zn(II)tetraarylporphyrin dyes comprised an antenna complex with coverage across the visible spectrum [71]. Coordination of a dipyridyl functionalized fullerene to the two adjacent Zn(II)porphyrins of the antenna complex completed the formation of a multiantenna reaction center complex **9**. Excitation of any of the antenna pigments in the complex leads to rapid light induced electron transfer to the fullerene. Developing molecular design strategies for broad spectral coverage with funneling of excitation energy to charge transfer centers, such as those outlined above, plays a central role in the development of efficient solar to fuel systems.

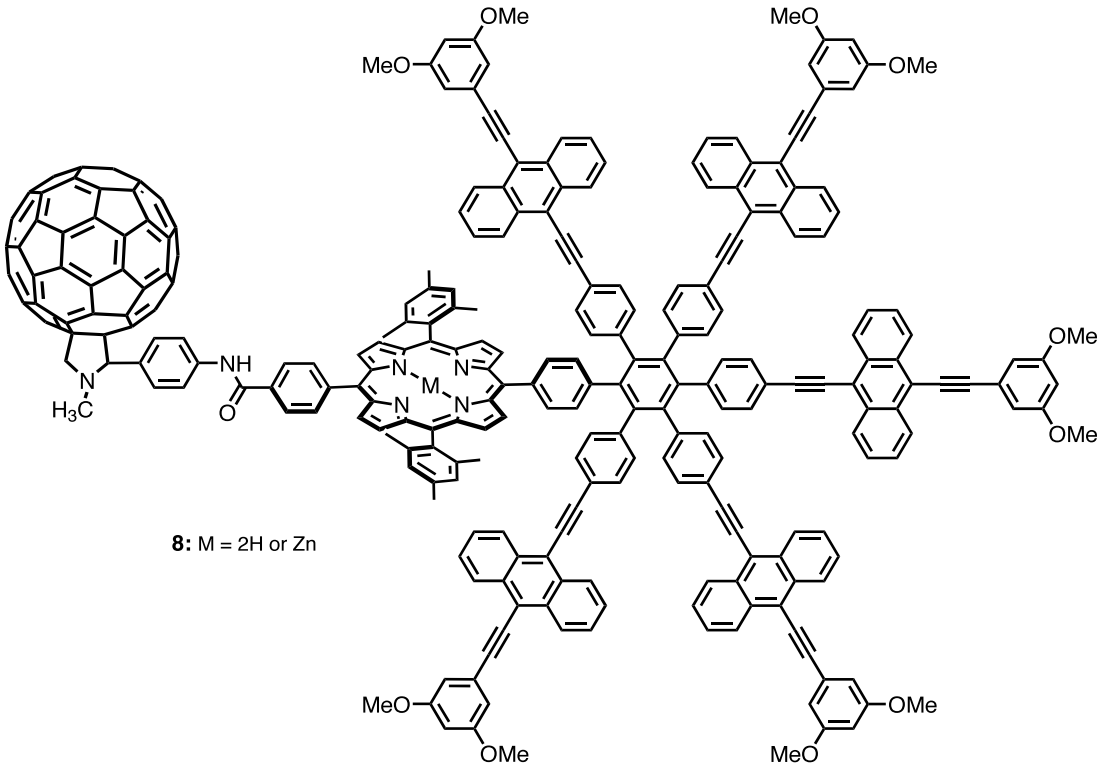

Figure 5:Antenna-reaction center complex **8**.

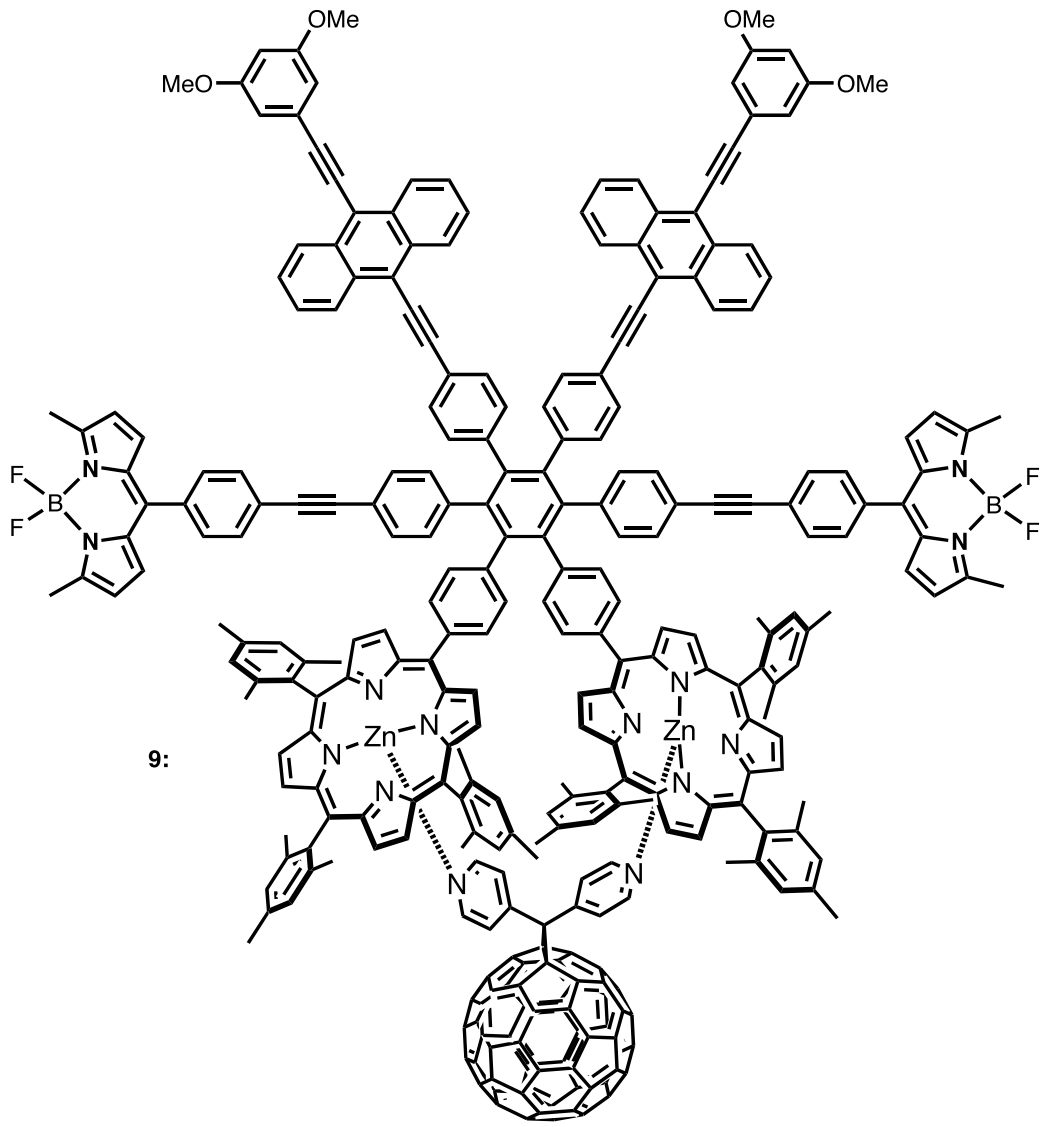

Figure 6: Antenna-reaction center complex **9**.

Photoregulation

During photosynthesis, the process of non-photochemical quenching (NPQ) enables the organism to avoid the buildup of energetic, and damaging, intermediates that would otherwise form under high light intensities [72,73]. Avoiding destructive intermediates formed under such conditions could likely increase the longevity of artificial systems in a similar manner. A pentad reaction center, consisting of a porphyrin primary donor, fullerene acceptor, two antenna pigments, and a dihydroindolizine (DHI) photochrome control moiety, demonstrated the ability of an artificial reaction center to reversibly change the quantum yield of charge separation based on the intensity of incident light [74]. Under low white light levels, in which the DHI exists primarily in the closed form, the reaction center carries out light induced charge separation with a quantum yield of 0.82. Under high white light intensities, the quantum yield of a solution of the pentad decreases to 0.27 as photoisomerization converts some of the photochrome to its open, betaine form (BT), a conformation competent for rapidly quenching the porphyrin excited singlet state by energy transfer. Upon forming BT at high white light intensities, the quenching of the porphyrin excited state prevents charge separation in the reaction centers of the isomerized molecules, markedly reducing the overall quantum yield for this process.

Charge separation across a membrane

Along with light capture and formation of a charge-separated state, an artificial solar-to-fuel system must convert incident light energy to some other useful form. In photosynthesis, photoinduced charge transfer across the thylakoid membrane is coupled to proton shuttling across the bilayer, thereby establishing a proton gradient. Dissipation

of the proton imbalance back across the membrane then drives the production of adenosine triphosphate (ATP) via a transmembrane ATP-synthase enzyme. Producing constructs capable of mimicking this process can offer insight into the design and development of artificial systems for solar energy conversion.

A study to this end demonstrated that illumination of a phospholipid bilayer impregnated with C-P-Q type reaction centers and separating a solution containing a sacrificial electron donor from that with an acceptor species results in the passage of photocurrent in a circuit bridging the bilayer membrane [75]. Building off this work, imbedding a similar C-P-Q type reaction center in the bilayer of a liposome set the basis of a system capable of pumping protons across the lipid layer [67]. The overall amphiphilic nature of the C-P-Q complex used directs the asymmetric insertion of the reaction center into the liposome with the carotenoid moiety toward the interior and the more polar quinone to the exterior. Excitation of the complex generates an oxidizing potential inside and a reducing potential around the periphery of the liposome. A freely diffusing quinone electron/proton carrier within the membrane of the liposome with a midpoint potential between that of the oxidized carotenoid and reduced quinone moieties of the reaction center shuttles protons across the membrane, resulting in the acidification of the interior of the liposome. This results in the creation of a light induced potential gradient across the bilayer.

In order to harness the proton motive force generated in this system, a CF_0F_1-ATP synthase was incorporated into the liposome along with the reaction center and redox mediator components [68]. With proton translocation driven by the photocycle described above, dissipation of the pH gradient coupled to the catalytic conversion of ADP and P_i

to ATP as carried out by the CF_0F_1-ATP synthase resulted in the net conversion of incident light energy into that of a high-energy chemical species. Quantitative analysis of the system reveals that in low light the absorption of 14 photons results in the production of 1 ATP molecule and, with illumination by 633 nm light, roughly 4% of the absorbed energy is conserved in the form of a chemical bond.

In a subsequent study, the same C-P-Q reaction center was used in conjunction with a quinone-like molecule whose ability to bind Ca^{2+} is modulated by the redox status [76]). This system was capable of pumping Ca^{2+} ions against a concentration gradient by the asymmetric arrangement of the C-P-Q reaction center in liposomes. Although the quantum yield was only 1%, a significant electrical potential was measured across the membrane extending Mitchell's mechanism of accumulating membrane potential using a redox loop to divalent cations in addition to protons.

Mimicking proton control during electron transfer

The $Tyrosine_Z$-Histidine190 (Tyr_Z-His190) pair of photosystem II (PSII) is thought to undergo proton coupled electron transfer (PCET) as it serves as an electron transfer mediator between P_{680} and the oxygen evolving complex (OEC) [9,77]. The interaction between Tyr_Z and His190 likely serves to tune the potential of the tyrosine residue so that it lies between that needed for the reduction of the photogenerated P_{680}^+ and the potential for oxidizing the OEC. Serving as an intermediary between P_{680} and the OEC, Tyr_Z-His190 prevents charge recombination that would otherwise compromise the catalytic activity of the Mn_4O_5Ca cluster of the OEC. This is especially important given that four oxidizing equivalents must accrue on the OEC to carry out the oxidation of one

molecule of water. To improve artificial systems, utilizing a similar design feature could also aid in preventing back electron transfer after photoinduced charge separation.

With the natural system as a template, we designed a porphyrin construct **10** (Fig. 7) bearing a benzimidazolphenol (BiP) moiety with the phenolic hydrogen capable of forming a hydrogen bond with the lone pair electrons of the imidazole nitrogen [78,79]. Chemically functionalizing the porphyrin to adsorb to the surface of a colloidal TiO_2 nanoparticle enables the assembly of **10** as shown in Fig. 7. This molecule-nanoparticle complex is reminiscent of the triad reaction centers discussed earlier, consisting of a porphyrin light absorber (PF_{10}), TiO_2 primary electron acceptor, and BiP electron donor [78]. Electron paramagnetic resonance studies of this complex reveal phenoxyl radical formation in the complex upon excitation of the porphyrin as a result of light induced charge separation. Given that the potential for the oxidation of the BiP moiety lies at 1.00 V vs. SCE, the photo-formed $BiP^{\bullet+}$-PF_{10}-$TiO_2^{\bullet-}$ state is thermodynamically competent for water oxidation.

A continuation of this study led to the development of **11** (Fig. 7), a fully organic triad complex with a tetracyanoporphyrin (TCNP) serving as the primary acceptor in place of a TiO_2 nanoparticle [80]. This complex bears considerable similarity to the Tyr_Z-His190-P_{680}-$Phoe_{D1}$ portion of the electron transport chain in PSII. Time resolved spectroscopic investigation of this reaction center in benzonitrile reveals that with excitation of TCNP the complex undergoes an initial electron transfer between the PF_{10} and TCNP resulting in Bi-PhOH-$PF_{10}^{\bullet+}$-$TCNP^{\bullet-}$. Competing with charge recombination, a second, rapid electron transfer then occurs between the benzimidazole-phenol and oxidized PF_{10}, presumably resulting in BiH^+-$PhO^{\bullet}$-PF_{10}-$TCNP^{\bullet-}$. This state forms with a

quantum yield of 0.52 and persists with a 4 μs lifetime, which is longer than those of many of the carotenoporphyrin-acceptor reaction centers of prior studies. Presumably, the final charge separated state reflects transfer of the phenolic proton to the nitrogen of the benzimidazole.

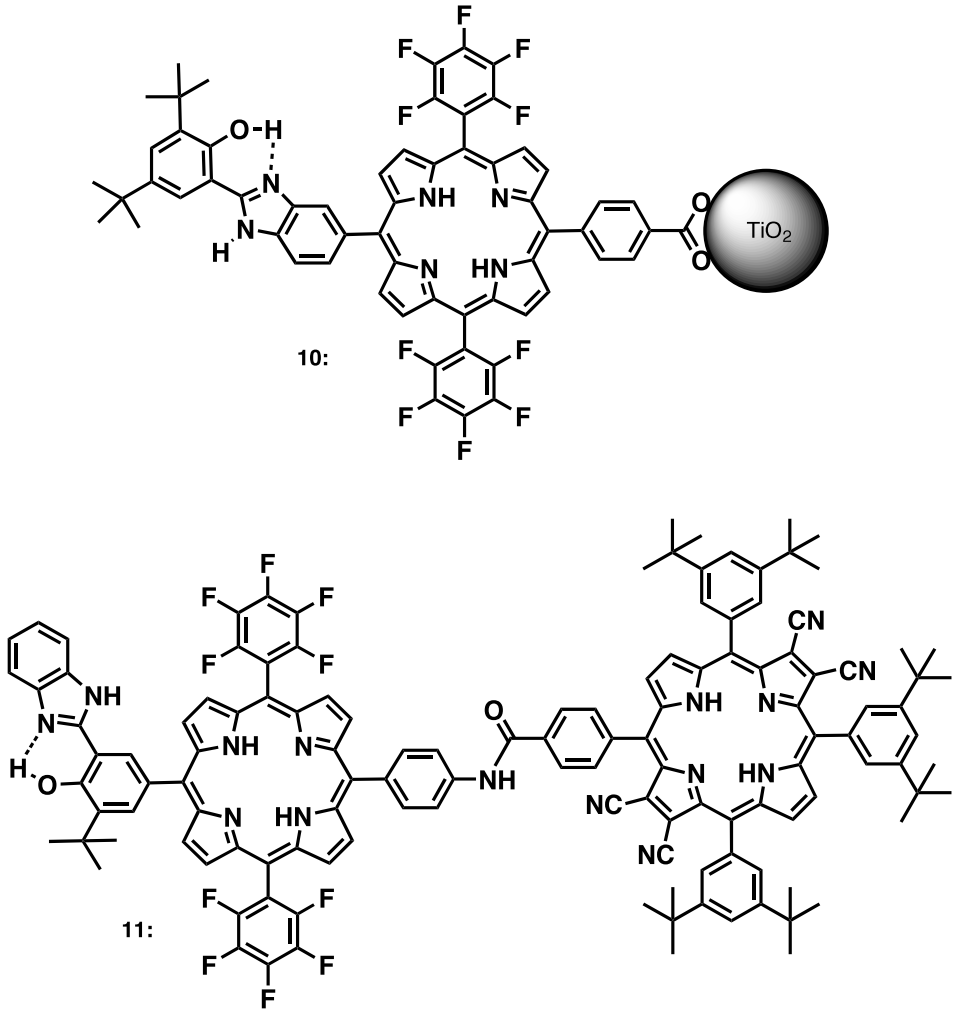

Figure 7: BiP containing triad reaction centers **10** and **11**.

Based on reduction potentials for model compounds [79], the $PF_{10}^{\bullet+}$ would not generate sufficient driving force for the formation of the Bi-$PhOH^{\bullet+}$-PF_{10}-$TCNP^{\bullet-}$, implying a PCET leading to the formation of the BiH^{+}-$PhO^{\bullet}$-PF_{10}-$TCNP^{\bullet-}$ state. The long-lived charge separated state and high potential of the oxidized BiH^{+}-$PhO^{\bullet}$ (1.04 V vs. SCE), make this reaction center type an ideal candidate for incorporation into the photoanode of a photoelectrochemical device for light driven water splitting.

Employing reaction centers for water splitting

Thus far, we have illustrated artificial photosynthetic systems for light absorption and charge separation via photoinduced electron transfer. Fuel production requires "wiring" such reaction centers to catalysts. One approach to doing so is to combine electrode architectures reminiscent of those used in dye sensitized solar cells with artificial reaction centers to produce photoelectrochemical water splitting cells.

In collaboration with the Mallouk lab, we developed a photoanode composed of a transparent fluorine doped tin oxide (FTO) conductive glass support bearing a nanoparticulate TiO_2 semiconducting layer to which is adsorbed a trisbipyridylruthenium(II) ($Ru(bpy)_3^{2+}$)-hydrated iridium oxide ($IrO_x \bullet nH_2O$) complex (Fig. 8) [33]. A photoelectrochemical cell (PEC) consisting of this electrode in combination with a platinum cathode in aqueous solution

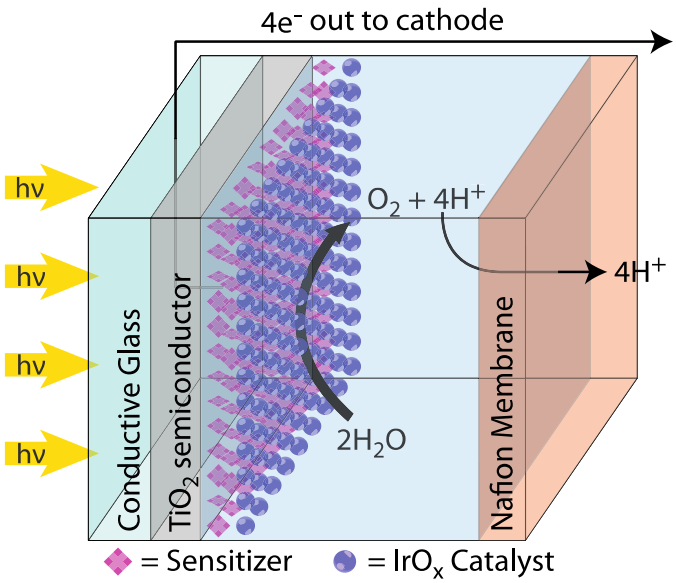

Figure 8: Schematic representation of the photoanode compartment of a PEC. Electrons and protons from water oxidation migrate to the cathode for fuel production.

demonstrated overall photolytic water splitting to oxygen and hydrogen, with the application of a small bias.

This system resembles a triad-type reaction center with a $Ru(bpy)_3^{2+}$ light absorber and primary electron donor, a TiO_2 primary acceptor, and an $IrO_x \bullet nH_2O$ secondary electron donor. Ideally, four sequential photocycle turnovers consisting of excitation of the $Ru(bpy)_3^{2+}$, electron transfer to the TiO_2 resulting in current flow to the platinum counter electrode, and hole transport to the $IrO_x \bullet nH_2O$, results in the conversion of water to oxygen at the $IrO_x \bullet nH_2O$ surface and production of hydrogen at the platinum cathode. While overall water splitting was observed, spectroscopic study of the system revealed that the charge recombination from the TiO_2 to the oxidized dye occurred nearly an order of magnitude faster than the forward electron transfer from the $IrO_x \bullet nH_2O$ to regenerate the ground state dye. This charge recombination imposes a major limitation on the performance of the system and represents a critical area for improvement.

In PSII, Tyr_Z serves the function of charge transfer mediator between P_{680} and the OEC and limits the occurrence of charge recombination. In order to address the analogous recombination in our system we turned to the use of the benzimidazolephenol of the BiP-P_{F10}-TiO_2 triad (Fig. 7) as a redox mediator in the photoelectrochemical system. Chemically modifying the BiP with a dicarboxylate functionality enabled the production of colloidal $IrO_x \bullet nH_2O$ particles decorated with both the BiP mediator and 2-dicarboxyethylphosphonic acid (CEPA) [81]. Study of a PEC similar to that of the earlier work but using an FTO-TiO_2 photoanode bearing co-immobilized $Ru(bpy)_3^{2+}$ dye and BiP/CEPA-$IrO_x \bullet nH_2O$ shows that the BiP mediator improves the performance of the system. As compared to a cell without the mediator (using only CEPA capped

IrO_x•*n*H_2O), higher photocurrents and greater overall efficiency (about a factor of three) are observed. Transient bleaching recovery traces showed that the improved performance results from faster regeneration of the ground state dye from the first oxidized state with the presence of BiP in the system [81]. Thus, BiP serves a similar role to that of Tyr_Z in PSII by preventing recombination losses after light induced charge separation.

Conclusion

This account shows our research group's trajectory from building simple molecular reaction center constructs to developing complete systems for the conversion of solar energy to a fuel. Efficient and economical systems which can generate a sustainable fuel from sunlight and a widely available precursor such as water are requisite to meeting future human energy demand in a way that does not endanger the diversity of life on the planet or the health and wellbeing of its inhabitants. Developing and improving the technologies for such systems represents a principal challenge of the modern world. The complications of fulfilling energy demand requires a host of sustainable technologies for varying locales. Certainly, solar energy will play a substantial role, and chemical fuels provide the greatest possible flexibility of usage.

We have pursued this challenge through the study of artificial reaction centers designed to mimic aspects of photosynthesis. As the only process capable of converting solar energy to a chemical fuel on a planet wide scale, photosynthesis provides a model for doing so by artificial means. The development and study of molecular reaction centers has culminated in the development of a first generation of dye sensitized photoelectrochemical cells for solar-to-fuel conversion. Substantial work remains in advancing the viability of this system. For instance, we are exploring the synthesis and

use of new dye-catalyst constructs [34] and catalytic materials based on more abundant elements [82]. Ultimately the grand challenge of supplying sustainable energy requires contributions from many researchers and all fields of science; our best hope lies in developing a range of renewable energy technologies and contributing to a well informed and well equipped global society.

Acknowledgments

This work was supported by the Center for Bio-Inspired Solar Fuel Production, an Energy Frontier Research Center funded by the U.S. Department of Energy, Office of Science, Office of Basic Energy Sciences under award Number DE-SC0001016. Some of the research described in this review was supported by the National Science Foundation (CHE-0352599) and U.S. Department of Energy (DE-FG02-03ER15393). M.D.V. thanks the National Science Foundation for support from the Graduate Research Fellowship Program (GRFP).

CHAPTER 2

PORPHYRINS FOR WATER OXIDATION

A Porphyrin-Stabilized Iridium Oxide Water Oxidation Catalyst

Benjamin D. Sherman,[a] Smitha Pillai,[a] Gerdenis Kodis,[a] Jesse J. Bergkamp,[a] Thomas E. Mallouk,[b] Devens Gust,[a]* Thomas A. Moore,[a]* and Ana L. Moore[a]*

[a] Center for Bioenergy and Photosynthesis and Department of Chemistry and Biochemistry, Arizona State University, Tempe, AZ 85287-1604, USA

[b] Department of Chemistry, The Pennsylvania State University, University Park, Pennsylvania 16802,USA

Citation:

Sherman, B. D.; Pillai, S.; Kodis, G.; Bergkamp, J.; Mallouk, T. E.; Gust, D.; Moore, T. A.; Moore, A. L. A porphyrin-stabilized iridium oxide water oxidation catalyst. *Can. J. Chem.* **2011**, *89*, 152–157.

My contribution to this work was helping with the preparation of the porphyrin dyes and aiding in the editing process.

Abstract:

Colloidal solutions of iridium oxide hydrate ($IrO_2 \cdot nH_2O$) were formed using porphyrin stabilizers bearing malonate-like functional groups at each of the four meso positions of the porphyrin ring. Cyclic voltammetry and monitoring of solution oxygen concentrations under constant applied potential demonstrate the electrochemical catalytic activity of the porphyrin–$IrO_2 \cdot nH_2O$ complexes for the oxidation of water to oxygen.

Quenching of the porphyrin fluorescence in the complex implies strong interaction between the porphyrin and the $IrO_2 \cdot nH_2O$. These results mark a step toward developing a porphyrin-based photoanode for use in a photoelectrochemical water splitting cell.

Keywords: water oxidation, electrochemical catalysis, iridium oxide, porphyrin.

Introduction:

Work carried out by Harriman et al. over twenty years ago demonstrated that hydrated iridium oxide ($IrO_2 \cdot nH_2O$) is an active, stable, and efficient catalyst for water oxidation [83-85]. Colloidal $IrO_2 \cdot nH_2O$ in solution with either $Ru(II)(bpy)_3$ or porphyrin dye could carry out the photochemical generation of O_2 from water [84,85]. These studies, however, required the presence of a strong oxidant ($S_2O_8^{2-}$) to generate the photo-oxidized dye that then would oxidize the catalyst. Subsequent electrochemical studies by other groups investigated techniques for immobilizing $IrO_2 \cdot nH_2O$ on the surface of transparent glass electrodes [86-88]. Yagi et al. showed that adsorbed layers formed on the surface of indium doped tin oxide (ITO) and fluorine doped tin oxide (FTO) electrodes when the electrodes were allowed to soak in a solution containing citrate-stabilized colloidal $IrO_2 \cdot nH_2O$ [87,88]. Electrochemical studies on prepared electrodes showed the onset of catalytic current near 1.0 V vs. SCE at pH 5.3 (no $IrO_2 \cdot nH_2O$ in solution). Murray et al. have studied $IrO_2 \cdot nH_2O$ particles formed at high pH, without the use of stabilizing groups, both on a surface and in solution [89,90]. Their work has shown the need for only 0.15 V of overpotential for the onset of water oxidation and 100% current efficiency for the generation of O_2 from water at an overpotential of 0.29 V. While the

catalytic activity of $IrO_2 \cdot nH_2O$ has been well established, only recently has a system capable of driving the catalyst photoelectrochemically been demonstrated [33].

We have reported the development of a water splitting photoelectrochemical cell employing a $Ru(II)(bpy)_3$–$IrO_2 \cdot nH_2O$ based photoanode [33]. In that work, the dye–$IrO_2 \cdot nH_2O$ complex was formed using a heteroleptic $Ru(II)(bpy)_3$ complex containing phosphonate groups on one of the bipyridyl ligands and a malonate group on another. Previous work had demonstrated the preference of carboxylate groups over phosphonate groups for binding to the surface of $IrO_2 \cdot nH_2O$ [38]. This chemistry allowed for the formation of small $IrO_2 \cdot nH_2O$ particles (1–5 nm), capped with $Ru(II)(bpy)_3$ dye molecules containing exposed phosphonate groups [33,38]. The dye–$IrO_2 \cdot nH_2O$ constructs could then be attached to metal oxide semiconductors, such as titanium dioxide (TiO_2), via the phosphonate group.

In this system, the photoanode consisted of the dye–$IrO_2 \cdot nH_2O$ complex adsorbed to a TiO_2 layer on top of an FTO electrode. When this photoanode was combined with a platinum cathode in a photoelectrochemical cell, the cell produced a photocurrent of 12.7 $\mu A\ cm^{-2}$ upon illumination with 450 nm light at an intensity of 7.8 $mW\ cm^{-2}$, giving an internal quantum yield of 0.9% [33]. Three principal factors limited the performance of this system: slow electron transfer from the $IrO_2 \cdot nH_2O$ catalyst to the oxidized dye, bleaching of the dye likely due to nucleophilic attack on the oxidized dye, and the need for applied bias to achieve overall water splitting. Transient spectroscopic studies showed electron transfer from the $IrO_2 \cdot nH_2O$ to the photo-oxidized dye (2.8 ms) to be an order of magnitude slower than the back electron transfer from TiO_2 to the oxidized dye (0.37 ms) [33]. An additional issue with $Ru(II)(bpy)_3$ complexes as photosensitizers is that they

absorb strongly in the blue but cannot efficiently utilize light in the red region of the spectrum.

The work outlined herein seeks to improve the stability, electron transfer rate, and spectral properties of the dye–$IrO_2 \cdot nH_2O$ complex by incorporating a porphyrin rather than the $Ru(II)(bpy)_3$ dye. We report the synthesis of a porphyrin–$IrO_2 \cdot nH_2O$ complex which shows electrochemical catalytic response similar to other $IrO_2 \cdot nH_2O$ complexes [87]. Finally, fluorescence lifetime measurements indicate quenching of the porphyrin fluorescence in the porphyrin–$IrO_2 \cdot nH_2O$ complex.

Experimental

Materials

Sephadex with a 5,000 molecular weight cutoff, Na_2HPO_4, NaH_2PO_4, tetrabutylammonium hexafluorophosphate and benzonitrile were obtained from Sigma Aldrich. Benzonitrile was distilled prior to use. K_2IrCl_6 was used as received from Alfa Aesar. KNO_3 was obtained from Fluka. Tetrahydrofuran for synthesis was distilled from sodium/benzophenone. Dimethylformamide was dried over activated 4 Å molecular sieves. Dichloromethane used for chromatography was distilled from calcium hydride.

Porphyrin Synthesis

General Methods: 5,10,15,20-Tetrakis(4-bromomethylphenyl)porphyrin was synthesized by a published method [91]. The malonate substitution and cleavage of the esters were performed by literature procedures used for related compounds [92-94]. Palladium insertion was achieved by adapting Durantini's procedure [93].

Porphyrin 1

Sodium hydride (387 mg, 16 mmol) was suspended in 10 mL of dry THF under nitrogen atmosphere. Diethyl malonate (0.61 ml, 4 mmol) in 20 mL THF was added dropwise under ice cooling. After being stirred for 1 h at room temperature, a solution of 5,10,15,20-tetrakis(4-bromomethylphenyl)porphyrin (200 mg, 0.20 mmol) in 20 mL of dry THF was added dropwise to the mixture and stirred for 1 h. The reaction mixture was then poured into an ice-cold saturated NH_4Cl solution. The aqueous layer was extracted with CH_2Cl_2. The organic solution was washed thoroughly with water and dried over Na_2SO_4. The crude material was purified by column chromatography on silica gel (solvent CH_2Cl_2/EtOAc 20/1). Yield: 120 mg (45%). ^{1}H NMR: (400 MHz, $CDCl_3$, RT): δ -2.82 (s, 2H, NH), 1.34 (t, 24H, J = 7.2 Hz, ethyl CH_3), 3.56 (d, 8H, J = 7.7 Hz, CH_2), 3.96 (t, 4H, J = 7.7 Hz, CH), 4.3(m, 16H, J = 7.2 Hz, ethyl CH_2), 7.58 (d, 8H, J = 8.0 Hz, phenyl–CH_2), 8.10 (d, 8H, J = 8.0 Hz, phenyl–CH_2), 8.77 (s, 8H pyrrolic H). MALDI-TOF-MS m/z: calcd. for $C_{76}H_{78}N_4O_{16}$ 1302.54, obsd. 1302.67. UV-vis (CH_2Cl_2): λ_{max} 419, 516, 551, 591, 647 nm.

Porphyrin 1a

A 50 mg (0.038 mmol) portion of 1 and finely ground sodium hydroxide (292 mg, 7.5 mmol) were suspended in 40 mL of ethanol. The mixture was refluxed for 15 h and a precipitate was formed. The mixture was cooled to room temperature and filtered. The residue was washed with a little ice-cold ethanol and dried in high vacuum. Yield: 43 mg (89.5%). ^{1}H NMR: (400 MHz, D_2O, RT): δ 3.3 (d, 8H, J = 7.9 Hz, CH_2), 3.59 (t, 4H, J = 7.9 Hz, CH), 7.58 (d, 8H, J = 7.8 Hz, phenyl–CH_2), 7.9 (d, 8H, J = 7.8 Hz, phenyl–CH_2), 8.47 (s, 4H, pyrrolic H), 8.98 (s, 4H, pyrrolic H). MALDI-TOF-MS m/z: calcd. for $C_{76}H_{78}N_4O_{16}$ 1079.02, obsd. 1079.41. UV-vis (H_2O): λ_{max} 415, 519, 557, 582, 635 nm.

Porphyrin 2

To a solution of 1 (24 mg, 0.018 mmol) in 10 mL DMF was added palladium(II) chloride (32.6 mg 0.18 mmol). The mixture was stirred for 1 h at 55 ^{0}C under nitrogen. The solvent was removed under reduced pressure and the compound was purified by column chromatography on silica gel (solvent CH_2Cl_2/EtOAc 20/1). Yield: 21 mg (81%). ^{1}H NMR: (400 MHz, $CDCl_3$, RT): δ 1.35 (t, 24H, J = 7.2 Hz, ethyl CH_3), 3.56 (d, 8H, J = 7.7 Hz, CH_2), 3.96 (t, 4H, J = 7.7 Hz, CH), 4.3(m, 16H, J = 7.2 Hz, ethyl CH_2), 7.58 (d, 8H, J = 8.0 Hz, phenyl CH_2), 8.06 (d, 8H, J = 8.0 Hz, phenyl CH_2), 8.75 (s, 8H pyrrolic H). MALDI-TOF-MS m/z: calcd. for $C_{76}H_{78}N_4O_{16}$ 1302.54, obsd. 1302.67. UV-vis (CH_2Cl_2): λ_{max} 416, 523 nm.

Porphyrin 2a

Porphyrin 2 (20 mg, 0.014 mmol) and finely ground sodium hydroxide (107 mg, 2.7 mmol) were suspended in 20 mL of ethanol. The mixture was refluxed for 15 h and a precipitate was formed. The mixture was cooled to room temperature and filtered. The residue was washed with a little ice-cold ethanol and dried in high vacuum. Yield: 17 mg (88%). ^{1}H NMR: (400 MHz, D_2O, RT): δ 3.28 (d, 8H, J = 7.9 Hz, CH_2), 3.59 (t, 4H, J = 7.9 Hz, CH), 7.58 (d, 8H, J = 7.8 Hz, phenyl CH_2), 7.96 (s, 8H phenyl CH_2), 8.47 (s, 8H, pyrrolic H). UV-vis (H_2O): λ_{max} 413, 522 nm.

Preparation of the porphyrin–$IrO_2 \cdot nH_2O$ complex

The complex was formed in a solution containing 50 μM of the porphyrin sodium salt, either 1a or 2a, and 1 mM of K_2IrCl_6. The solution was adjusted to pH 8 with 0.25 M NaOH and heated to 35° C, and the reaction was allowed to proceed (~2–3 days) until the starting red-brown solution became pale yellow. The pH of the solution was monitored

throughout the reaction period and NaOH was added as necessary to maintain mildly basic pH. The resulting colloids were either used as such or purified by size exclusion chromatography using a Sephadex gel filtration medium. The malonate–$IrO_2 \cdot nH_2O$ was prepared as previously described [38].

Electrochemical Measurements

All electrochemical measurements were done using a CH Instruments 760D potentiostat along with software provided by the manufacturer. A glassy carbon or platinum working electrode was used as indicated along with a Ag/Ag^+ quasi reference or Ag/AgCl (in saturated KCl) reference and a Pt wire mesh counter electrode. Ferrocene was used to calibrate the potential of the Ag/Ag^+ quasi reference with Cp_2Fe^+/Cp_2Fc taken as 0.45 V vs. SCE. Cyclic voltammetric (CV) measurements of 1 and 2 were done in benzonitrile with 0.1 M tetrabutylammonium hexafluorophosphate. Porphyrin–$IrO_2 \cdot nH_2O$ measurements were done in 0.1 M KNO_3 aqueous solution at the scan rates and potentials indicated. Some measurements were taken in 0.1 M phosphate buffer with pH near 7 as indicated.

Clark Electrode Measurements

A Yellow Springs Instrument Co. 5300 Biological Oxygen Monitor was used to measure the $\%O_2$ in solution with air saturated solution set as 100% O_2. Solutions were purged of O_2 by bubbling Ar until reaching a level of 30-50% O_2. Argon was then flowed over the headspace of the cell to keep atmospheric O_2 from entering. After reading a stable $\%O_2$ level for 2-5 min, the amperometry experiment was initiated. A line was fitted to the stable $\%O_2$ reading for the 60 s before applying potential in the experiment and a

fitted line was subtracted from the trace to give $\Delta\%O_2$ (change in $\%O_2$ during the experiment) as show in Figure 3.

Time-resolved Fluorescence Measurements

Fluorescence decay measurements were performed by the time-correlated single-photon-counting method. The excitation source for the system was a mode-locked Ti:Sapphire laser (Spectra Physics, Millennia-pumped Tsunami) with a 130 fs pulse duration operating at 80 MHz. The laser output was sent through a frequency doubler and pulse selector (Spectra Physics Model 3980) to obtain 370-450 nm pulses at 4 MHz. Fluorescence emission was detected at the magic angle using a double grating monochromator (Jobin Yvon Gemini-180) and a microchannel plate photomultiplier tube (Hamamatsu R3809U-50). The instrument response function was 35–55 ps. The spectrometer was controlled by software based on the LabView programming language and data acquisition was done using a single photon counting card (Becker-Hickl, SPC-830).

Data analysis was carried out using locally written software (ASUFIT) developed in a MATLAB environment (Mathworks Inc.). Random errors associated with the reported lifetimes obtained from fluorescence were typically ≤ 5%.

Results and Discussion

This work centers on the use of tetrakis(methylphenylmalonate)porphyrins as stabilizers for the formation of $IrO_2 \cdot nH_2O$ colloidal solutions. It builds on the previous finding that bidentate carboxylic acid groups act as effective stabilizers for the formation of small $IrO_2 \cdot nH_2O$ colloidal particles [38]). The porphyrins used in this study contain methylphenylmalonate groups at each of the para positions of the four meso phenyl

groups; it is expected that the colloidal particles formed with these stabilizers will be similar in structure to those reported by Hoertz et al [38].

Colloidal $IrO_2 \cdot nH_2O$ particles were successfully formed using porphyrin 1a and its Pd analogue, 2a, shown in Figure 1 along with their protected ester forms (1 and 2). Synthesis of the $IrO_2 \cdot nH_2O$ colloids entailed heating a solution containing K_2IrCl_6 and the porphyrin at 35°C for ~2–3 days. The initial pH of the solution was adjusted to near pH 8 with NaOH and monitored and adjusted throughout the synthesis to maintain moderately basic conditions. The resulting colloidal solution was a pale yellow color. In some cases the resulting preparation was purified over a size exclusion column to remove salts and unused starting material. Solutions prepared in this way were stored under mildly basic conditions and remained stable on the bench top for several months.

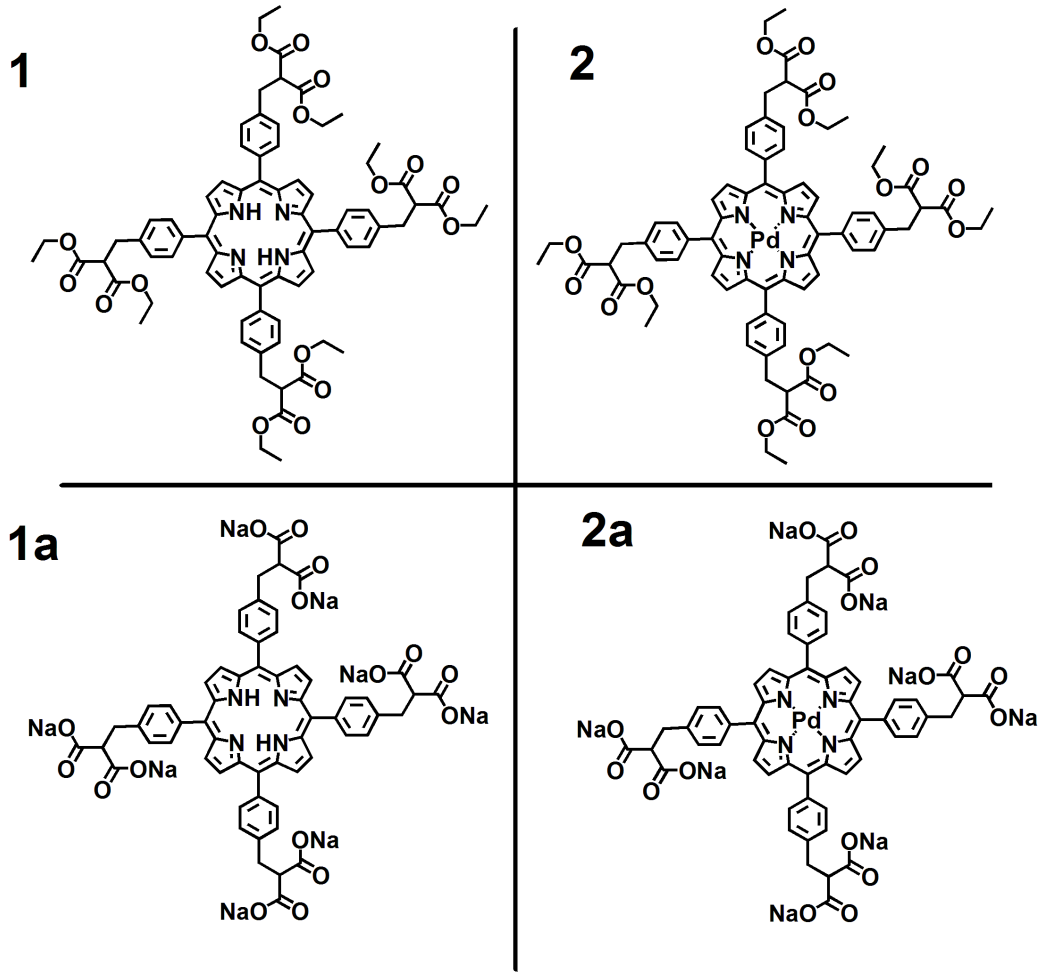

Figure 1: Structures of porphyrin 1, the octasodium salt of 1 (1a), porphyrin 2, and the octasodium salt of 2 (2a).

Cyclic voltammetry (CV) experiments were carried out to elucidate the electrochemical characteristics of the colloids. A typical voltammogram reveals the onset of strong anodic current near 1.1 V vs. Ag/AgCl, indicative of water oxidation. Poising of the working electrode at sufficiently positive potentials causes the generation of bubbles at the electrode surface in solutions containing the porphyrin–$IrO_2 \cdot nH_2O$. Figure 2 shows an overlay of several voltammograms performed in the presence of $IrO_2 \cdot nH_2O$ catalysts. The various $IrO_2 \cdot nH_2O$ complexes give comparable voltammograms, with strong anodic signals indicative of water oxidation. Comparison with the scan in the absence of any $IrO_2 \cdot nH_2O$ clearly shows the signal originates from the presence of the catalyst. It should be emphasized that Figure 2 is not intended as a quantitative comparison between the various $IrO_2 \cdot nH_2O$ complexes as the concentration and likely the size of the colloid was different in each case, but rather as a means of demonstrating that the behavior of the porphyrin–$IrO_2 \cdot nH_2O$ complexes is similar to that of the carboxylic acid (malonate or citrate) stabilized $IrO_2 \cdot nH_2O$ complexes described in the literature [87,88].

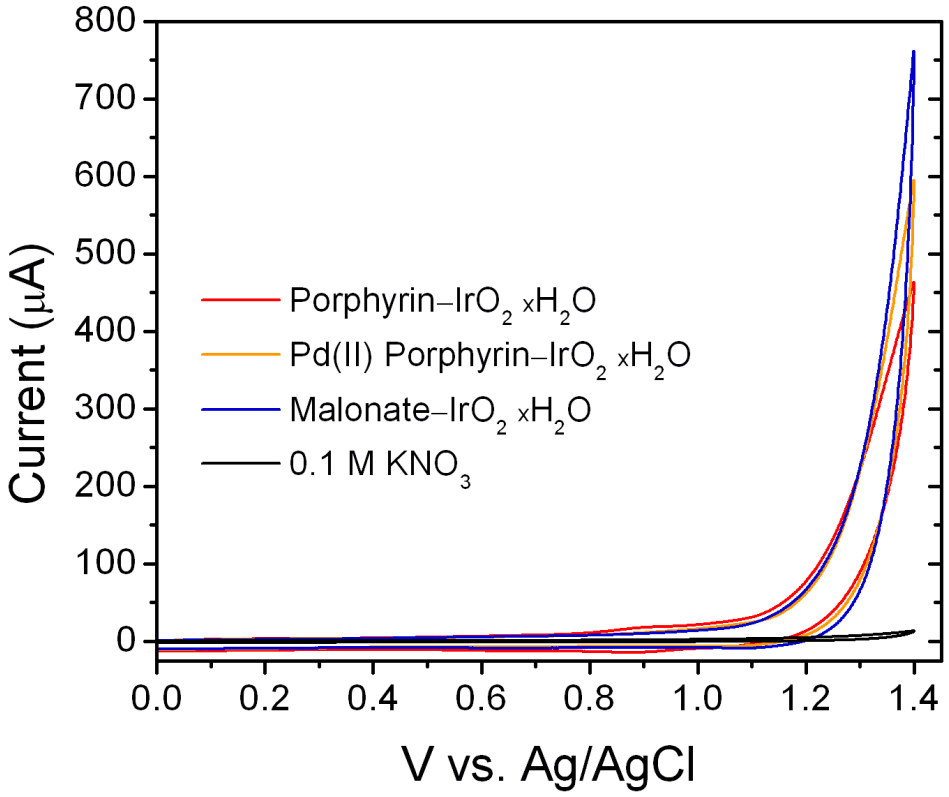

Figure 2: Comparison of cyclic voltammograms taken in solutions containing (red) porphyrin 1a–$IrO_2 \cdot nH_2O$, (orange) porphyrin 2a–$IrO_2 \cdot nH_2O$, (blue) malonate–$IrO_2 \cdot nH_2O$ or (black) only supporting electrolyte. All scans taken with a glassy carbon working electrode, at a scan rate of 100 mV/s, with voltages referenced to a Ag/AgCl electrode. The solutions contained $IrO_2 \cdot nH_2O$ colloidal catalyst at different concentrations and the currents observed should not be taken as a quantitative comparison of catalytic activity.

In order to demonstrate that the observed catalytic signal corresponds to the oxidation of water to O_2, a Clark electrode was employed to monitor the O_2 concentration in the solution during electrochemical measurements. After purging the cell of O_2 by bubbling with argon, the cell was sealed and the O_2 concentration was monitored while poising the glassy carbon working electrode at various potentials vs. Ag/AgCl (Figure 3). With porphyrin 2a–$IrO_2 \cdot nH_2O$ in solution, the O_2 concentration does not increase with time at 0.6 V vs. Ag/AgCl, but does increase at 1.4 V. When the same working electrode is used in a solution containing only supporting electrolyte and no catalyst, no increase in O_2 occurs at either 0.6 or 1.4 V vs. Ag/AgCl. Thus, oxygen is produced only in the presence of the catalyst at a suitable potential.

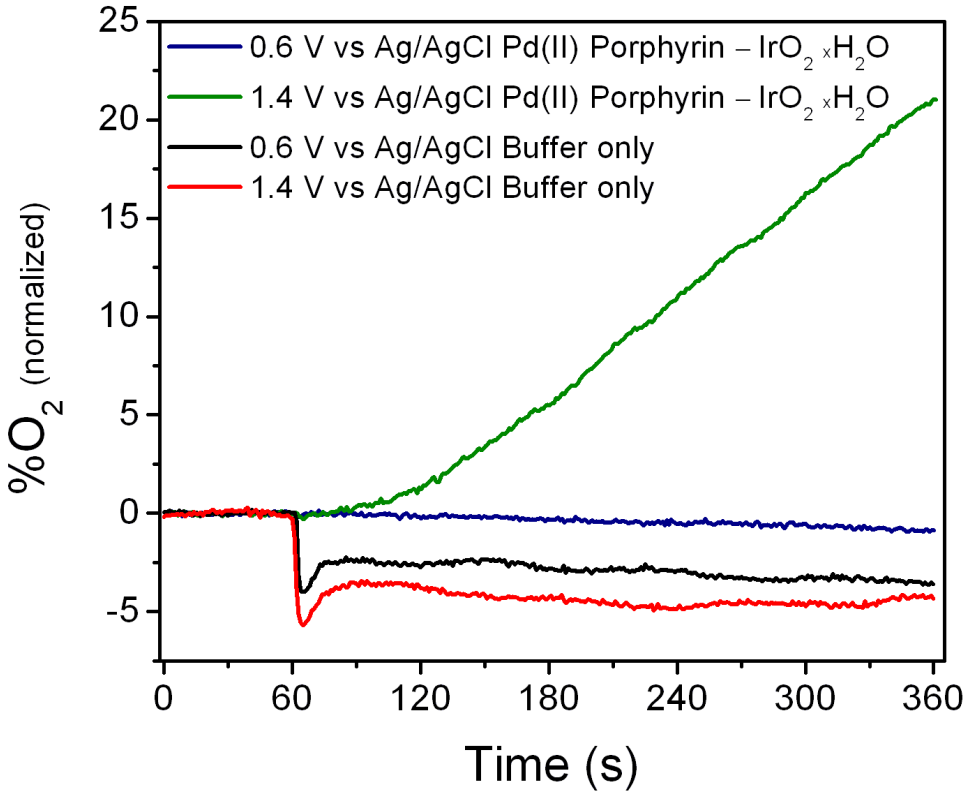

Figure 3: Oxygen concentration relative to air-saturated water measured with a Clark electrode. Green line: porphyrin 2a–$IrO_2 \cdot nH_2O$, glassy carbon working electrode poised at 1.4 V vs. Ag/AgCl. Blue line: porphyrin 2a–$IrO_2 \cdot nH_2O$, glassy carbon working electrode poised at 0.6 V vs. Ag/AgCl. Black line: buffer only, glassy carbon working electrode poised at 0.6 V vs. Ag/AgCl. Red line: buffer only, glassy carbon working electrode poised at 1.4 V vs. Ag/AgCl. All measurements taken in H_2O at pH 6.95 with 0.1 M KNO_3 and 0.1 M phosphate buffer. Potential applied starting at t = 60 sec.

As one means of assessing the interaction of the porphyrin dye with the $IrO_2 \cdot nH_2O$, the porphyrin fluorescence lifetimes in the porphyrin–$IrO_2 \cdot nH_2O$ complex and with the porphyrin dissolved in a solution containing malonate–$IrO_2 \cdot nH_2O$ were determined. As shown in Figure 4, the fluorescence lifetime of the free porphyrin 1a in the presence of malonate–$IrO_2 \cdot nH_2O$ was 8.79 ns. This lifetime is typical for a free base porphyrin of this general type. The fluorescence lifetime of the same porphyrin complexed with $IrO_2 \cdot nH_2O$ was quenched, with the major lifetime component of 46.7 ps (70.4%), and minor components with lifetimes of 316.9 ps (18.6 %), 1.81 ns (9.1%), and 7.09 ns (1.9 %). These results suggest that different populations of porphyrin molecules in the material experience different interactions with the $IrO_2 \cdot nH_2O$. The dominant short fluorescence lifetime component implies a significant interaction between the porphyrin and the $IrO_2 \cdot nH_2O$ particle. Quenching by energy transfer, electron transfer, enhanced intersystem crossing or some combination of these is possible; the exact mechanism has not been assigned. Fortunately, the porphyrin excited state is not quenched to the point that the quantum yield of electron injection into a nanostructured Ti- or Sn- oxide would be expected to be limited.

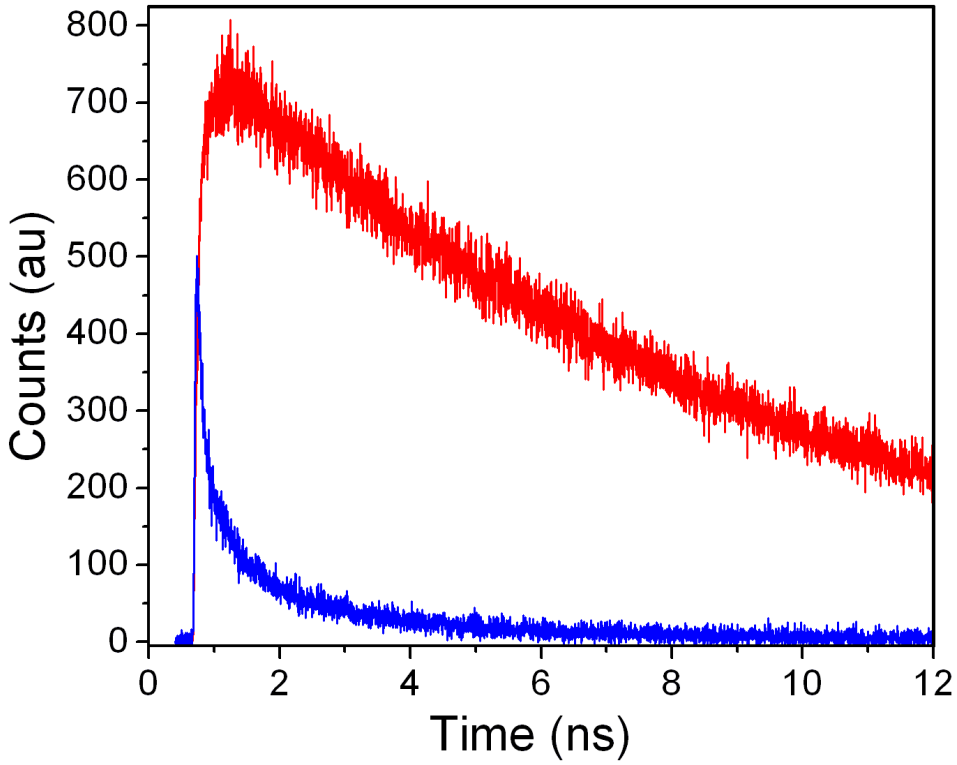

Figure 4: Porphyrin fluorescence lifetime measurements. (Red) porphyrin 1a in solution with malonate-stabilized $IrO_2 \cdot nH_2O$, lifetime 8.79 ns. (Blue) porphyrin 1a–$IrO_2 \cdot nH_2O$ colloidal particles, major component lifetime 46.7 ps (see text).

In these photoanodes, the driving force for electron transfer from the $IrO_2 \cdot nH_2O$ catalyst to the sensitizer is provided by the electrochemical potential for the reduction of the porphyrin radical cation. Figure 5 shows cyclic voltammograms of free base porphyrin 1 and its Pd analog 2. As seen in Table 1, the addition of Pd increases the potential by ~160 mV. Having these two sensitizers available will facilitate mechanistic studies designed to determine the yield-limiting steps in the photooxidation of water.

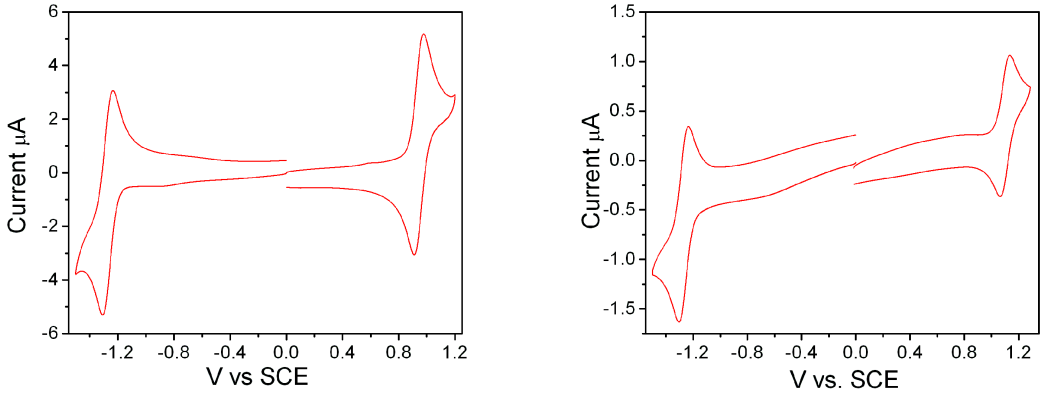

Figure 5: Cyclic Voltammograms of (a) porphyrin 1 and (b) porphyrin 2.

Voltammograms were taken with a platinum working electrode in benzonitrile with 0.1 M tetrabutylammonium hexafluorophosphate, at a scan rate of 100 mV/s.

Table 1: Electrochemical potentials for 1 and 2.

Porphyrin	1^{st} ox V vs. SCE	ΔE_p 1^{st} ox mV	1^{st} red V vs. SCE	ΔE_p 1^{st} red mV
(1)	0.94	67	-1.28	75
(2)	1.10	72	-1.28	71

ΔE_p: difference between anodic and cathodic peak potentials of the CV. Scan rate: 100 mV/s.

Conclusion:

We report the use of a high potential, porphyrin-based stabilizer in the formation of $IrO_2 \cdot nH_2O$ colloidal particles and have demonstrated catalytic electrochemical water oxidation by this complex. The porphyrin was designed to incorporate dicarboxylic acid groups at each of the four meso positions as such groups are known to interact favorably with the $IrO_2 \cdot nH_2O$ surface [38]. This work is a step towards the synthesis of a high potential porphyrin carrying the proper moieties, namely para-malonate and phosphonate groups on the porphyrin ring, to allow formation of the catalytic complex and then its subsequent adsorption to a transparent conductive electrode. This construct will be the photoanode of a porphyrin-based analogue of the $Ru(II)(bpy)_3$-based water splitting photoelectrochemical (PEC) cells that have previously been reported by us [33] as well as by other groups [95].

Acknowledgments

This work is supported as part of the Center for Bio-Inspired Solar Fuel Production, an Energy Frontier Research Center funded by the U.S. Department of Energy, Office of Science, Office of Basic Energy Sciences under Award Number DE-SC0001016, and by the Office of Basic Energy Sciences, Division of Chemical Sciences, Geosciences, and Energy Biosciences, Department of Energy under contract DE-FG02-07ER15911. B.D.S. thanks Science Foundation Arizona for their support in this work through a graduate research fellowship.

CHAPTER 3

PHTHALOCYANINES FOR PROTON REDUCTION

Synthesis and characterization of silicon phthalocyanines bearing axial phenoxyl groups for attachment to semiconducting metal oxides

Jesse J. Bergkamp,[a] Benjamin D. Sherman,[a] Ernesto Mariño-Ochoa,[b] Rodrigo E. Palacios,[c] Gonzalo Cosa,[d] Thomas A. Moore*,[a] Devens Gust◊*,[a] and Ana L. Moore*[a]

[a] Department of Chemistry and Biochemistry, Center for Bio-Inspired Solar Fuel Production, Arizona State University, Tempe, Arizona 85287-1604, USA

[b] Department of Chemistry, Tecnológico de Monterrey, Campus Monterrey, Monterrey, NL, 64849, México

[c] Departamento de Química, Facultad de Ciencias Exactas Físico-Químicas y Naturales, Universidad Nacional de Río Cuarto, Río Cuarto, Córdoba 5800, Argentina

[d] Department of Chemistry, McGill University, Otto Maass Chemistry Building # 314, 801 Sherbrooke Street West, Montreal, QC, H3A 2K6, Canada

Citation:

Bergkamp, J. J.; Sherman, B. D.; Mariño-Ochoa, E.; Palacios, R. E.; Cosa, G.; Moore, T. A.; Gust, D.; Moore, A. L. Synthesis and characterization of silicon phthalocyanines bearing axial phenoxyl groups for attachment to semiconducting metal oxides. *J. Porphyrins Phthalocyanines* **2011**, *15*, 943–950.

Abstract:

A series of axial phenoxy substituted octabutoxy silicon phthalocyanines bearing ethyl carboxylic ester and diethyl phosphonate groups have been prepared from the corresponding phenols in pyridine. Axial bis-hydroxy silicon phthalocyanine was prepared using an adaptation of a reported protocol [96,97] from the octabutoxy free-base phthalocyanine. The phenols bear either carboxylic ester or phosphonate groups, which upon deprotection can serve as anchoring groups for attaching the phthalocyanines to semiconducting metal oxides used in dye sensitized solar cells (DSSCs). All the phthalocyanines of the series absorb in the near infra-red region: 758–776 nm. The first oxidation potential for each phenoxy derivative occurs near 0.55 V vs. SCE as measured by cyclic voltammetry, with all falling within a 10 mV range. This indicates that these dyes will have sufficient energy in the photo-excited state to drive the reduction of protons to hydrogen. Taking into account the absorption and electrochemical potentials, these dyes are promising candidates for use in dual-threshold photoelectrochemical cells.

Keywords: silicon phthalocyanines, synthesis, electrochemistry, axial phenoxy linkage

*Correspondence to: Ana L. Moore, email: amoore@asu.edu, phone: 480-965-2953, fax: 480-965-2747, Devens Gust, email: gust@asu.edu, Thomas A. Moore, email: tom.moore@asu.edu.

[◊]Member of the Society of Porphyrins and Phthalocyanines

Introduction:

Developing artificial photosynthetic technologies for converting solar energy to transportable, energy-dense fuels would be a major step towards meeting future human energy demands while also mitigating our impact on the environment [98]. Using the energy of sunlight to drive the conversion of water to oxygen and hydrogen offers an attractive means of converting and storing solar energy. A device capable of splitting water with light requires several key components including catalysts for the oxidation of water and production of hydrogen and photochemical systems capable of generating and stabilizing charge separated states. The latter are of interest in this work and require light absorbing materials judiciously chosen for their absorbance and redox properties.

To date, artificial photosynthetic systems have suffered from high cost, a need for rare materials, and/or low overall efficiencies for generating hydrogen [33,99]. An appealing route for incorporating potentially lower cost materials that enable fine-tuning of light absorption and the generation of long-lived, stable charged separated states lies in the use of organic dyes. Organic chromophores such as porphyrins, chlorins, perylenes, and phthalocyanines that bear carboxylic acid or phosphonate groups share many properties with natural dyes involved in photosynthesis and have demonstrated their viability in capturing and converting solar energy to electricity in dye sensitized solar cells as shown in recent reviews [100,101], [100-103].

Producing an efficient device for the generation of hydrogen from water with the only energy input coming from light will likely require a design utilizing two light absorbing photosystems, each of which harvests distinct regions of the solar spectrum [21,104]). When considering organic dyes for use in such a system, careful balance of the absorption and

redox properties of the dyes plays an integral role in the design; in a dual-threshold cell, the dyes must interact with separate parts of the spectrum while still accessing similar solar flux, and the excited state energies and redox properties of each must provide sufficient driving force for its electrochemical reaction of interest.

Phthalocyanines are good candidates for use in dual-threshold photoelectrochemical cells because of their high extinction coefficients, good chemical stability, and, most importantly, excited state energies that provide sufficient driving force for the cathodic reduction of protons to hydrogen. Octabutoxy silicon phthalocyanines are of particular interest because of their absorbance in the visible and near-IR and the opportunity to functionalize them by covalent attachment to the axial position of the central silicon atom.

Herein we explore axially modifying silicon phthalocyanines to introduce desirable functional groups for integrating these dyes into photoelectrochemical cells. Axial substitution is an attractive feature for multiple synthetic reasons: (i) having substituents above and below the macrocycle prevents aggregation and increases the solubility of these compounds [105], (ii) the ligands can be highly functionalized, and (iii) silicon phthalocyanines are robust under harsh chemical treatments. Axially coordinated ruthenium phthalocyanines have been shown to photo-inject electrons into TiO_2 [106], demonstrating that the electronic coupling of axially linked phthalocyanines is suitable for electron injection into semiconducting metal oxides. It is also worth noting that the use of non-peripheral octabutoxy groups helps to reduce aggregation [107], bathochromically-shifts the absorbance considerably relative to peripherally substituted analogues [108], and shifts the redox values to more negative potentials [109].

Here we report synthetic strategies for functionalizing far red absorbing octabutoxy silicon phthalocyanines for adsorption to metal oxide semiconductors. We have introduced phenyl or biphenyl axial substituents with ethyl carboxylic ester or diethyl phosphonate functional groups via a phenoxy linkage. Upon deprotection, the resulting carboxylate or phosphonate moieties would serve as anchoring groups to metal oxide semiconductors.

Results and Discussion:

Joyner et al. [110] first reported a protocol for displacing axial hydroxy ligands on silicon phthalocyanines using molten phenol and a few drops of pyridine. Herein we report an adaption of this method, which yields mono-phenoxy silicon phthalocyanines. Silicon insertion into the free-base octabutoxy phthalocyanine involved first using trichlorosilane in a mixture of dichloromethane and tributylamine to yield the dichloride silicon phthalocyanine in situ (Scheme 1). Displacement of the chloride ligands in a mixture of water and triethylamine produced the dihydroxy silicon phthalocyanine 1 with a 53% yield (Scheme 1). Monosilation of 1 took place in refluxing toluene with one equivalent of chlorotriethylsilane to yield 2 with a 76% yield (Scheme 1).

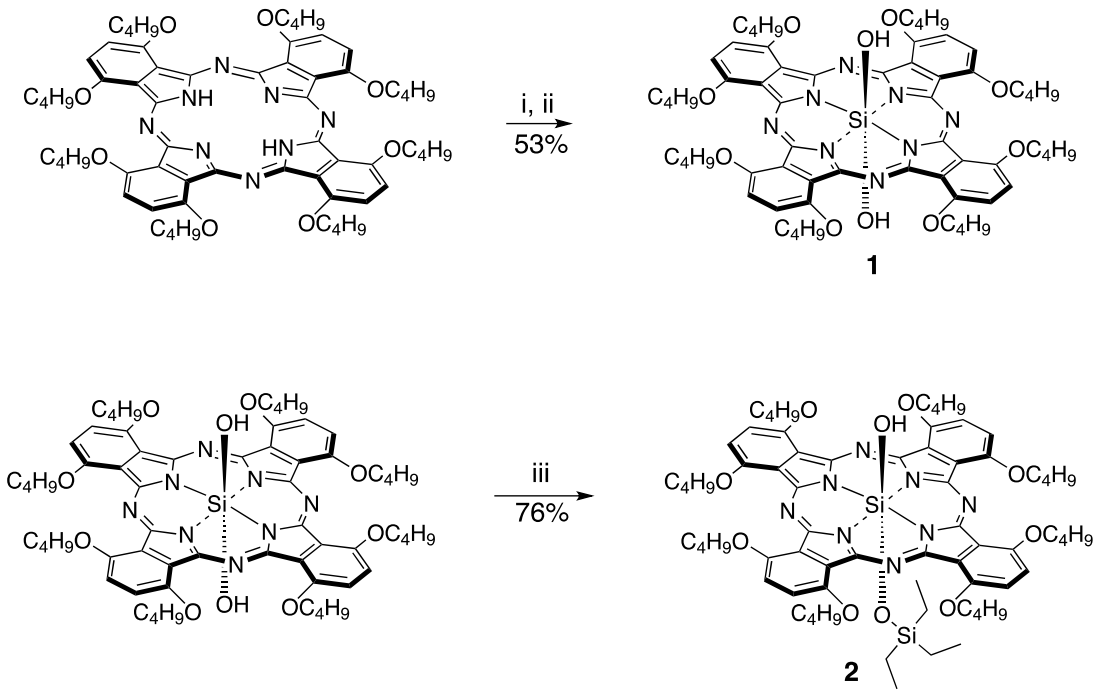

Scheme 1: Reaction conditions: i) $HSiCl_3$, TBA, CH_2Cl_2, rt, 18 h; ii) TEA, H_2O, rt, 3 h; iii) $ClSiEt_3$, toluene, pyridine, reflux, 45 min

The reaction was monitored via thin layer chromatography and quenched upon formation of traces of the disilylated silicon phthalocyanine. Diethyl 4'-hydroxybiphenyl-4-ylphosphonate 3 was prepared by an adaptation of the Hirao palladium-catalyzed cross-coupling reaction [111] in dry dimethylformamide using tris(dibenzylideneacetone)dipalladium(0) as the catalyst, diisopropylethylamine as the base, and 1,1'-bis(diphenylphosphino)ferrocene as the ligand (Scheme 2). The linkage of the corresponding phenols in compounds 4, 5, and 6 (Scheme 2 and 3) was done in pyridine at 55^{o}C for 48–60 hours. In all cases, two column-chromatography steps were necessary for purification of 4, 5, and 6 due to the tendency for streaking on silica gel. We started with a non-peripheral octaalkoxy substituted phthalocyanine for several reasons. Most importantly, alkoxy substituents aid in increasing the solubility of the phthalocyanine in organic solvents while inhibiting the tendency for aggregation [105,107,112]. Secondly, we have chosen octabutoxy groups located at the non-peripheral positions (1,4,8,11,15,18,22,25) because substitution at these sites has been shown to induce a greater shift on the absorption spectrum to longer wavelengths than octabutoxy groups on the peripheral positions [108].

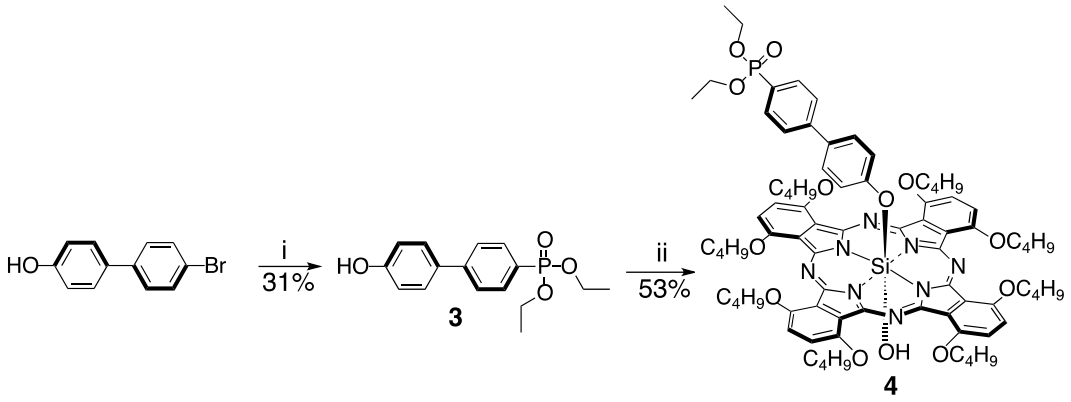

Scheme 2: Reaction conditions: i) dimethylformamide, diethylphosphite, diisopropylethylamine (Hünig's base), 1,1'-bis(diphenylphosphino)ferrocene, tris(dibenzylideneacetone)dipalladium(0), 110 ^{o}C, 24 h; ii) 1, pyridine, 55 ^{o}C, 48 h

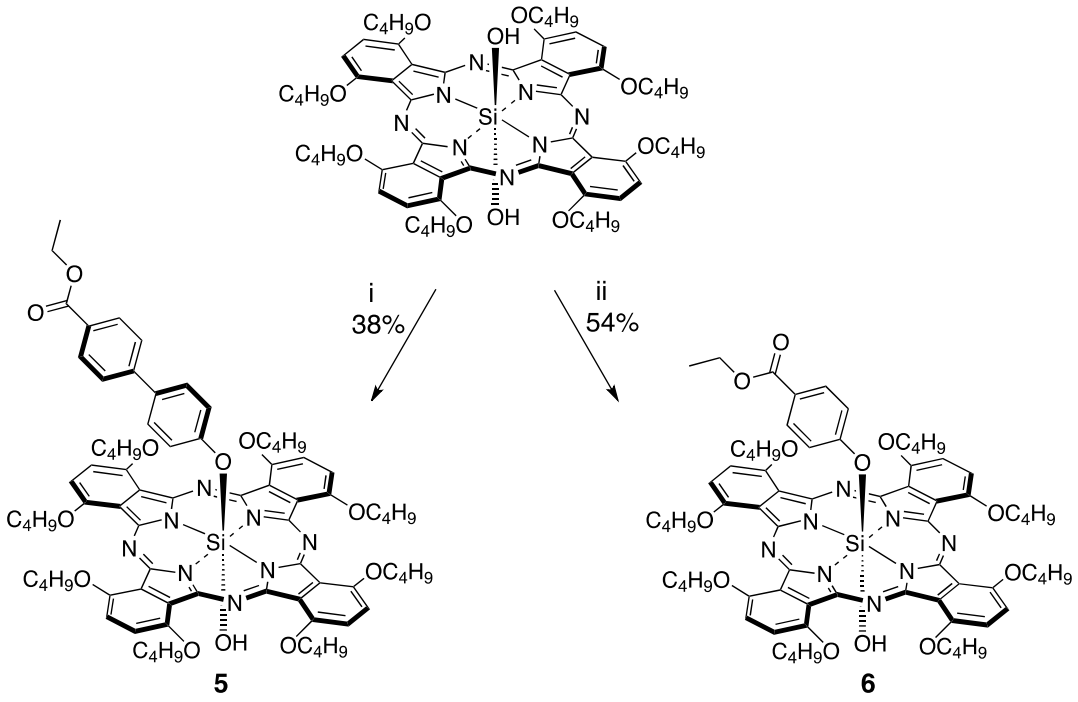

Scheme 3: Reaction conditions: i) ethyl 4'-hydroxybiphenyl-4-carboxylate, pyridine, 55 ^{o}C, 48 h; ii) ethyl 4-hydroxybenzoate, pyridine, 55 ^{o}C, 60 h

We have inserted silicon into the macrocycle of the phthalocyanine as this allows for axial covalent modification. Typically, axial modification of silicon phthalocyanines proceeds from the dichloride silicon phthalocyanine. However, we found the dichloride species to be unstable, possibly due to greater lability of the chloride ligands resulting from electron donating effects and increased solubility from the presence of the octabutoxy groups at the non-peripheral positions of the phthalocyanine macrocycle. Others have achieved the phenoxy linkage [105,109,113,114], but started from the non-substituted dichloride silicon phthalocyanine and allowed it to react with a strong base such as sodium hydride. Our method starts from the dihydroxy species, as demonstrated by Joyner and others [110,115], but requires only mild reaction conditions (such as lower temperatures), limited amounts of starting phenol, and allows use of phenols with chemically sensitive functional groups. Furthermore, it allows for the synthetic control necessary to produce the mono axial phenoxy substituted silicon phthalocyanine.

Initially we set out to synthesize mono-phenoxy phthalocyanine with the opposite face protected with a triethylsiloxyl group. This strategy resulted in two issues of concern: (i) the longest wavelength Q band was blue shifted in 2 with respect to 1 by 5 nm (Fig. 1), and, (ii) after the phenoxy group is coupled, the stability of the triethylsiloxyl group decreases as evidenced by difficulties in isolation. Therefore we decided to leave the second axial hydroxyl group unprotected.

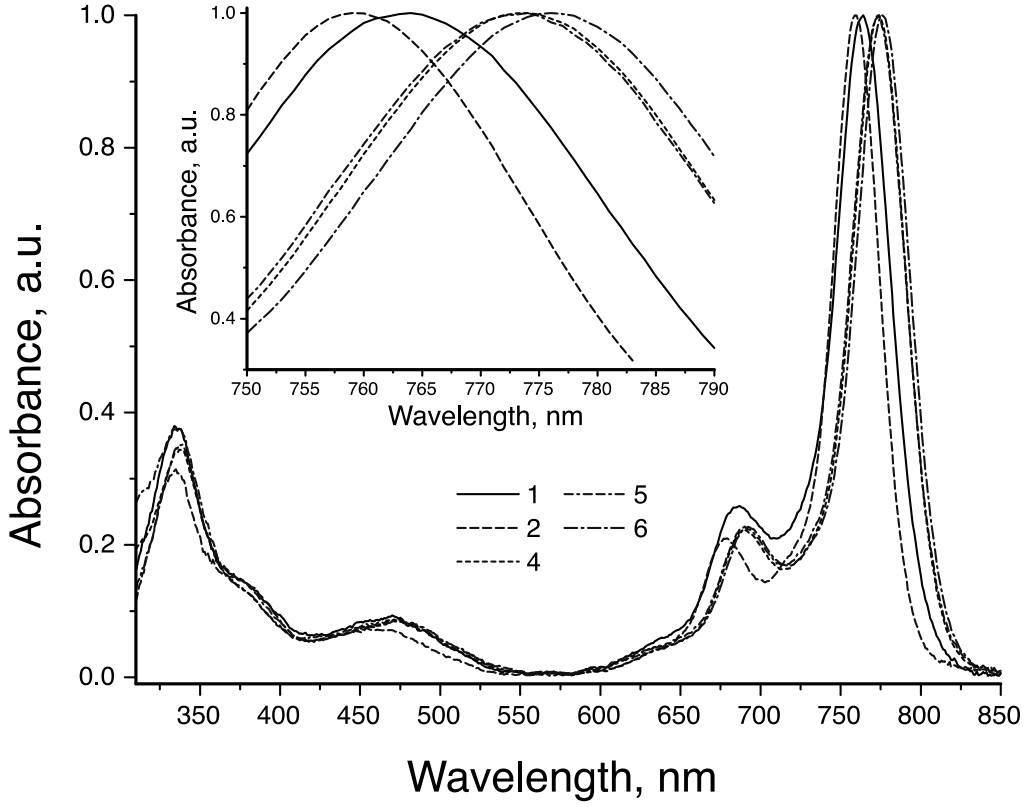

Figure 1: Normalized absorption spectra for phthalocyanine derivatives 1, 2, 4, 5, and 6. Inset shows a zoomed expanded view of the longest wavelength Q band of each derivative. Spectra were taken in distilled dichloromethane.

Ultraviolet-visible spectral analysis reveals a shift to longer wavelengths of the last Q band upon phenoxy displacement of the hydroxide. Compound 6 shows a bathochromic shift of 12 nm with respect to 1 (Fig. 1) with the last Q band occurring at 776 nm. Both 4 and 5 have the biphenyl linker and, although they bear different functional groups at the para position, their absorption properties are similar in that the last Q band is slightly shifted to shorter wavelengths in comparison with 6 but longer wavelengths with respect to 1 (Fig. 1). The absorbance of the last Q bands of 4 and 5 indicates that the ethyl carboxylic ester or diethyl phosphonate groups do not have as strong an influence on the absorbance presumably due to decoupling caused by the biphenyl linker.

The ^{1}H NMR spectra of 4, 5, and 6 show an upfield shift of the aromatic protons that are axial to the plane of the phthalocyanine. Aromatic protons ortho to the phenoxy linkage show signals at ~2.9 ppm, consistent with results from other studies [116]. The magnitude of the up field shift decreases as the location of the proton moves further away from the center of the phthalocyanine macrocycle which is in accordance with the literature [117-120]. The OH signal in the ^{1}H NMR of 2, 4, 5, and 6 could not be detected; Zhao et al. have observed similar effects [121]). Each target compound was characterized by matrix assisted laser desorption/ionization-time of flight (MALDI-TOF) mass spectroscopy. Trans-2-[3-(4-tert-butylphenyl)-2-methyl-2-propenylidene]malononitrile was found to be the best matrix and free-base 1,4,8,11,15,18,22,25-octabutoxyphthalocyanine was used as an internal reference.

An important aspect of evaluating dyes for photoelectrochemical applications lies in the determination of their redox properties in order to ensure that they can carry out the

photo-initiated electrochemical processes of interest. We are targeting silicon phthalocyanines in this work to drive the cathodic reduction of protons to hydrogen; their excited state redox potentials must be sufficiently negative to carry out this process, which at pH 7 occurs at –0.65 V vs. SCE. Determining the potentials for the oxidation and reduction of a dye, coupled with its absorption characteristics, allows approximation of its excited state redox potentials. Cyclic voltammetry experiments on the silicon phthalocyanine dyes synthesized for this work showed them to be good candidates for driving proton reduction. Figure 2 features cyclic voltammagrams for compounds 4, 5, and 6; the redox potentials for these compounds and dye 1 are listed in Table 1. Overall, the identity of the axial ligand to the silicon had minimal influence on the redox potentials of the phthalocyanines. For example, the potentials for the first oxidation differed by only 10 mV across the series. These molecules showed reversible first and second oxidations with anodic and cathodic peak separations (ΔE_p) near 60 mV, while the first reductions gave greater peak separations, implying more quasi-reversible character.

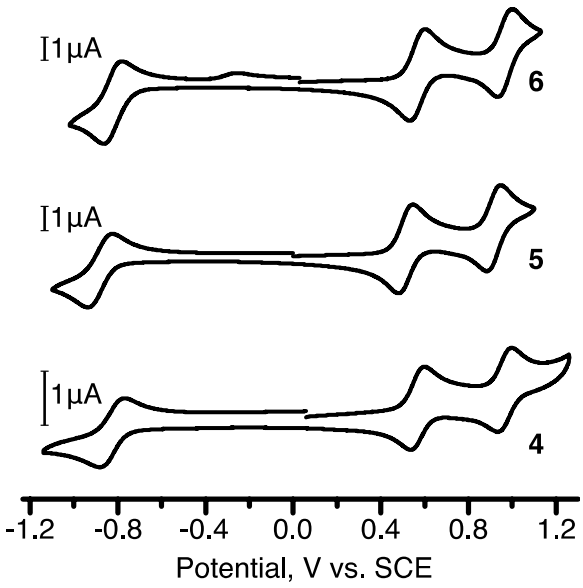

Figure 2: Cyclic voltammograms for compounds 4, 5, 6. All scans shown were taken at 100 mV/s in dichloromethane with 0.1 M tetrabutylammonium hexafluorophosphate. The identity of the phenoxy ligand had only subtle influence on the redox potentials as evidenced by the similarity of each scan.

Table 1: Redox values for the compounds 1, 4, 5, and 6. Potentials given are in reference to a standard calomel electrode (SCE). Peak separation (ΔE_p) of the anodic and cathodic scans is given for each process.

Compound	Ox(1), (ΔE_p)	Ox(2), (ΔE_p)	Red(1),
1	0.55 V, (64	0.95 V, (67	-0.84 V, (80
4	0.55 V, (63	0.96 V, (64	-0.90 V, (98
5	0.54 V, (64	0.96 V, (64	-0.83 V, (98
6	0.54 V, (68	0.93 V, (67	-0.82 V, (80

With an eye toward the eventual testing of these dyes in a dual-threshold photoelectrochemical water splitting cell, we are most interested in the potential of the first oxidation. With midpoint potentials near 0.55 V vs. SCE and longest-wavelength photon absorption of ~1.6 eV, these dyes will have adequate excited state energies to sensitize TiO_2 or other semiconducting metal oxides with a more negative conduction band [122]. Future work will aim at investigating the efficiency of electron injection into metal oxide semiconductors by these axial functionalized phthalocyanines, and their ability to drive the formation of hydrogen in a photoelectrochemical cell.

Experimental:

Electrochemistry

All electrochemical experiments were carried out with a CH Instruments 760D potentiostat. All samples were analyzed in a closed glass cell under an argon atmosphere with a three electrode setup. A working platinum disc electrode was used in concert with a platinum mesh counter electrode and a silver quasi-reference electrode. The potential of the silver quasi-reference electrode was calibrated versus the ferrocenium/ferrocene (Fc^+/Fc) couple at the conclusion of each series of experiments with the Fc^+/Fc couple taken as 0.45 V vs. SCE. Distilled dichloromethane was used as the working solvent along with 0.1 M tetrabutylammonium hexafluorophosphate as supporting electrolyte, which was doubly recrystallized from ethanol and dried under reduced pressure with heat prior to use.

Materials

Dichloromethane used for synthesis and electrochemistry was refluxed over calcium hydride followed by distillation and storage over activated 4 Å molecular sieves.

Pyridine and dimethylformamide were dried over activated 4 Å molecular sieves. Tributylamine was passed though activated alumina and stored overnight over activated 4 Å molecular sieves. Toluene for synthesis was distilled from phosphorus pentoxide and stored over activated 4 Å molecular sieves. Toluene, ethyl acetate and hexane used for column chromatography were distilled. Triethylamine was purchased from Alfa Aesar and used without further purification. Trichlorosilane, 1,4,8,11,15,18,22,25-octabutoxy-29H,31H-phthalocyanine, chlorotriethylsilane, diethylphosphite, diisopropylethylamine (Hünig's base), 1,1'-bis(diphenylphosphino)ferrocene, 4'-bromo-(1,1'-biphenyl)-4-ol, ethyl 4'-hydroxybiphenyl-4-carboxylate, ethyl 4-hydroxybenzoate, and tris(dibenzylideneacetone)dipalladium(0) were purchased from Sigma-Aldrich and used without further purification. Tetrabutylammonium hexafluorophosphate was also purchased from Sigma-Aldrich. Thin layer chromatography plates (250 micron), both fluorescent and non-fluorescent, were purchased from Analtech, Inc. Silica gel (SiliaFlash F60 40-63 μm) used for column chromatography was purchased from SILICYCLE.

General

^{1}H NMR spectra were recorded on a 400 MHz Varian Liquid-State spectrometer. NMR samples were dissolved in deuteriochloroform with 0.03% tetramethylsilane as an internal reference. Mass spectra were obtained on an Applied Biosystems Voyager-DE STR matrix-assisted laser desorption/ionization time-of-flight spectrometer (MALDI-TOF). The matrix used for all mass spectra samples was trans-2-[3-(4-tert-butylphenyl)-2-methyl-2-propenylidene]malononitrile. Ultraviolet-visible ground state absorption

spectra were measured using a Shimadzu UV2100U spectrophotometer. All ultraviolet-visible samples were dissolved in distilled dichloromethane.

Synthesis

Dihydroxy-1,4,8,11,15,18,22,25-octabutoxyphthalocyaninatosilicon(IV) (1). A portion of 1,4,8,11,15,18,22,25-octabutoxy-29H,31H-phthalocyanine (1.1 g, 1.0 mmol) was dissolved in dry dichloromethane (240 mL) and dry tributylamine (24 mL). The solution was degassed with argon for 10 min, followed by addition of trichlorosilane (2.4 mL, 23.8 mmol) and allowed to stir at room temperature for 18 h under argon. Triethylamine (80 mL) was added carefully, followed by H_2O (40 mL) and the mixture was allowed to stir at room temperature for an additional 3 h. To neutralize the amines, aqueous HCl (12 M, 58 mL) was added until the solution was acidic, and the solution was allowed to stir for an additional 1 h. The mixture was filtered and the solid was washed with dichloromethane (500 mL). The mother liquor was separated and the organic layer was washed twice with HCl (1 M, 100 mL) followed by 3 washes with H_2O. The organic layer was dried over sodium sulfate and the solvent was removed under reduced pressure. Column chromatography was done using silica gel with ethyl acetate/toluene (50:50) as eluent, which afforded a green solid. Yield 615 mg (53%), ^{1}H NMR (400 MHz; $CDCl_3$; 0.03% Me_4Si): δ_H, ppm -2.54 (2H, bs, -OH), 1.08 (24H, t, -CH_2-CH_2-CH_2-CH_3, J = 7.2 Hz), 1.66 (16H, sex., -CH_2-CH_2-CH_2-CH_3, J = 7.6 Hz), 2.20 (16H, p, -CH_2-CH_2-CH_2-CH_3, J = 7.6 Hz), 4.87 (16H, t, -CH_2-CH_2-CH_2-CH_3, J = 7.2 Hz), 7.64 (8H, s, PcH). UV-vis (CH_2Cl_2): λ_{max}, nm 334, 470, 687, 764. MS (MALDI-TOF): m/z calcd. for $C_{64}H_{82}N_8O_{10}Si$ 1150.59, obsd. 1150.59.

Triethylsilylhydroxy-1,4,8,11,15,18,22,25-octabutoxyphthalocyaninatosilicon(IV) (2). A portion of (1) (70 mg, 0.06 mmol) was dissolved in dry toluene (30 mL) and dry pyridine (4 mL) and degassed for 15 min. Chlorotriethylsilane (10.2 μL, 0.06 mmol) was added and the solution was allowed to reflux for 45 min. Once formation of bis-triethylsilyl phthalocyanine was observed (monitored by TLC), the solvent was removed under reduced pressure and column chromatography was done using silica gel with toluene/ethyl acetate (65:35) as eluent, which afforded a green solid. Yield 59 mg (76%), ^{1}H NMR (400 MHz; $CDCl_3$; 0.03% Me_4Si): δ_H, ppm -2.14 (6H, q, -CH_2-CH_3, J = 8 Hz), -0.98 (9H, t, -CH_2-CH_3, J = 8 Hz), 1.04 (24H, t, -CH_2-CH_2-CH_2-CH_3, J = 7.6 Hz), 1.63 (16H, sex., -CH_2-CH_2-CH_2-CH_3, J = 7.6 Hz), 2.15 (16H, p, -CH_2-CH_2-CH_2-CH_3, J = 7.2 Hz), 4.88 (16H, m, -CH_2-CH_2-CH_2-CH_3), 7.65 (8H, s, PcH). UV-vis (CH_2Cl_2): λ_{max}, nm 335, 465, 679, 759. MS (MALDI-TOF): m/z calcd. for $C_{70}H_{96}N_8O_{10}Si_2$ 1264.68, obsd. 1264.68.

Diethyl (4'-hydroxy-[1,1'-biphenyl]-4-yl)phosphonate (3). A portion of 4'-bromo-(1,1'-biphenyl)-4-ol (996 mg, 4.0 mmol) was dissolved in dimethylformamide (15 mL) and the solution was degassed with argon for 15 min. To that solution was added diethylphosphite (662 mg, 4.8 mmol), diisopropylethylamine (Hünig's base) (0.9 mL), 1,1’-bis(diphenylphosphino)ferrocene (24.3 mg, 0.044 mmol) and tris(dibenzylideneacetone)dipalladium(0) (26.9 mg, 0.040 mmol, 1 mol%). The solution was allowed to stir at 110 ^{o}C for 24 h under argon. The solvent was removed under reduced pressure and the red-yellow oil dissolved in ethyl acetate, H_2O was added (50 mL) and the aqueous layer was washed 4 times with ethyl acetate followed by 1 wash with brine, dried over magnesium sulfate and concentrated. Column chromatography was

done using silica gel with ethyl acetate/hexane (70:30) as eluent, which afforded a yellow solid. Yield 378 mg (31%), ^{1}H NMR (400 MHz; $CDCl_3$; 0.03% Me_4Si): δ_H, ppm 1.35 (6H, t, -CH_2 –CH_3, J = 7.2 Hz), 4.15 (4H, m, -CH_2-CH_3), 6.87 (2H, d, Ar-phenoxy, J = 8.8 Hz), 7.47 (2H, d, Ar-phenoxy, J = 8.8 Hz), 7.63 (2H, m, Ar-phosphonate), 7.84 (2H, m, Ar-phosphonate). MS (MALDI-TOF): m/z calcd. for $C_{16}H_{19}O_4P$ 306.10, obsd. 307.11.

4'-(Diethoxyphosphoryl)biphenyl-4-olatehydroxy-1,4,8,11,15,18,22,25-octabutoxyphthalocyaninatosilicon(IV) (4). A portion of (1) (31 mg, 0.027 mmol) was dissolved in dry pyridine (10 mL), to this solution was added diethyl 4'-hydroxybiphenyl-4-ylphosphonate (3) (82 mg, 0.27 mmol) and the solution was degassed with argon for 10 min. The solution was allowed to stir at 55 ^{o}C for 48 h under argon. The solvent was removed under reduced pressure and two column chromatography steps were needed to purify the desired product using silica gel. The first chromatography step was with toluene/ethyl acetate (60:40) and the second with toluene/ethyl acetate (75:25) to afford a green solid. Yield 20 mg (53%), ^{1}H NMR (400 MHz; $CDCl_3$; 0.03% Me_4Si): δ_H, ppm 1.04, (24H, t, -CH_2-CH_2-CH_2-CH_3, J = 7.6 Hz), 1.22 (6H, t, -CH_2-CH_3, J = 6.8 Hz), 1.62 (16H, sex., -CH_2-CH_2-CH_2-CH_3, J = 7.6 Hz), 2.14 (16H, p, -CH_2-CH_2-CH_2-CH_3, J = 8 Hz), 2.94 (2H, d, Ar-phenoxy, J = 8.8 Hz), 3.98 (4H, m, -CH_2-CH_3), 4.82 (16H, m, -CH_2-CH_2-CH_2-CH_3), 5.96 (2H, d, Ar-phenoxy, J = 8.8 Hz), 6.87 (2H, m, Ar-phosphonate), 7.49 (2H, m, Ar-phosphonate) 7.65 (8H, s, PcH). UV-vis (CH_2Cl_2): λ_{max}, nm 339, 472, 691, 774. MS (MALDI-TOF): m/z calcd. for $C_{80}H_{99}N_8O_{13}PSi$ 1438.68, obsd. 1438.69 and 1133.59 (M-phenoxy).

4'-(Ethoxycarbonyl)biphenyl-4-olatehydroxy-1,4,8,11,15,18,22,25-octabutoxyphthalocyaninatosilicon(IV) (5). A portion of (1) (48 mg, 0.042 mmol) was dissolved in dry pyridine (10 mL) and the solution degassed for 10 min. To this solution was added ethyl 4'-hydroxybiphenyl-4-carboxylate (51 mg, 0.21 mmol) and allowed to stir at 55 ^{o}C for 48 h under argon. The solvent was removed under reduced pressure and column chromatography was done using silica gel with toluene/ethyl acetate (65:35) and then a second column chromatography step using toluene/ethyl acetate (75:25) as eluent, which afforded a green solid. Yield 22 mg (38%), ^{1}H NMR (400 MHz; $CDCl_3$; 0.03% Me_4Si): δ_H, ppm 1.04, (24H, t, -CH_2-CH_2-CH_2-CH_3, J = 7.6 Hz), 1.31 (3H, t, -CH_2-CH_3, J = 7.2 Hz), 1.62 (16H, sex., -CH_2-CH_2-CH_2-CH_3, J = 7.6 Hz), 2.14 (16H, p, -CH_2-CH_2-CH_2-CH_3, J = 8 Hz), 2.93 (2H, d, Ar-phenoxy, J = 8.8 Hz), 4.27 (2H, q, -CH_2-CH_3, J = 7.2 Hz), 4.81 (16H, m, -CH_2-CH_2-CH_2-CH_3), 5.98 (2H, d, Ar-phenoxy, J = 8.4 Hz), 6.83 (2H, d, Ar-benzoate, J = 8.8 Hz), 7.64 (8H, s, PcH), 7.72 (2H, d, Ar-benzoate, J = 8.4 Hz). UV-vis (CH_2Cl_2): λ_{max}, nm 338, 471, 690, 774. MS (MALDI-TOF): m/z calcd. for $C_{79}H_{94}N_8O_{12}Si$ 1374.68, obsd. 1374.68.

4-(Ethoxycarbonyl)phenolatehydroxy-1,4,8,11,15,18,22,25-octabutoxyphthalocyaninatosilicon(IV) (6). A portion of (1) (48 mg, 0.042 mmol) was dissolved in dry pyridine (12 mL) and the solution degassed for 10 min. To this solution was added ethyl 4-hydroxybenzoate (35 mg, 0.21 mmol) and was allowed to stir at 55 ^{o}C for 60 h under argon. The solvent was removed under reduced pressure and column chromatography was done using silica gel with toluene/ethyl acetate (70:30) as solvent. A second column chromatography step using toluene/ethyl acetate (80:20) as eluent, afforded a green solid. Yield 29 mg (54%), ^{1}H NMR (400 MHz; $CDCl_3$; 0.03% Me_4Si):

δ_H, ppm 1.07, (24H, t, $-CH_2-CH_2-CH_2-CH_3$, J = 7.2 Hz), 1.34 (3H, t, $-CH_2-CH_3$, J = 7.2 Hz), 1.64 (16H, sex., $-CH_2-CH_2-CH_2-CH_3$, J = 7.2 Hz), 2.16 (16H, p, $-CH_2-CH_2-CH_2-CH_3$, J = 8 Hz), 2.87 (2H, d, Ar-phenoxy, J = 8.8 Hz), 3.91 (2H, q, $-CH_2-CH_3$, J = 6.8 Hz), 4.80 (16H, m, $-CH_2-CH_2-CH_2-CH_3$), 6.41 (2H, d, Ar-phenoxy, J = 8.8 Hz), 7.65 (8H, s, PcH). UV-vis (CH_2Cl_2): λ_{max}, nm 337, 471, 692, 776. MS (MALDI-TOF): m/z calcd. for $C_{73}H_{90}N_8O_{12}Si$ 1298.64, obsd. 1298.65 and 1133.58 (M-phenoxy).

Conclusion:

The synthesis of silicon octabutoxy phthalocyanines bearing axial ethyl carboxylic esters and diethylphosphonate groups via a phenoxy linkage can be accomplished in a few synthetic steps, from a variety of phenols, and under mild conditions. Additionally, this approach allows for isolation of the mono axial functionalized phenoxy phthalocyanines. Strongly red absorbing phthalocyanines are good candidates for dual-threshold solar cells and the use of non-peripheral octabutoxy groups as well as the substitution of phenols on the axial position of silicon phthalocyanines, as demonstrated with 4, 5, and 6, helps to further shift their absorption to the near infrared. Furthermore, the phenoxy substituted phthalocyanines prepared in this study demonstrated potentials for the first oxidation near 0.55 V vs. SCE, making them good candidates for photosensitizing low-potential conduction band metal oxide semiconductors. The ability to use low-potential conduction band materials will provide more driving force for the generation of hydrogen from water. By incorporating phenoxy ligands with functional groups that can anchor to metal oxide semiconductors, we are progressing toward the use of these dyes in dual-threshold photoelectrochemical cells designed to carry out overall water splitting with sunlight. Moreover the ability to bind a

variety of phenoxy derivatives in the axial position can be exploited to control the macrocycle to metal-oxide electronic coupling and consequently the efficiency of the sensitization process. The synthetic strategy presented offers a route to obtaining phthalocyanines with axial groups for anchoring to semiconducting metal oxides from the readily obtainable bis-hydroxy octabutoxy silicon phthalocyanines.

Acknowledgments:

This work was supported in part by a grant from the National Science Foundation, USA (DMR-0908656), the Agencia Nacional de Promoción Científica y Tecnológica, Argentina (PRH 23 PICT 140/08), the Consejo Nacional de Ciencia y Tecnología, México (101939), the National Science and Engineering Research Council (Canada) and a Tomlinson Award, McGill University. The research of J.J.B, B.D.S, D.G. and A.M. was supported as part of the Center for Bio-Inspired Solar Fuel Production, an Energy Frontier Research Center funded by the U.S. Department of Energy, Office of Science, Office of Basic Energy Sciences under Award Number DE-SC0001016. R.E.P. is a permanent research staff of CONICET (Consejo Nacional de Investigaciones Científicas y Técnicas, Argentina). We would also like to acknowledge John Lopez and Zach Laughrey from the ASU Proteomics and Protein Chemistry Facility for obtaining MALDI-TOF mass spectra. B.D.S thanks Science Foundation Arizona for their support of this work through a graduate research fellowship.

CHAPTER 4

PERYLENES FOR ELECTRON TRANSFER STUDIES

4.1 Spectral Characteristics and Photosensitization of TiO_2 Nanoparticles in Reverse Micelles by Perylenes

Laura I. Hernández[1], Robert Godin[2], Jesse J. Bergkamp[3], Manuel J. Llansola Portolés[3], Benjamin D. Sherman[3], John Tomlin[3], Gerdenis Kodis[3], Dalvin D. Méndez-Hernández[3], Sonia Bertolotti[1], Carlos A. Chesta[1], Ernesto Mariño-Ochoa[4], Ana L. Moore[3], Thomas A. Moore[3], Gonzalo Cosa[2], Rodrigo E. Palacios[1]

[1] Departamento de Química, Facultad de Ciencias Exactas Físico-Químicas y Naturales, Universidad Nacional de Río Cuarto, Río Cuarto, Córdoba 5800, Argentina

[2] Department of Chemistry and Center for Self Assembled Chemical Structures (CSACS/CRMAA), McGill University, Otto Maass Chemistry Building, 801 Sherbrooke Street West, Montreal, QC, H3A 0B8, Canada

[3] Department of Chemistry and Biochemistry, Center for Bioenergy and Photosynthesis, Arizona State University, Tempe, Arizona 85287-1604, USA

[4] Department of Chemistry, Tecnológico de Monterrey, Campus Monterrey, Monterrey, NL, 64849, México

*Corresponding author e-mail: rpalacios@exa.unrc.edu.ar (Rodrigo E. Palacios).

Citation:

Hernández, L. I.; Godin, R.; Bergkamp, J. J.; Llansola Portolés, M. J.; Sherman, B. D.; Tomlin, J.; Kodis, G.; Méndez-Hernández, D. D.; Bertolotti,

S.; Chesta, C. A.; Mariño-Ochoa, E.; Moore, A. L.; Moore, T. A.; Cosa, G.; Palacios, R. E. Spectral Characteristics and Photosensitization of TiO_2 Nanoparticles in Reverse Micelles by Perylenes. *J Phys Chem B* **2013**, *117*, 4568–4581.

My contribution to this work was focused on the synthesis of the perylene dyes and aiding in the editing process

Abstract:

We report on the photosensitization of titanium dioxide nanoparticles (TiO_2 NPs) synthesized inside AOT (bis(2-ethylhexyl) sulfosuccinate sodium salt) reverse micelles following photoexcitation of perylene derivatives with dicarboxylate anchoring groups. The dyes, 1,7-dibromoperylene-3,4,9,10-tetracarboxy dianhydride (1), 1,7-dipyrrolidinylperylene-3,4,9,10-tetracarboxy dianhydride (2), and 1,7-bis(4-tert-butylphenyloxy)perylene-3,4,9,10-tetracarboxy dianhydride (3), have a considerably different driving force for photoinduced electron injection into the TiO_2 conduction band as estimated by electrochemical measurements and quantum mechanical calculations. Fluorescence anisotropy measurements indicate that dyes 1 and 2 are preferentially solubilized in the micellar structure creating a relatively large local concentration that favors the attachment of the dye to the TiO_2 surface. The binding process was followed by monitoring the hypsochromic shift of the dye absorption spectra over time for 1 and 2. Photoinduced electron transfer from the singlet excited state of 1 and 2 to the TiO_2 conduction band (CB) is indicated by emission quenching of the TiO_2-bound form of the dyes and confirmed by transient absorption measurements of the radical cation of the dyes and free carriers (injected electrons) in the TiO_2 semiconductor. Steady state and transient spectroscopy indicate that dye 3 does not bind to the TiO_2 NPs and does not

photosensitize the semiconductor. This observation was rationalized as a consequence of the bulky t-butylphenyloxy groups which create a strong steric impediment for deep access of the dye within the micelle structure to reach the semiconductor oxide surface.

Keywords:

Photo-induced charge separation, semiconductor nanoparticle, dianhydride perylene, perylene radical cation, organic-inorganic electron transfer, ultrafast transient absorption, time resolved fluorescence anisotropy.

Introduction:

The study of interfacial electron transfer (IET) in dye – semiconductor nanoparticle systems is an area of considerable research interest from both fundamental and practical points of view [123-128]. Modification of metal oxide semiconductors with organic dyes is a well-known method to extend their photoresponse to visible light. Application of metal oxide/dye systems has been extensively demonstrated in a variety of organic – electronic devices such as dye-sensitized solar cells (DSSC) [28,129-133], heterogeneous photocatalysis [134-139], and chemical sensing [140-144]. The current need for performance improvement in many of these devices entails a better understanding of the IET process which plays a central role in device operation [133,145-149].

Dye to semiconductor nanoparticle (NP) photoinduced electron transfer has been widely studied in nanostructured metal oxide semiconductor films where the dye molecules are deposited in a relatively uncontrolled manner that leads to a number of physically adsorbed and non-bound aggregated dyes with poor electronic coupling with the semiconductor [150]. A large number of the electron transfer studies on these systems have been performed using steady state and time resolved UV-Vis spectroscopic techniques. The results obtained usually show complex kinetics and spectra due to the heterogeneous nature of the dye-NP binding, the size and crystallinity of the semiconductor NPs, scattering effects of the nanostructured film, and the presence of unbound trapped dye and dye aggregates [145,151-154]. The use of well characterized dye-sensitized NP suspensions can help to overcome many of these difficulties (by reducing scattering effects and providing a more homogeneous set of semiconductor NPs) and accordingly a large number of studies have been carried out on such systems [126-

[128,145,147,155-184]. In some of these studies well dispersed and homogeneous semiconductor particles suspensions were obtained via a microemulsion method [161,174,175,178,180].

Perylene based dyes have been extensively explored as photosensitizers for DSSC because they absorb strongly in the visible, are chemically photostable and amenable for fine tuning their light absorbing and redox properties through structural modifications [185-196]. Additionally, the relatively low number of excited state relaxation pathways in perylenes, as compared to the prototypical ruthenium based dyes, facilitates the study of IET. [196]) Binding of perylene derivatives to TiO_2 has been achieved through carboxylic acid and dicarboxylic acid groups derived from anhydrides [187-193,197,198]. The nature of the binding and the electronic coupling between the dye and the semiconductor has been shown to influence the dye excited state properties and IET behavior. [187,188,190,197-199] Binding of perylene derivatives to metal NPs and metal-oxide and nanorods has also being achieved through thiol and sulfide groups, respectively [200-202].

Herein we report studies of the sensitization of TiO_2 nanoparticles in a reverse micelle suspension by perylene dye derivatives. The perylene dyes used in this study, (1,7-dibromoperylene-3,4,9,10-tetracarboxy dianhydride (1), 1,7-dipyrrolidinylperylene-3,4,9,10-tetracarboxy dianhydride (2), and 1,7-bis(4-tert-butylphenyloxy)perylene-3,4,9,10-tetracarboxy dianhydride (3), contain cyclic anhydride moieties which hydrolyze to yield two carboxylic acid groups that serve as anchoring groups to the TiO_2 surface. Steady state and transient spectroscopic results indicate that a large portion of dyes 1 and 2 are attached to the TiO_2 NPs surface and can effectively initiate IET. On the other hand spectroscopic results show inefficient binding of dye 3 to the semiconductor surface and

lack of photoinduced electron transfer indicating that the bulky structure of the dye hampers the binding process within the micelle-TiO_2 NP structure.

Experimental and Theoretical Methods

Materials.

Titanium tetraisopropoxide (TTIP, ≥97.0%), isopropanol (anhydrous, 99.5%), 3,4,9,10-perylenetetracarboxylic dianydride (97%), 2,6-diisopropylaniline (97%), pyrrolidine (99%), and bis(2-ethylhexyl) sulfosuccinate sodium salt (AOT, 98%), were purchased from Sigma-Aldrich and used as received. Anhydrous tert-butyl alcohol was purchased from Alfa-Aesar and used as received. Thin layer chromatography plates (250 micron), with fluorescent and non-fluorescent indicators, were purchased from Analtech, Inc. Silica gel (SiliaFlash F60 40-63 μm) used for column chromatography was purchased from SILICYCLE. Syringe PTFE membrane (200 nm pore) filters: disposable assemblies (PALL, Acrodisc. CR 25 mm) and disposable membranes (Microclar, T02013WPH) on a re-usable filter holder (Cole-Palmer, CZ-02928-10) were used interchangeably. N-heptane (HPLC grade), ethanol (anhydrous, HPLC grade), and potassium hydroxide (KOH, ACS reagent grade) were purchased from Merk. Perchloric acid (ACS reagent grade) was purchased from Taurus. Ultrapure water (18Ω, Millipore) and bottled water (Sintorgan, HPLC grade) were used interchangeably. Tetrahydrofuran (THF) (Sintorgan, HPLC) was distilled over metallic sodium with benzophenone. All solvents used for column chromatography were distilled before use.

Synthesis.

1,7-Dibromoperylene-3,4,9,10-tetracarboxy dianhydride (1). Compound 1 was obtained following a literature procedure [198].

1,7-Dipyrrolidinylperylene-3,4,9,10-tetracarboxy dianhydride (2). Compound 2 was prepared following slightly modified reported protocols. First N,N'-bis(2,6-diisopropylphenyl)-1,7-bis(pyrrolidin-1-yl)perylene-3,4,9,10-tetracarboxylic acid bisimide was prepared [198]. This was followed by base hydrolysis in tert-butyl alcohol and purification by column chromatography using 2% ethyl acetate in chloroform as eluent on silica gel [203] to yield compound 2. All compounds were characterized by ^{1}H NMR and MALDI-TOF mass spectrometry; the spectra were identical to that previously reported.

1,7-Bis(4-tert-butylphenyloxy)perylene-3,4,9,10- tetracarboxy dianhydride (3). Compound 3 was prepared following a modified published procedure. [204] A portion of compound 1 (8 g, 14.5 mmol), 4-tert-butlyphenol (7.2 g, 48.0 mmol), and cesium carbonate (9.5 g, 29.1 mmol) were dissolved in dimethylformamide (485 mL), and heated at reflux for 4 h under nitrogen. The reaction mixture was poured into water (200 mL), and neutralized with aqueous 1 M HCl. The precipitate was filtered and washed repeatedly with water and then methanol to give a crude solid. A 100 mg portion was then purified by preparatory TLC, which was followed by flash column chromatography on silica gel using chloroform as the eluent to afford a red solid (15.4 mg, 0.022 mmol, 15.4% yield). ^{1}H NMR (Chloroform-d, 400MHz): δ_H, ppm 9.64 (d, J=8.2 Hz, 2 H), 8.71 (d, J=8.2 Hz, 2 H), 8.28 (s, 2 H), 7.52 (d, J=8.6 Hz, 4 H), 7.13 (d, J=8.6 Hz, 4 H),1.39 (s, 18 H).

Titanium dioxide Nanoparticles (TiO_2 NP)

The synthesis was carried out by the hydrolysis of TTIP inside the water pool of AOT reverse micelles suspended in n-heptane. [174] In this system the micelles act as nanoreactors, where the hydrolysis reaction takes place, preventing the formation of TiO_2 nanoparticle aggregates. A micellar suspension of w_0= 1 (w_0= [H_2O]/[AOT]) was prepared by adding 220 μL of aqueous $HClO_4$ (0.02 M) to 30 mL of AOT solution (0.4 M) in n-heptane under continuous stirring. A 0.2 mL aliquot of a TTIP stock solution (0.136 M) in anhydrous isopropanol was added dropwise to 30 mL of the micellar suspension under mild agitation at room temperature. Stirring was continued for 20 min to obtain a clear micellar suspension containing TiO_2 NPs (see Figure 2, insert).

Micelles without TiO_2 NPs

A control sample of micelles without TiO_2 NPs was prepared following exactly the same procedure described above except for the addition of TTIP. We estimate a significant proton concentration inside the reverse micelle water pool based on the concentration of $HClO_4$ in the aqueous solution used for micelle formation. However, calculation of pH is not valid in these systems where the nanoscopic size of the water pool limits the number of avalible water molecules. **[205]**

Instruments and measurements.

Steady state absorption

Spectra were recorded in 1 cm path length cuvettes with the following spectrophotometers: diode array HP 8452, Shimadzu - UV-IR (2041PC), and Hitachi double beam UV/Vis spectrophotometer (U-2800).

Steady state fluorescence

Spectra and fluorescence anisotropy measurements were obtained with the following spectrofluorometers: Horiba FluoroMax-4 and PTI Quantamaster 40, both equipped with motorized polarizers. To compare emission intensities of samples measured with absorbances not matched at the excitation wavelength (Abs(λ_{ex})), the corrected emission intensity of a given sample ($I_{corr}(\lambda_{em})$) was calculated from the observed emission intensity ($I_{obs}(\lambda_{em})$) using Equations 1 and 2: [206])

(1) $$I_{A,corr}(\lambda_{em}) = \left(\frac{Abs_B(\lambda_{ex})}{Abs_A(\lambda_{ex})}\right) I_{A,obs}(\lambda_{em}) \cdot 10^{\left(\frac{Abs_A(\lambda_{ex}) + Abs_A(\lambda_{em})}{2}\right)}$$

and

(2) $$I_{B,corr}(\lambda_{em}) = I_{B,obs}(\lambda_{em}) \cdot 10^{\left(\frac{Abs_B(\lambda_{ex}) + Abs_B(\lambda_{em})}{2}\right)}$$

where λ_{ex} and λ_{em} are excitation and emission wavelengths respectively and the subscripts A and B correspond to the different samples for which the emission intensity is compared.

Time resolved fluorescence

Fluorescence lifetime measurements were performed with a Time-Correlated Single Photon Counting (TC-SPC) system. The excitation source was a fiber supercontinuum laser based on a passive mode-locked fiber laser and a high-nonlinearity photonic crystal fiber supercontinuum generator (Fianium SC450). The laser provides 6 ps pulses at a repetition rate variable between 0.1 – 40 MHz. The laser output was sent through an Acousto-Optical Tunable Filter (Fianium AOTF) to obtain excitation pulses at the desired wavelength. Fluorescence emission was collected at 90° and detected using a double-grating monochromator (Jobin-Yvon, Gemini-180) and a microchannel plate photomultiplier tube

(Hamamatsu R3809U-50). The polarization of the emission was 54.7° relative to that of the excitation. Data acquisition was done using a single photon counting card (Becker-Hickl, SPC-830). The IRF had a FWHM of ~ 50 ps, measured from the scattering of sample at the excitation wavelength. The data was globally fitted as sum of exponential decays including IRF deconvolution using locally written software (ASUFIT) (www.public.asu.edu/~laserweb/asufit/asufit.html) developed in a MATLAB environment (Mathworks Inc.).

Time resolved absorption

Femtosecond to nanosecond transient absorption measurements were acquired with a kilohertz pulsed laser source and a pump-probe optical setup. Laser pulses of 100 fs at 800 nm were generated from an amplified, mode-locked titanium sapphire kilohertz laser system (Millennia/Tsunami/Spitfire, Spectra Physics). Part of the laser pulse energy was sent through an optical delay line and focused on to a 2 mm sapphire plate to generate a white light continuum for probe beam. The remainder of the pulse energy was used to pump an optical parametric amplifier (Spectra Physics) to generate excitation pulses at different wavelengths, which were modulated using a mechanical chopper. The excitation intensity was adjusted using a continuously variable neutral density filter. The probe beam was sent through a monochromator (SP150, Action Res. Corp.) and recorded by a diode detector (Model 2032, New Focus Inc.) and box car (SR250, Stanford Research Systems). Instrument response function was ca. 200 fs.

Nanosecond transient absorption measurements were recorded with excitation from an optical parametric oscillator pumped by the third harmonic of a Nd:YAG laser (Ekspla NT342B). The pulse width was ~4-5 ns, and the repetition rate was 10 Hz. The detection

portion of the spectrometer (Proteus) was manufactured by Ultrafast Systems. The instrument response function was ca. 4.8 ns.

Transient absorption data analysis was carried out using ASUFIT. In brief, decay-associated spectra were obtained by fitting the transient absorption kinetic traces over a selected wavelength region simultaneously as described by Equation 3 (parallel kinetic model),

$$\Delta A(\lambda,t) = \sum_{i=1}^{n} A_i(\lambda)\exp(-t/\tau_i) \quad (3)$$

where $\Delta A(\lambda,t)$ is the observed absorption change at a given wavelength at time delay t and n is the number of kinetic components used in the fitting. A plot of $A_i(\lambda)$ versus wavelength is called a decay-associated spectrum (DAS), and represents the amplitude spectrum of the i^{th} kinetic component, which has a lifetime of τ_i. The global analysis procedures described here have been extensively reviewed. Random errors associated with the reported lifetimes obtained from fluorescence and transient absorption measurements were typically ≤ 5%.

Structural characterization

^{1}H NMR spectra were recorded on a 400 MHz Varian Liquid-State spectrometer. NMR samples were dissolved in deuteriochloroform with 0.03% tetramethylsilane as an internal reference. Mass spectra were obtained on an Applied Biosystems Voyager-DE STR matrix-assisted laser desorption/ionization time-of-flight spectrometer (MALDI-TOF).

Dynamic light scattering (DLS)

Measurements were performed with a Malvern Instrument 4700 system with detection at 90° from the excitation, at a temperature of 25 °C, and using the 488 nm spectral line of an argon ion laser. Light scattering results were analyzed with Zetasizer software

(provided by the manufacturer) to obtain hydrodynamic radius distributions and polydispersity indexes. Micro emulsion solutions were filtered through 200 nm pore filters right before data acquisition. Extreme care was taken to reduce the contamination by dust.

Electrochemical Measurements

Cyclic voltammograms on 1, 2 and 3 in solution were carried out in benzonitrile (1) or acetonitrile (2, 3) with 100 mM tetrabutylammonium hexafluorophosphate as supporting electrolyte. A three electrode setup, consisting of a glassy carbon disc working electrode, platinum gauze counter electrode, and Ag^{+}/Ag quasireference, was used with the sample volume under an argon atmosphere. A CH Instruments 760D pontentiostat and corresponding software was used for all measurements. The Ag^{+}/Ag quasireference was calibrated to the ferrocenium/ferrocene (Fc^{+}/Fc) couple with $E_{Fc+/Fc}$ taken as 0.45 V vs. saturated calomel electrode (SCE).

Transmission Electron Microscopy

TEM micrographs were collected using a Philips CM200 TEM at 200kV. The TiO_2-micelle microemulsion was plated on a plasma treated (10 minutes, air intake) 200-mesh carbon coated copper grid (Canemco, Lakefield, QC, Canada) for 1 minute before wicking using filter paper. The grid was then rinsed with high purity water (HyClone, Logan, UT) to wash AOT surfactant away. TEM micrographs were analyzed using ImageJ software. [207] The 'analyze particle' plug-in was used to find the outline and calculate the diameter of nanoparticles on arbitrarily thresholded images.

Computational Methodology

Geometry optimizations of dyes 1, 2 and 3 (in their Open (O) and Closed (C) forms) (see Figure S3a in the Supporting Information) were performed with Gaussian 09 [208] using

Density Functional Theory (DFT) calculations at the B3LYP/6-31G(d) level of theory [209-216]. Using the Conductor-like Polarizable Continuum Model (CPCM), acetonitrile was implicitly included for all the optimizations. [217,218]

Results and Discussion:

Perylene dyes

Molecular structure

The structures of perylene derivatives 1, 2 and 3 are shown in Scheme 1. Based on the structure of the dyes, at least three species in equilibrium can be proposed during the hydrolysis of an anhydride group (catalyzed in basic media) as shown in Scheme 1 right. Partially hydrolyzed and/or deprotonated species, i.e. involving only one of the two anhydride rings present in the dyes, were not considered in this scheme but are also possible. As it is discussed below, the opening of at least one anhydride group to yield a dicarboxylic acid species is necessary for binding of the dyes to the TiO_2 surface. The precise nature of the interaction between the carboxylic group and the TiO_2 surface atoms still remains a subject of debate. Possible binding modes of the carboxylic acid species to the TiO_2 surface involve bidentate simple adsorption (electrostatic attraction and hydrogen bonding) and chemical bonding (ester linkage, bridging, and chelating) [199,219].

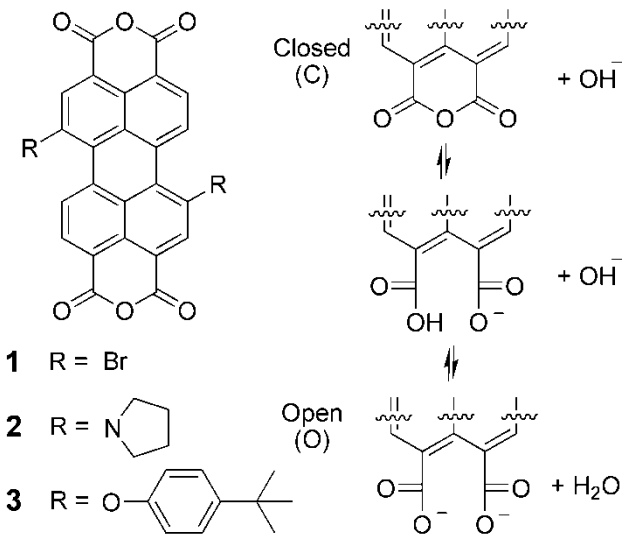

Scheme 1: Left: molecular structure of dyes 1, 2 and 3. Right: opening of anhydride ring under basic catalysis.

Spectroscopic characterization in homogeneous solution

Figure 1 shows the absorption and fluorescence of dyes 1 and 2 in ethanol (~10^{-6} M) as a function of time and addition of base (potassium hydroxide). The solutions were prepared by addition of a small aliquot (100 μL) of dye stock solution in THF (in this solvent the dyes are present in the anhydride form, species C Scheme 1) to 3 mL of ethanol with continuous stirring. The acquisition of spectra as a function of time started immediately after the stock dye solution was added to ethanol. For perylenes 1 and 3 both absorption and fluorescence spectra (Figure 1a and 1b) show clear isosbestic and isoemissive points indicating the interconversion between two species with distinct spectra and similar fluorescence quantum yields. The species that absorb and emit at longer wavelengths are assigned to the anhydride form (C, Scheme 1) while the shorter wavelength absorption and emission spectra are assigned to the fully hydrolyzed form for each dye (O, Scheme 1). [187,188,190-192] In the case of 2, isosbestic points and isoemissive points were not observed. This indicates that there is more than two interconverting species with significantly different spectra, presumably protonated/deprotonated amines, protonated/deprotonated carboxylic acids or zwitterionic species. For all perylenes the spectral changes observed indicate that the addition of a strong base (potassium hydroxide) is necessary to shift the equilibrium between the anhydride species (C, Scheme 1) and its hydrolyzed form (O, Scheme 1) towards the later. The base catalyzes the hydrolysis of the cyclic anhydride and deprotonates the resulting dicarboxylic acid (species O, Scheme 1). Figures 1a, 1c, and 1e show that the absorption spectra of the freshly prepared ethanol solutions (where the anhydride species prevails), are significantly bathochromically shifted (49 nm, 134 nm and 48 nm for 1, 2, and 3

respectively) compared to the corresponding spectra after base addition (when the fully hydrolyzed species prevails). The fluorescence spectra shown in Figures 1a and 1c were recorded with excitation at the isosbestic point for 1 and 3 (472 and 478 nm, respectively) to allow for the direct comparison of the relative fluorescence quantum yields of the anhydride and hydrolyzed species. The resulting fluorescence intensities indicate that the emission quantum yields (Φ_F) of both species (C and O) are very similar for these perylenes. For 2 the emission spectra were corrected for the number of photons absorbed at the excitation wavelength as described in the experimental section. Comparison of emission intensities before and after base addition for 2 (Figure 1d) indicates that the emission quantum yield of the hydrolyzed form is significantly larger than that of the di-anhydride form ($\Phi_F^O > 8\ \Phi_F^C$). The spectral changes observed upon hydrolysis of the dyes in solution are consistent with previous reports on analogous dyes [187,188,190,191,198] and were useful for monitoring the kinetics of dye binding to TiO_2 as described below.

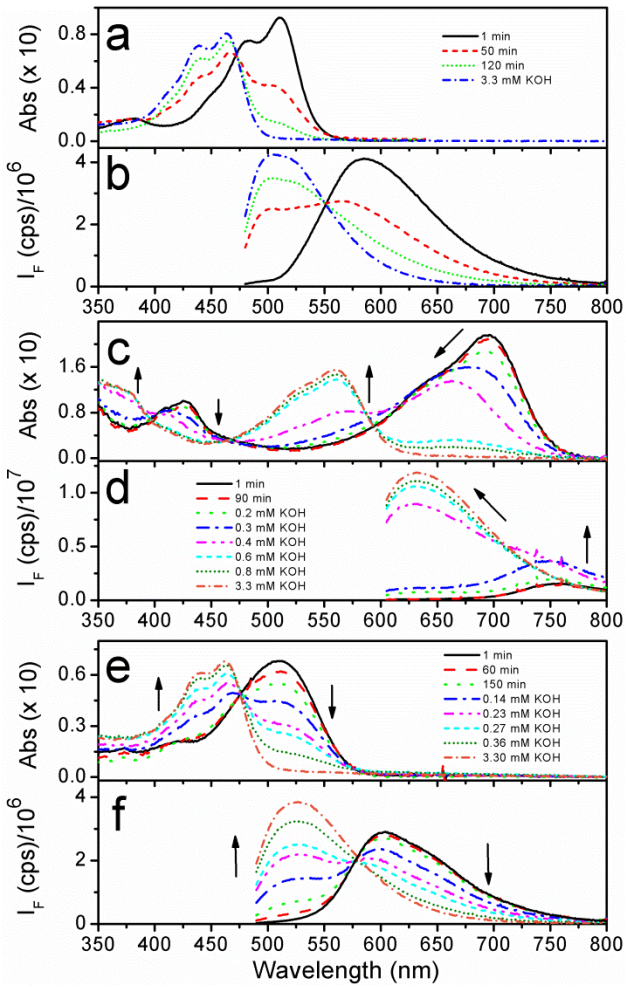

Figure 1: Absorption and emission spectra of 1 (a, b), 2 (c, d), and 3 (e, f) in ethanol as a function of time and KOH addition. Emission spectra for 1 and 3 were taken with excitation at the isosbestic point (472 and 475 nm, respectively). Emission spectra for 2 were taken with excitation at 594 nm. Dye concentration was ~ 10^{-6} M for all samples. Arrows indicate direction of change.

Energy diagram

Scheme 2 shows the relative energetics for the oxidation of the ground and excited states of the dyes and the conduction band edge (E_{CB}) of TiO_2. The potential for the first oxidation (D^+/D) of the dyes was measured electrochemically for the cyclic anhydride (closed) form of the dyes. Attempts to measure D^+/D of the hydrolyzed (open) form were unsuccessful thus to a first approximation the D^+/D of the C form will be used for calculations trough the text. The potential for the oxidation of the excited state (D^+/D^*) was calculated with the equation $D^+/D^* = D^+/D - E_{00}$, where E_{00} is the zero-zero optical excitation energy estimated from the intersection of the normalized absorption and emission spectra of the hydrolyzed (open) species in ethanol (see Figure S1 in the Supporting Information). The E_{CB} of TiO_2 was estimated as the flat-band potential [220] of polycrystalline TiO_2, –0.52 vs. SCE at pH = 2 [221] to account for the concentration of protons in the micelle water before NP formation. Based on energetic considerations, according to Scheme 2 all the dyes are capable to photoinject an electron in the conduction band of TiO_2. Two additional factors not considered in Scheme 2 could in principle lead to a higher driving force for the photoinduced IET process: a) the oxidation potentials of similar dyes attached to the TiO_2 surface in their open bound form are known to shift anodically relative to those in solution in their closed form [188,190,192] and b) the presence of trap-sites energetically situated between the valence and conduction bands of the TiO_2 NPs which could act as electron acceptors. Finally the size-quantization effect observed in the TiO_2 NPs used herein (vide infra) could lead to a negative shift of E_{CB} shown in Scheme 2 resulting in a decreased driving force for photoinduced electron transfer. Since the magnitude of the factors mentioned before

cannot be estimated accurately Scheme 2 provides only a first approximation for the energetics of the system. Quantum mechanical calculations were performed to correlate molecular structure with the experimental electrochemical and spectroscopic parameters. The calculated HOMO-LUMO energies and energy gaps are summarized in Table 1. Rationalizing the DFT calculations by means of molecular orbital analysis, it was observed that both the HOMO and LUMO energies of all dyes shifted to less negative energies (vs. vacuum) upon opening of the anhydride ring. Also the HOMO-LUMO gap of all dyes increased upon opening of the anhydride with respect to the closed form, resulting in a hypsochromic shift of the absorption spectra. These two observations combined yield an increase in the driving force for photo-induced injection. These results are in agreement with previous work on analogous perylenes [186,187,191,192] and correlate well with the electrochemical and spectroscopic data presented in Table 1 and Figure 1.

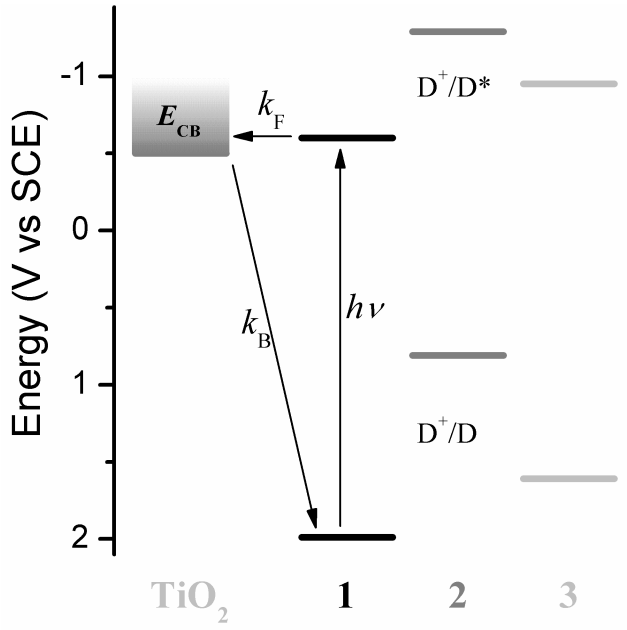

Scheme 2: Diagram depicting the potentials for the first oxidation and for the oxidation of the optically excided states of 1, 2, and 3 and the TiO_2 Conduction Band (CB) energy. D/D^+ values were measured electrochemically for the anhydride (closed) form of the dye. D/D* values were calculated as described in the text from the E_{00} energy of the hydrolyzed (open) form of the dyes.

Table 1. Energetics of 1, 2, and 3 estimated by electrochemistry, spectroscopy and quantum mechanical calculations.

	Ox(1)[a]	Ox(2)[a]	Red(1)[a]	Red(2)[a]	HOMO[c]	LUMO[c]	HOMO-LUMO Gap[c]	E_{00} [b]
1-C	1.99 (irr)	--	-0.25 (61)	-0.52 (64)	1.99	-0.52	2.51	2.32
1-O	--	--	--	--	1.83	-0.82	2.65	2.59
2-C	0.81 (47)	0.91 (35)	-0.72 (61)	--	0.86	-1.08	1.94	1.71
2-O	--	--	--	--	0.73	-1.40	2.13	2.10
3-C	1.61 (65)	-- --	-0.51 (52)	-0.70 (55)	1.56	-0.80	2.36	2.22
3-O	--	--	--	--	1.41	-1.10	2.51	2.56

[a] $E_{1/2}$ values for the indicated process reported in V vs. SCE with the peak separation (ΔE_p) given in mV.

[b] Determined from the intersection of the normalized emission and absorption spectra (measured in ethanol, Figure 1S in SI) with the equation E_{00} (eV) = 1240/λ (nm).

[c] Calculated HOMO and LUMO energies (see Figure S3a in Supporting Information) were normalized to the experimental oxidation potential of 1-C vs. SCE by the equation: $E_{vs.\ SCE} = -E_{cal} - 4.26$ eV.

Titanium dioxide nanoparticles (TiO_2 NPs)

Characterization

The hydrodynamic diameter distribution of the micellar suspension before and after the addition of TTIP stock was measured by DLS. As shown in Figure 2a (grey bars), the mean hydrodynamic diameter (d) of the micelles before TTIP addition was found to be d =3.8 ± 0.5 nm (mean and standard deviation of three independent experiments). After formation of TiO_2 NPs the mean hydrodynamic diameter of the micelles/TiO_2 microemulsion is slightly increased to d = 4.5 ± 0.1 nm, see Figure 2a (black bars). As seen in this figure the size distribution of the micelle microemulsion with TiO_2 NPs is narrower than that of the micelles without TiO_2 NPs. This effect can be attributed to the fact that micelles without TiO_2 inside are inherently dynamic systems continually exchanging water from the inner pool and surfactant molecules with other micelles, so that its size varies constantly. In the case of micelles containing TiO_2 NPs the surfactant movement is much more restricted, possibly due to attractive electrostatic interactions between the negatively charged polar head of the surfactant and the positively charged oxide surface under the acidic conditions inside the water pool. Estimation of the total concentration of micelles ($C_m = 10^{-3}$ M) and of TiO_2 NPs ($C_{NP} = 10^{-3}$ M) (see details in the Supporting Information) in the resulting solution after NP formation indicates that a large fraction of the total micelles do not contain TiO_2 NPs. Considering this estimation we rationalize the significant difference observed for the DLS results of micelles with and without TiO_2 NPs as consequence of a higher light scattering efficiency of the TiO_2 NP vs. that of "empty" micelles.

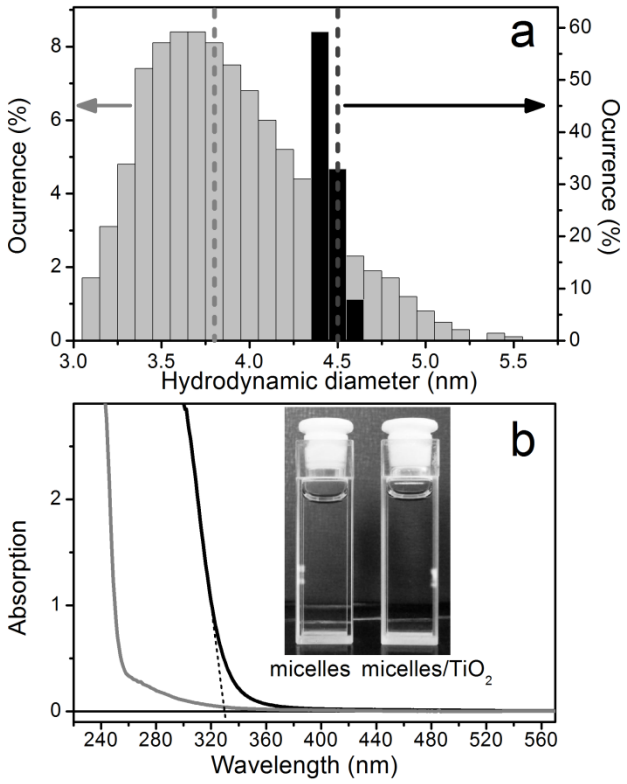

Figure 2: a) DLS measurements of microemulsions without (grey bars) and with (black bars) TiO_2 NPs. Dashed lines indicate the corresponding mean diameter values for each sample. b) Absorption spectra of microemulsions without (grey) and with (black) TiO_2 NPs. Insert shows a photograph of the micelle and micelle-TiO_2 microemulsions.

Spectroscopic evidence for the formation of TiO_2 particles is seen in the absorption spectra. Figure 2b shows the absorption spectra of micelles before (dashed line) and after the addition of TTIP (solid line). In the latter, the strong absorption in the UV region is assigned to the TiO_2 band gap transition. It is well-known that the band-gap of semiconductors is modulated by quantum confinement effects when the particle size reaches nanometric dimensions. [222,223] These sized-induced quantum effects produce an increase of the band-gap which results in a blue-shift of the optical absorption. However, some reports in the literature indicate unusual variation of the oscillator strength of the first allowed direct transition in TiO_2 NPs (as consequence of structural size effects) and caution about the use of the absorption shifts to estimate NP size based on quantization effects. [224] Other reports indicate that the presence of surface states and formation of a surface dipole layer on the surface of TiO_2 NPs synthesized in inverse micelles leads to sub-band gap absorption making the comparison of shifts unreliable. [225] Our TiO_2 NPs show a significant blue shift in the absorption spectra relative to that of bulk TiO_2. Assuming that this shift is due to quantum effects, the apparent band-gap of the NPs can be estimated as $E_{BG} \sim 3.88$ eV (see Figure S2 in the Supporting Information). This putative E_{BG} of TiO_2 NPs is significantly higher than that of bulk TiO_2 (3.2 and 3.0 eV, for anatase and rutile phases respectively) suggesting significant size-quantization. [175,225-227] The prepared micelle/TiO_2 microemulsion has very low light scattering effects even at wavelengths below 350 nm due to the small average size of the TiO_2 NP and narrow size distribution, being an ideal system for spectroscopic studies.

The morphology and crystallinity of the synthesized TiO_2 NPs were studied by transmission electron microscopy (TEM). The micrographs in Figure 3 show nearly

spherical particles with an estimated mean diameter of 3.5 ± 0.7 nm (average from 123 particles). The particles have a relatively narrow size distribution as shown on the histogram in Figure 3c. These measurements are consistent with the DLS results showing a mean diameter for the "naked" TiO_2 NPs which is slightly smaller than the mean hydrodynamic diameter of the TiO_2-micelle system. High resolution TEM (HRTEM) images (Figure 3a) show, for some particles, clear crystal planes with an average spacing of 2.186 ± 0.004 Å (mean from 6 NPs), which matches well the literature values of the (111) planes of bulk rutile TiO_2 (2.188 Å, (111) plane); no interplanar spacing in the anatase phase matches this value. Even though this information is not sufficient to categorically assign a crystal structure to the synthesized nanoparticles, since this would require a more detailed study involving diffraction experiments, the results suggest the rutile phase as the most likely one. However, given the large number of factors that affect the observation of NPs crystalline structure in TEM micrographs [228] we cannot make a definitive assignment of the crystalline nature of the prepared TiO_2 nanoparticles based only on HRTEM images.

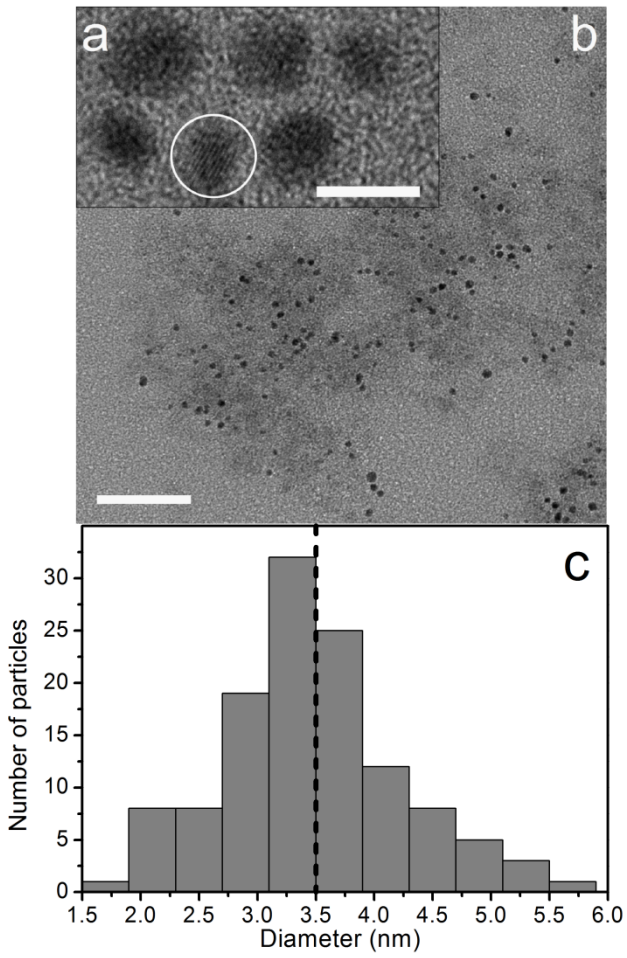

Figure 3: TEM micrographs of TiO_2 nanoparticles synthesized in AOT reverse micelles. a) High magnification image showing crystallinity in the circled TiO_2 nanoparticle. Scale bar = 5 nm. b) Representative region showing TiO_2 nanoparticles as dark circles and excess AOT surfactant as dark gray areas. Scale bar = 50 nm. c) Histogram of nanoparticles diameter constructed by analyzing TEM micrographs, see details in text. The dashed line indicates the mean diameter value.

Dyes - TiO_2 NPs systems

Assembly

Binding of perylene 1 and 2 to TiO_2 NPs in a microemulsion was carried out by addition of 100 μL of a stock solution of the dye (~10^{-4} M) in THF to 3 mL of a TiO_2-NP-micelle suspension ([TiO_2] = 0.109 g/L) in n-heptane (for pump-probe experiments the dye/TiO_2 NP concentration ratio was increased two times). The microemulsion was left incubating for > 4 h and absorption spectra were recorded at periodic time intervals immediately after addition of the dye as shown in Figure 4. A control sample of micelles without TiO_2 was prepared as described in the materials section and analyzed in analogous manner. The hypsochromic shift observed in the absorption spectra of dyes 1 and 2 in the presence of TiO_2 is indicative of opening of the anhydride ring and suggest binding of the resulting dicarboxylic form of the dye to the semiconductor. [186-192,197,198] Further evidence for dye binding to the oxide surface comes from time resolved experiments that are described in detail below and which show the formation of the $dye^{\bullet+}$-$TiO_2(e–)$ charge separated state. Other authors have confirmed binding of dyes (containing carboxylic acid moieties) to TiO_2 films using FTIR by monitoring the frequency shift of the carbonyl band upon acid deprotonation and binding to the oxide surface. [229,230]. In the micelle systems described herein, AOT surfactant molecules are in a ~10^5 fold excess relative to dye molecules (vide infra) thus the IR absorption of the AOT ester groups dominates the carbonyl band signal and precludes observation of dye binding to TiO_2 by vibrational spectroscopy. In both systems, 1-TiO_2 and 2-TiO_2, the binding of the dye was a relatively slow process as shown by the kinetic traces in Figure 4a,b inserts. When 3 was added to a TiO_2 NPs microemulsion no significant changes

were observed in the absorption and emission spectra over time indicating that the dye's anhydride groups are not hydrolyzed. Under these conditions the attachment of the dye to the TiO_2 surface through the possible binding modes of the carboxylic acid species is precluded.

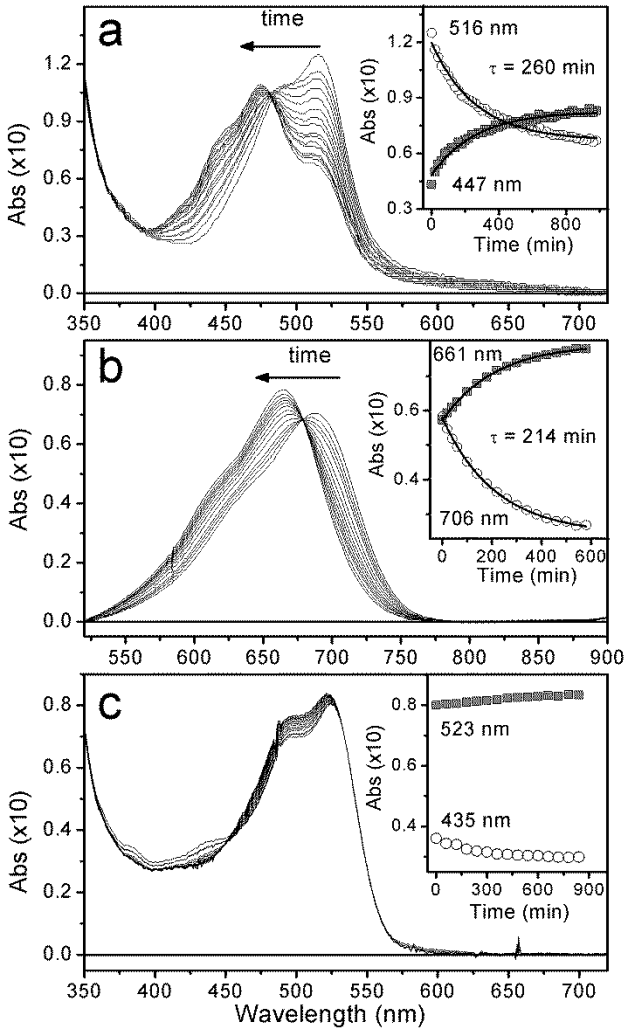

Figure 4: Absorption spectra of 1 (a), 2 (b) and 3 (c) in a microemulsion containing TiO_2 NPs as a function of time. Insert displays kinetic traces at the indicated wavelengths (circles and squares) and corresponding monoexponential fittings (solid lines) with a shared time constant.

Figure 5 shows the absorption, fluorescence emission, and excitation spectra of the dyes in samples described above after incubation for 17 hours. No further spectral changes were observed beyond this time. The absorption spectrum of 1 in the presence of TiO_2 NPs (Figure 5a, solid line) shows clear contributions from two distinct species, referred as 1-C and 1-OB (for Closed-unbound and Open-Bound to TiO_2, respectively), with absorption peaks (Abs_{max}) at ~519 nm and 471 nm respectively. The presence of the TiO_2 NPs is confirmed by the strong absorption in the UV region (below 360 nm), see Figure 5a, solid and dotted lines. The corresponding fluorescence excitation spectrum (Figure 5a, dashed line) indicates that 1-C is the species that contributes predominantly to the observed fluorescence. The absorption and fluorescence excitation spectra of the control sample without TiO_2 NPs (Figure 5b), show that 1-C is the only species present in the absence of TiO_2 NPs. Note that in this case the strong TiO_2 absorption in the UV region is not observed.

Analogous preparation and analysis using perylene 2 shows similar results (Figures 5c and 5d). In this case the observed shift (~ 25 nm) is significantly smaller than that observed in ethanol upon full basic hydrolysis (~134 nm), this difference could be explained considering only partial hydrolysis of the dye in the TiO_2-micelle microemulsion. Thus, the spectra with peak absorption at ~690 nm and 665 nm are assigned to the anhydride (Closed, 2-C) and partially hydrolyzed (Open Bound, 2-OB, i.e. only one anhydride group is hydrolyzed) forms of 2, respectively. Evidence for the putative partial hydrolysis of 2 in ethanol is shown as a small shift in the absorption and emission spectra upon addition of a few equivalents of KOH, see Figure 1c blue dash dot

line. As mentioned before, the lack of an isosbestic point in Figure 1c suggests the presence of more than two interconverting species for 2.

The absorption and emission spectra of 3 did not show significant changes in TiO_2-micelle vs. empty micelle microemulsions as shown in Figure 5e and 5f. The lack of spectral shift and low emission quenching suggest that the dye does not open and bind to the oxide and consequently cannot effectively photoinject an electron in its conduction band. The deficient binding of the dye is rationalized as a consequence of the bulky 4-tert-butylphenyloxy groups which create a strong steric hindrance for the insertion of the dye through the micelle structure to reach the TiO_2 NP surface. Analysis of the calculated molecular structure for the dyes support this interpretation indicating that the largest molecular dimension (D) across the perylenes' bay substituents varies in the series as D1 (9 Å) < D2 (13 Å) < D3 (27 Å), see Figure S3b in the Supporting Information.

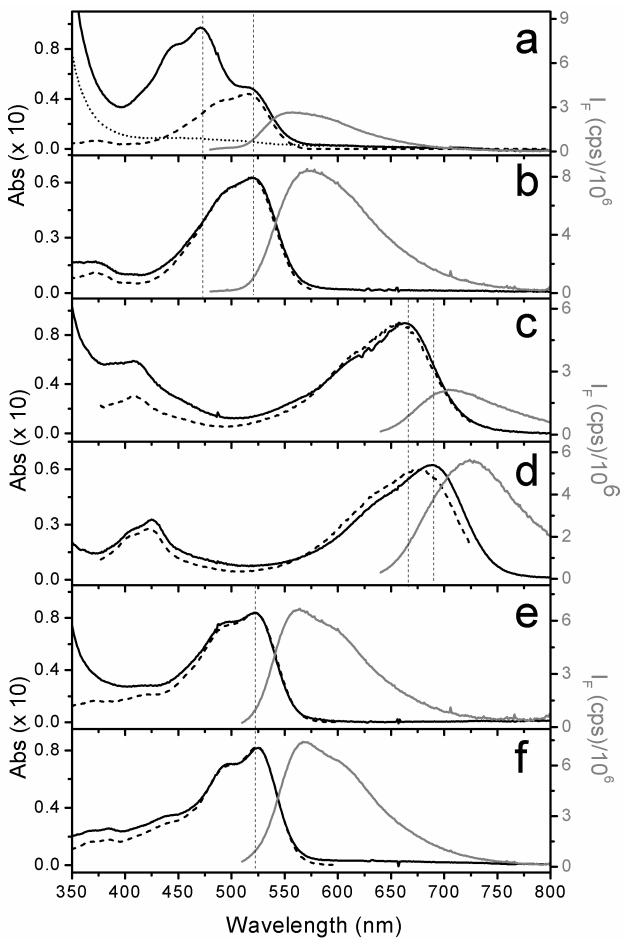

Figure 5: a) Absorption (solid black), emission (solid grey), and normalized excitation spectra (dash) of perylene 1 in a microemulsion containing TiO_2 NPs and absorption of a microemulsion containing TiO_2 NPs (dotted line) but not the dye. b) Same as (a) for a microemulsion without TiO_2. c, d) Same as (a) and (b) respectively for perylene 2. e, f) Same as (a) and (b) for perylene 3. Excitation spectra were recorded with emission at 578 nm, 735 nm, and 610 nm for (a, b), (c, d), and (e, f), respectively. Emission spectra were recorded with excitation at 470, 630 nm, and 495 nm for (a, b), (c, d), and (e, f), respectively. Emission spectra intensities were corrected as described in the experimental section. Vertical dotted lines show absorption maximum in microemulsions with and without TiO_2 NPs for each dye.

Steady state absorption and emission spectra and emission anisotropy

Steady state fluorescence anisotropy measurements were performed to gain insight on the location of the dyes in micellar suspensions. Table 2 shows that the fluorescence anisotropy of 1, 2, and 3 is considerably higher in micellar suspensions than in the low viscosity solvent THF indicating that the movement of the dye is significantly restricted and suggesting that it is preferentially located in the ordered micellar environment. This preferential location of the dye generates a relatively high local concentration of the dye in the micellar environment, which presumably facilitates the binding of dye to the adjacent oxide surface in solutions of micelles with TiO_2 NPs. Under these conditions, the fluorescence of 1 and 2 in the TiO_2-micelle suspension is highly reduced (~70% quenched for 1-TiO_2 and 2-TiO_2 compared to the corresponding control samples without TiO_2). In the case of the 1-TiO_2 system, the emission is dominated by the spectrum of the closed anhydride species of the dye (Scheme 1, C) while the absorption spectra has a major contribution corresponding to the open bound species (OB). The lack of significant emission corresponding to the OB species suggests an efficient fluorescence deactivation pathway by electron injection from photoexcited dye into the TiO_2 conduction band (see Scheme 2). The remaining emission of the 1-TiO_2 system, which is presumably from the non-bound C species located in the micellar environment, is more polarized than that of 1 in the micelle without TiO_2. This indicates that the TiO_2 NP restricts the movement of the non-bound dye presumably by creating a more rigid micelle due to the strong electrostatic interaction of the positively charged TiO_2 surface and the negatively charged phosphonate group of the surfactant. Similar observations were found for the 2-TiO_2 system although it is difficult to discriminate the

contribution of the C species and partially OB species due to the relatively small spectral shift in their emission spectra. The shape of the fluorescence excitation spectra of the 2-TiO_2 system is in between the absorption spectra of the 2-TiO_2 and 2-micelle systems indicating a significant contribution of both the C and the OB species to the observed fluorescence. In the case of the 3-TiO_2 system the emission spectra is dominated by the emission of the C species and the steady state emission anisotropy measurements in different environments show similar trends to the other perylene systems, but not so marked. This observation is consistent with the dye being located in the outer layer of the micellar structure but not close enough to attach to the TiO_2 surface.

Table 2. Steady state fluorescence anisotropy (r) of perylene dyes in different environments. [a]

	THF	micelle	micelle/TiO_2
1	0.004 (0.002)	0.12 (0.01)	0.24 (0.01)
2	0.011 (0.001)	0.15 (0.02)	0.33 (0.03)
3	0.015 (0.007)	0.04 (0.01)	0.21 (0.01)

[a] Anisotropy was measured in a L-format geometry spectrofluorimeter. The reported numbers are the average and the standard deviation (in parenthesis) of the values obtained over the 520-610 nm, 710-770 nm, and 550-640 nm spectral range for 1, 2, and 3 respectively.

Time resolved fluorescence anisotropy

Figure 6 shows the fluorescence anisotropy decays of dyes 1, 2 and 3 in different environments. The fluorescence anisotropy decay of 1 in heptane can be fitted with one fast decay lifetime of 81 ps. However when 1 is dissolved in a micelle solution (control sample) the anisotropy shows a bi-exponential decay with components of 81 ps (2%) and 1.67 ns (98%). The 81 ps component is associated to the rotational correlation time of 1 in the heptane whereas the 1.67 ns component could be associated to the rotation of the dye within the surfactant layer of the micelle. Alternatively the 1.67 ns component can be associated to the rotation of the whole dye-micelle assembly (the decay closely matches the rotational correlation time of a sphere with diameter of ~ 3.5 nm in hexane). [206] The anisotropy decay of 1 in a micelle solution containing TiO_2 NPs shows a bi-exponential decay with a 81 ps (15%) component associated with the free dye in heptane and a longer 2.74 ns (85%) component associated with the rotation of the dye in the restricted surfactant layer or with the rotation of the whole 1-TiO_2/micelle assembly in hexane. Dye 2 shows analogous behavior with slightly larger decay components in all media, this difference is associated with the larger molecular dimension D (see Figure S3b) of 2 vs. 1 which hinders the rotation of 2 relative to that of 1.

Dye 3 dissolved in heptane and micelles shows analogous behavior to 1 and 2 but with slightly larger decay components consistent with a larger steric hindrance for rotation due to the bulky t-butylphenoxy groups. The anisotropy decay of 3 in micelles with TiO_2 NPs is very similar to that in micelles without NPs. This observation is consistent with the lack of spectroscopic evidence for opening of the anhydride groups and putative binding to the TiO_2 surface. Overall the analysis of the time resolved data show results in line with those of the steady state anisotropy emission shown in Table 2.

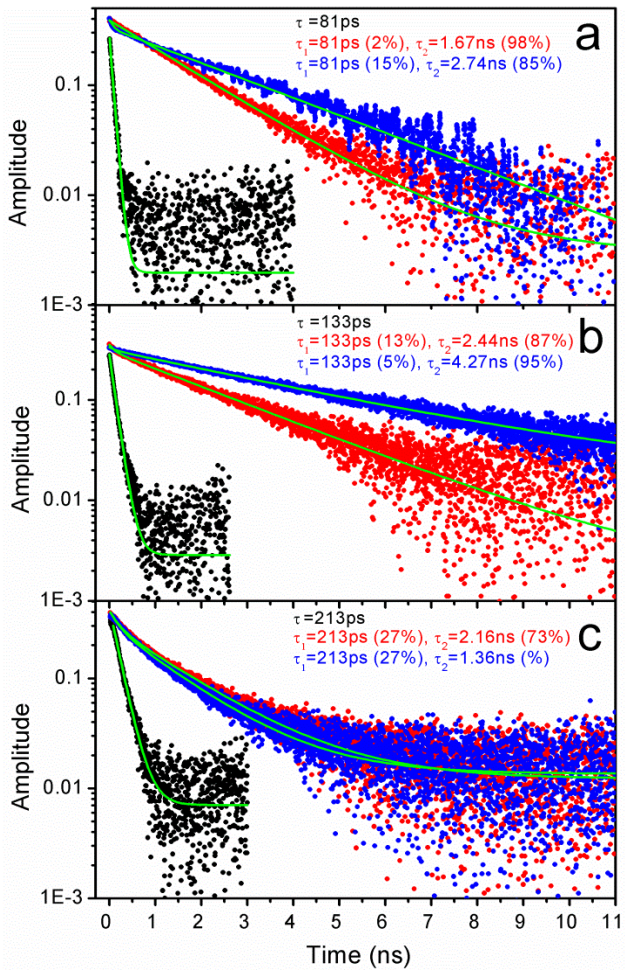

Figure 6: a) Fluorescence anisotropy decays (data points) of 1 in heptane (black), micelle solution (red), and TiO_2-micelle solution (blue). Smooth lines show exponential fits to the data. Samples were excited and emission collected at the following wavelengths, heptane and micelle: λ_{ex}= 520 nm λ_{em}= 600 nm and 1-TiO_2 λ_{ex}= 420 nm, λ_{em}= 510 nm. b) Same as (a) for dye 2. Heptane: λ_{ex}= 640 nm λ_{em}= 750 nm, micelle: λ_{ex}= 640 nm, λ_{em}= 750 nm, and 2-TiO_2 λ_{ex}= 640 nm, λ_{em}= 750 nm. c) Same as (a) for dye 3. Heptane, micelle and 3-TiO_2: λ_{ex}= 515 nm and λ_{em}= 600 nm. Dye concentration was ~ 10^{-6} M for all samples.

Time resolved emission

TC-SPC measurements were performed to investigate the nature of the steady state emission quenching observed for the dye-TiO_2 systems. Figure 7a shows the fluorescence Decay Associated Spectra (DAS) of the 1-TiO_2 system. Global analysis of kinetics yields four decay components ($\chi^2 = 1.14$) with lifetimes of 29 ps, 212 ps, 1.09 ns, and 4.28 ns. To a first approximation the 29 ps component with maximum at 520 nm is associated with the 1-OB (Open Bound species) and the rest of the components are associated with the 1-C (Closed unbound species) in different environments. Based on these assignments the first fluorescence DAS (29 ps) shows energy transfer from 1-OB (Open Bound species) to 1-C as indicated by the negative amplitude above 600 nm. The second (212 ps) and third (1.09 ns) components show energy migration in between 1-C species which are in slightly different environments towards the most solvated one, with the lowest energy (4.28 ns component). Overall, the data indicates the existence of a non-homogeneous system with several dyes per micelle. Analogous measurements on the 1-micelle system (control sample without TiO_2 NPs), show longer lived multiexponential decays (see Figure S4a in the Supporting Information) consistent with the high emission quenching observed for 1-TiO_2 vs. 1-micelle in the steady state measurements (vide supra).

Figure 7b shows the fluorescence Decay Associated Spectra (DAS) of the 2-TiO_2 system. Global analysis yields four decay components ($\chi^2 = 1.09$) with lifetimes of 487 ps, 2.8 ns, and 5.3 ns. The 487 ps component is associated with the 2-OB (partially Open Bound species) and could be assigned in principle to the photoinduced electron injection

process from 2-OB to TiO_2. However some electron injection may occur faster than the instrument resolution (~10 ps) and therefore is non-time-resolved in this experiment. The rest of the components are associated with the 2-C (Closed non-bound species) in different environments. Analogous measurements on the 2-micelle system (control sample without TiO_2 NPs), show a longer lived biexponential decay (2.9 ns and 4.9 ns, see Figure S4b in the Supporting Information) consistent with the high emission quenching observed for 2-TiO_2 vs. 2-micelle in the steady state measurements (vide supra).

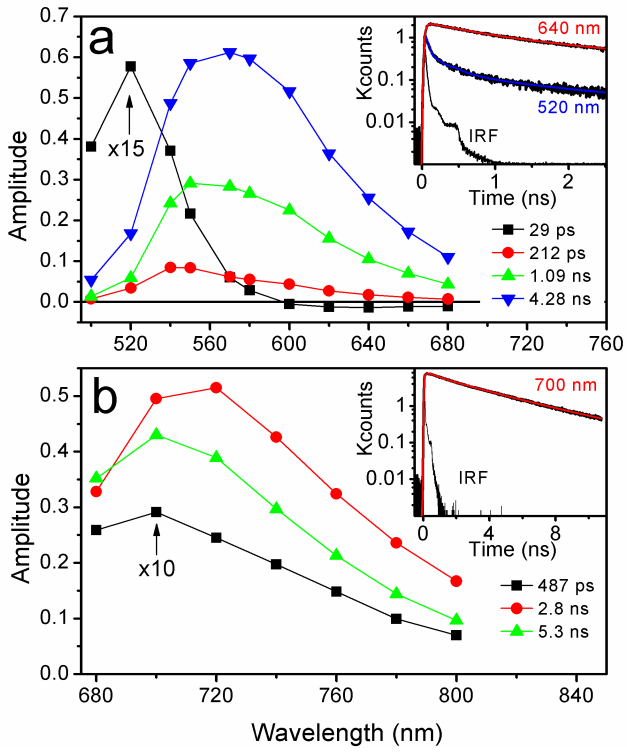

Figure 7: a) Fluorescence decay associated spectra of the 1-TiO_2 system, data was acquired with excitation at 480 nm. Data was globally fitted (χ^2= 1.14) as described in the experimental section. Insert: kinetic traces and corresponding fits (smooth line) at selected wavelengths and the Instrument Response Function (IRF). b) same as (a) for the 2-TiO_2 system (χ^2= 1.10). Data was acquired with excitation at 640 nm. The short lived components were multiplied by a factor to make them clearly visible.

Time resolved absorption

Femtosecond pump-probe experiments were performed to establish the kinetics of the photoinduced electron transfer reaction of the dye-TiO_2 system. Figure 8a shows the results for the 1-TiO_2 system, global analysis of kinetics (measured up to 40 ps time delay) shows four decay components with lifetimes of 210 fs, 2.5 ps, 21.5 ps, and 212 ps. The 40 ps time window used in the experiment was chosen to accurately determine the faster components of the decay; the 212 ps component cannot be accurately determined with this window and was fixed in the analysis based on the information provided by the TC-SPC experiments (vide supra). The Decay Associated Spectra (DAS) of the 210 fs component can be attributed to the formation of charge transfer state between 1-OB and TiO_2 (i.e. $1^{\bullet+}$-TiO_2(e–)). It shows decay of stimulated emission and singlet excited state absorption at ~540 and 780 nm, respectively, and formation (negative amplitude) of 1-OB radical cation with characteristic absorption at ~650 nm. [196,231] The DAS of the 2.5 ps component can be attributed to the decay of 1-C showing ground state bleaching and stimulated emission at ~500-700 nm and singlet excited state absorption at ~780 nm. This DAS can be associated with the process seen in the fluorescence decays, i.e. energy migration in between 1-C species in different environments. The 21.5 ps component is most likely due to the energy transfer process between 1-OB and 1-C as seen in the fluorescence decay data (Figure 7a 29 ps fluorescence DAS).

The DAS of the 212 ps component shows a mixture of two main processes: a) decay of singlet excited state of the 1-C species (as seen in the fluorescence decay data) and b) decay of the $1^{\bullet+}$-TiO_2(e–) charged separated state with strong absorption at ~650 nm and weak absorption around 850-1000 nm characteristic of the 1-OB [196,231] radical cation species and free carrier (injected electrons) in the TiO_2 semiconductor, [232] respectively.

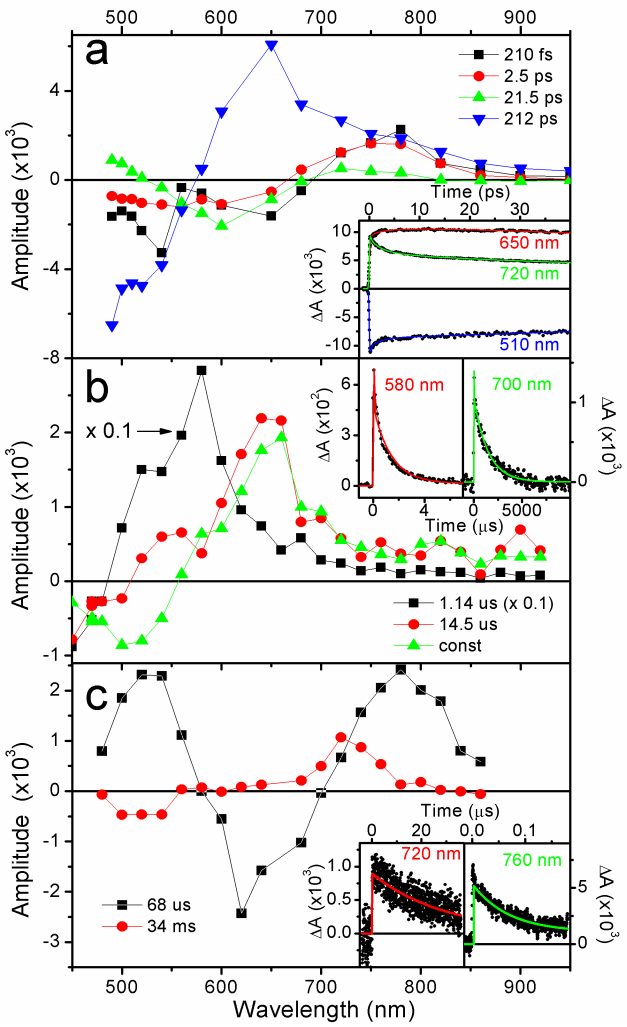

Figure 8: a) Decay associated spectra of the 1-TiO_2 system measured by pump-probe (fs-ps range). Data was acquired with laser excitation at 460 nm. Insert: kinetic traces (data points) and corresponding fits (smooth lines) at selected wavelengths. b) Same as (a) measured by flash photolysis (ns-μs range). Data was acquired with laser excitation at 440 nm. c) Decay associated spectra of the 2-TiO_2 system in argon saturated solution measured by flash photolysis (ns-μs range). Data was acquired with laser excitation at 660 nm.

Transient absorption measurements on the 1-TiO_2 system in the nanosecond to millisecond time range were performed to complement the pump-probe data on the faster time scale, the results are shown in Figure 8b. Global analysis of the kinetics shows three decay components: 1.14 ms, 14.5 ms, and a component that does not decay within the 40 ms time window. The 1.14 ms DAS is associated with the decay of triplet excited states of 1-C and 1-OB showing transient absorption in the ~500-650 nm range and ground state bleaching at 450 and 510 nm. The other two DAS are associated with the decay of the $1^{\bullet+}$-TiO_2(e–) state. They show the characteristic ground state bleaching and induced absorption seen in the pump-probe data (see Figure 8a, 212 ps DAS). The non-decaying transient has ground state bleaching at ~510 nm and is associated with charge transfer state formed with 1-C most likely due to migration of charge from 1-OB to 1-C. The triplet excited state is not clearly shown in these measurements since it is most likely quenched due to presence of molecular oxygen. To determine the lifetime of the non-resolved component, a kinetic trace at 700 nm was recorded up to 10 ms, see Figure 8b insert. Fitting of this trace yields two decay components of ~15 μs and ~1.5 ms. As mentioned before both of these components are consistent with the decay of $1^{\bullet+}$ species.

Flash photolysis measurements on the 2-TiO_2 system in argon saturated solution are shown in Figure 8c. Global fit to the data yields two components: a long lived component of 34 ms assigned to the decay of the $2^{\bullet+}$-TiO_2(e–) charge transfer state and a 68 μs DAS assigned to 2-OB and 2-C triplet states. Measurements in air saturated solutions (See Figure S5 in the Supplementary Information) show only one DAS of 30 ms assigned to the $2^{\bullet+}$-TiO_2(e–) state with spectral features very similar to the long decay measured in argon. The transients in the 520-700 nm and 640-820 nm regions correspond

to the 2-OB ground state absorption recovery and the 2-OB radical cation absorption decay respectively.

Attempts to determine the formation rate of $2^{\bullet+}$-TiO_2(e–) at short time scales using the pump-probe technique showed only features associated to the excited state decay (see Figure S6). The lack of radical cation absorption at early times is probably due to the long lifetime of the $2^{\bullet+}$-TiO_2(e–) state which precludes the recovery of the 2-TiO_2 system ground state in the time between laser pulses (2 ms, pulse frequency = 500 Mz) coupled to slow sample mixing due to the high viscosity of the solutions.

Rigorous analysis of time resolved emission and absorption data in a non-homogeneous system requires the use of a model which considers a distribution of exponential decays to describe the kinetics of each transient species. The distribution of decays accounts for the distribution of available environments in the heterogeneous system. In our analysis we used the minimum number of exponential components that adequately fitted the experimental data within the experimental error. Thus it is likely that the reported decay components correspond to a weighted mean value of the actual distribution of constants associated with each species.

Distribution of dyes in the micellear solution

To better understand the dye-TiO_2 assembly process it is useful to discuss the expected distribution of dyes in micellar systems. The distribution of non-reacting dyes (i.e. in anhydride form) in a micelle microemulsion can be calculated from the concentration of dye and micelles (C_{dye} and C_m, respectively) assuming Poisson statistics [111 233] as shown in Equation 4:

(4) $$P_n = \frac{\lambda^n \cdot e^{-\lambda}}{n!}$$

where P_n is the probability of finding n dyes in a given micelle and $\lambda_m = C_{dye}/C_m$ is the average number of dyes per micelle. In our experiments $\lambda_m > 10^{-3}$ (see Supporting Information) thus the probability of finding two (or more) dyes in a given micelle is less than one in a million. On the other hand, considering that $\lambda_{NP} = C_{dye}/C_{NP} \sim 0.77$ (see Supporting Information) and assuming that the dyes are distributed exclusively among micelles that contain TiO_2 NPs the probability of finding two and three dyes per NP are $P_2 \sim 0.14$ and $P_3 \sim 0.03$ respectively. Comparison of $C_m \sim 10^{-3}$ M and $C_{NP} \sim 1.3\times10^{-6}$ indicates that in the TiO_2-NP micro-heterogeneous solutions a large fraction of the total micelles do not contain TiO_2 NPs. The results of these calculations and the evidence for dye aggregation shown in the time resolved experiments (vide supra) suggest that in the equilibrated 1-TiO_2 and 2-TiO_2 systems the dyes are preferentially located in the small fraction of the micelles that contain TiO_2 NPs rather than being statistically distributed among all the available micelles. This preferential dye location can be explained considering the following mechanism. At early times after dye addition, the dyes are statistically distributed among all the available micelles in the solution by micelle-collision mediated dye exchange. When a dye reaches a micelle containing a TiO_2 NP it can attach to the oxide surface and it is longer available to be exchanged with other micelles on subsequent collisions. Eventually all non-bound dyes "find" micelles containing a TiO_2 NP and attach to them. The slow equilibration process shown in Figure 4a,b could in principle be evidence of the proposed mechanism.

Photoiduced electron transfer

The spectroscopic results discussed above show evidence that both the 1-TiO_2 and 2-TiO_2 systems undergo photoinduced electron transfer to yield the dye-TiO_2 charge separated state. Global analysis of pump-probe and flash photolysis results indicate that the apparent forward and backward rate constants for the formation and decay of the $1^{\bullet+}$-TiO_2(e–) state are $k_F \sim 4.8\times10^{12}$ s^{-1} (1/210 fs) and $k_B < 6.9\times10^{4}$ s^{-1} (1/14.5μs), respectively. On the other hand, as it was mentioned above, it was not possible to measure by pump-probe the k_F of the $2^{\bullet+}$-TiO_2(e–). TC-SPC results for this system show a fluorescence decay with relatively slow components, the shortest decay component of ~490 ps for 2^{*}-TiO_2 might in principle be associated to the formation of the $2^{\bullet+}$-TiO_2(e–) however due to the limited time resolution of the TC-SPC experiment there is most likely a much faster unresolved fluorescence decay component associated with photoinduced electron injection on a shorter time scale (< 10ps). Formation of $2^{\bullet+}$-TiO_2(e–) was confirmed by flash photolysis experiments showing clear features of charged separated state that decayed on a very long time scale, $k_b = 33$ s^{-1} (1/30ms). For the 3-TiO_2 system the spectroscopic studies indicate that the dye does not bind to the TiO_2 NPs and show no evidence of photoinduced electron injection. Thus in the following analysis only the 1-TiO_2 and 2-TiO_2 systems will be considered.

The experimentally determined electron transfer rate constants can be discussed in terms of Equation 5 and similar equations that have been developed to describe electron transfer from a single donating state to a continuum of accepting states, such as those present in the conduction band of TiO_2 nanoparticles, [145,220,234-237]

$$k_{F(eT)} = \frac{2\pi}{\hbar}\int_{-\infty}^{\infty}\rho(E)\left|\overline{H}(E)\right|^2\left(4\pi\lambda k_B T\right)^{-1/2} e^{-\frac{(\lambda+\Delta G^0+E)^2}{4\lambda k_B T}} \quad (5)$$

where ρ (E) is the effective density of states at the energy E relative to the conduction band edge, $\overline{H}(E)$ is the average electronic coupling between the dye excited state and all k states in the semiconductor, and λ is the total reorganization energy. ΔG^0 is the energy difference between the energy level of the excited dye and the bottom of the conduction band and can be written as $\Delta G^0 = E_{CB} - E(D^+/D^*)$. To a first approximation $\overline{H}(E)$ and λ are assumed to be the same for all the dye-TiO_2 systems given the analogous structure of the dyes and their expected identical binding modes to the TiO_2 surface. Under these approximations and given that $E(2^+/2^*) > E(1^+/1^*)$, the rate constants for forward electron transfer are expected to follow the relationship $k_F(2) > k_F(1)$. The previous analysis suggests that the ~490 ps fluorescence quenching component seen on the 2-TiO_2 system is not due to the formation of the $2^{\bullet+}$-TiO_2(e–) state and that $k_F(2) > 4.8\times10^{12}$ s^{-1}.

Models for k_B generally involve semiconductor effects such as charge trapping and transport which are not well defined in our system so no detailed analysis will be carried out for this case. It is noteworthy to mention that approaches entirely based on quantum-chemical calculations can be used to estimate dye-TiO_2 electron injection times. [199,238] Such methods have been successfully applied to the study of perylene-TiO_2 systems with phosphonic and carboxylic acid anchoring groups and various spacer groups [199] and will therefore be interesting to apply to the systems described in this work.

Conclusions:

We report the successful sensitization of TiO_2 nanoparticles inside reverse micelles by perylene dyes. These systems having well dispersed oxide nanoparticles of small diameter (< 5 nm) spherical shape and relative narrow size distribution are good

models for the study of dye-semiconductor photoinduced electron transfer reactions in solution. Steady state and transient absorption and emission spectroscopy indicate that perylenes 1 and 2 efficiently attach to TiO_2 nanoparticles inside reverse micelles. The binding of the dyes to the oxide surface involves the attachment of dicarboxylic acid groups produced by hydrolysis of a cyclic anhydride. Binding of perylene 3 to the NPs was inefficient presumably due to steric hindrance resulting from the bulky t-butylphenoxy groups connected at bay positions of the dye. The 1-TiO_2 and 2-TiO_2 systems undergo fast photoinduced electron transfer ($k_f < 210$ fs) to form the dye$^{\bullet+}$-TiO_2(e–) charge separated state. The electron injected into the semiconductor NP recombines with the dye radical cation on a very long time scale ($k_b(1) > 14\mu s$ and $k_b(2) = 30ms$).

It is clear from these observations that the molecular structure of the dye plays an important role in the phenomena we observed. In principle, it should be possible to use dyes with the required substitutions to target specific regions of micro heterogeneous media; it is also possible to modulate the redox potential of the dyes and thereby control electron injection. Therefore, one could use these design parameters to envision applications of molecular systems to sensitize semiconductor nanoparticles located in specific regions of a micro heterogeneous environment. Additionally, one could imagine other applications in which the dyes are used to map complex landscapes by means of their fluorescence.

Acknowledgments:

This work has been supported in part by grants from: the Agencia Nacional de Promoción Científica y Tecnológica (ANPCyT), Argentina (PICT 140/08, 2213/07, 2691/11 and PRH23 PME01); the Consejo Nacional de Investigaciones Científicas y Técnicas (CONICET), Argentina (PIP 11220090100839/10, 11220100100284/11 and CIAM/09); the Secretaría de Ciencia y Técnica, UNRC Argentina; the Ministerio de Ciencia y Tecnología Cordoba, Argentina (PID 2010); the National Science and Engineering Research Council (Canada) and a Tomlinson Award, McGill University; the National Science Foundation, USA (DMR-0908656); the Consejo Nacional de Ciencia y Tecnología, México (CIAM-2008-101939). R.E.P., C.A.C and S.B. are permanent research staff of CONICET. The research of L.I.H. was supported by the ANPCyT through a Ph.D. scholarship. R.G. thanks the NSERC of Canada for a postgraduate scholarship. DDMH is supported by the National Science Foundation Graduate Research Fellowship Program (NSF-GRFP) under Grant No. DGE-0802261 and by the More Graduate Education at Mountain States Alliance (MGE@MSA) Alliance for Graduate Education and the Professoriate (AGEP) National Science Foundation (NSF) Cooperative Agreement No. HRD-0450137. REP thanks the CSACS of McGill University for a visiting professor scholarship. REP thanks Juan Palacios for his generous donation of optical components used in this work.

Supporting Information:

Figures S1-S6 and description for the estimation of the average number of dyes per micelle and per TiO2 NP. This information is available free of charge via the Internet at http://pubs.acs.org.

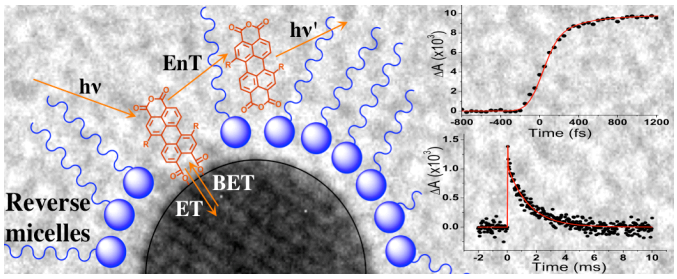

Artistic representation of a micelle-encapsulated TiO_2 NP with perylene derivatives. Background image: high magnification TEM micrograph of a TiO_2 NP. Arrows indicate elemental processes occurring in the system: photon (hν) absorption by the dye, photoinduced Electron Transfer (ET) from the dye to the TiO2 NP, Back Electron Transfer (BET), dye to dye energy transfer (EnT), and dye fluorescence (hν'). The right side graphs show transient absorption kinetic traces corresponding to the formation (top) and decay (bottom) of the $dye^{\bullet+}$-$TiO_2(e–)$ charge separated state.

4.2 Photoinduced electron transfer in perylene-TiO_2 nanoassemblies

Manuel J. Llansola-Portoles [1], Jesse J. Bergkamp [1], John Tomlin [1], Thomas A. Moore [1], Gerdenis Kodis [1], Ana L. Moore* [1], Gonzalo Cosa[2], Rodrigo E Palacios* [3]

[1] Department of Chemistry and Biochemistry, Center for Bioenergy and Photosynthesis, Arizona State University, Tempe, Arizona 85287-1604, USA.

[2] Department of Chemistry and Center for Self Assembled Chemical Structures (CSACS/CRMAA), McGill University, Otto Maass Chemistry Building, 801 Sherbrooke Street West, Montreal, QC, H3A 0B8, Canada.

[3] Departamento de Química, Facultad de Ciencias Exactas Físico-Químicas y Naturales, Universidad Nacional de Río Cuarto, Río Cuarto, Córdoba 5800, Argentina.

*Corresponding author e-mail: amoore@asu.edu (Ana Moore), rpalacios@exa.unrc.edu.ar (Rodrigo Palacios)

Citation:

Article first published 8 July 2013 DOI: 10.1111/php.12108

Journal of Photochemistry and Photobiology

My contributions to this work included synthesis of the perylene dyes and helping in manuscript preparation.

Abstract:

The photosensitization effect of three perylene dye derivatives on titanium oxide nanoparticles (TiO_2 NPs) have been investigated. The dyes used, 1,7-Dibromoperylene-3,4,9,10-tetracarboxy dianhydride (1), 1,7-Dipyrrolidinylperylene-3,4,9,10-tetracarboxy dianhydride (2), and 1,7-bis(4-tert-butylphenyloxy)perylene-3,4,9,10-tetracarboxy dianhydride (3), have in common bisanhydride groups that convert into TiO_2 binding groups upon hydrolysis. The different substituents on the bay position of the dyes enable tuning of their redox properties to yield significantly different driving forces for photoinduced electron transfer (P_{eT}). Recently developed TiO_2 NPs having a small average size and a narrow distribution (4±1 nm) are used in this work to prepare the dye-TiO_2 systems under study. Whereas successful sensitization was obtained with 1 and 2 as evidenced by steady state spectral shifts and transient absorption results, no evidence for the attachment of 3 to TiO_2 was observed. The comparison of the rates of P_{eT} (k_{PeT}) for 1- and 2-TiO_2 systems studied in this work with those obtained for previously-reported analogous systems, having TiO_2 NPs covered by a surfactant layer [239], indicates that k_{PeT} for the former systems is slower than that for the later. These results are interpreted in terms of the different energy of the conduction band edge in each system.

Introduction:

Photoinduced electron transfer (P_{eT}) at dye-semiconductor interfaces plays a central role in a number of technological applications such as solar cells [27,28,132,240], light emitting diodes [241,242], field effect transistors [243-245], advanced catalytic processes [137,246], optoelectronic transducers, etc. The detailed study of photoinduced processes in functioning devices is in general complicated by the spatial heterogeneity of the organic-inorganic interfaces at the nanoscale. The large number of possible dye to semiconductor binding geometries (including dye binding modes, nanoparticle size and distribution) and the potential for generation of dye-aggregates are some of the main factors that contribute to the heterogeneity of these systems and limit the detailed study of P_{eT} processes.

One of the strategies used to try to understand and minimize the heterogeneity effect is to study electron transfer processes in well-defined model nanoassemblies comprised of organic dyes bound to metal oxide particles in suspension [126-128,145,147,158,161,175,182,247]. We recently published a study of P_{eT} processes on a system consisting of perylene dyes bound to TiO_2 nanoparticles inside a micellar structure (dye-TiO_2@micelle) [239]. We selected perylene dyes because they are highly photostable and amenable to the tuning of both their redox and their TiO_2 binding properties trough chemical functionalization [185-187,190,193-195,248,249]. To reduce the size distribution of the inorganic nanoparticles in our previous work we performed the synthesis of TiO_2 particles inside the water pool of reverse micelles (which function as a controlled size nano-reactor). However the presence of surfactant groups surrounding the TiO_2 NPs (TiO_2@micelles) hindered the binding of some of the dyes due to steric effects and

potentially affected the P_{eT} processes in dye-TiO_2@micelle nanoassemblies due to the electric field generated by the surfactant polar heads and corresponding counterions.

Herein we report on the study of P_{eT} on dye-TiO_2 systems assembled from TiO_2 NPs prepared without surfactant molecules and suspended in an organic solvent. Steady state and transient absorption results indicate that in these systems a significant portion of dyes 1 and 2 can bind to TiO_2 NPs and undergo P_{eT} whereas dye 3 is observed to not bind to naked TiO_2. The rate constants for charge injection and charge recombination for dye 1- and dye 2-TiO_2 systems are discussed and compared to those previously acquired with TiO_2 nanoparticles prepared within micellar systems. Advantages and disadvantages for both preparations in terms of the dye-nanoparticle assembly and of charge injection and charge recombination rates are discussed.

Materials and Methods:

Materials

Titanium tetracloride (≥97.0%), dichloromethane (anhydrous, 99.5%) were purchased from Sigma-Aldrich and used as received, all other materials for the preparation of compounds 1, 2, and 3 were the same as reported in reference [239].

Synthesis

Perylenes 1 (1,7-Dibromoperylene-3,4,9,10-tetracarboxy dianhydride), 2 (1,7-Dipyrrolidinylperylene-3,4,9,10-tetracarboxy dianhydride), and 3 1,7-bis(4-tert-butylphenyloxy)perylene-3,4,9,10-tetracarboxy dianhydride were prepared following literature procedures [195,204,239].

Titanium dioxide Nanoparticles (TiO_2 NPs) of (4 ± 1) nm size (see Figure S1 in Supplementary Materials) were prepared by a non-hydrolytic condensation method involving the elimination of alkyl halide between metal alkoxides and metal halides [250-252] (M. Llansola-Portoles, unpublished data). The resulting TiO_2 nanoparticles were dried in ultra high vacuum at 25 ºC for 8 hours to remove physisorbed HCl, which was produced in the synthesis, from the surface of the TiO_2 nanoparticles. After drying, the resulting NP powder was added to freshly distilled THF to achieve the desired NP concentration. Small amounts of HCl remain present on the surface of the TiO_2. Therefore, the nanoparticles zeta potentials kept positive preventing agglomeration and further condensation of the nanoparticles in THF.

Binding of perylene 1 and 2 to TiO_2 NPs was carried out by addition of 100 µL of a stock solution of de dyes (~10^{-4} M) in THF to 3 mL of a TiO_2 NP suspension ([TiO_2] = 0.1 g/L) in THF (for pump-probe experiments dye concentration was increased ten times in an attempt to maximize the amount of dye attached and thus improve the signal corresponding to dye-TiO_2 assemblies). The system was left incubating for > 12 hrs and absorption spectra were recorded at periodic time intervals immediately after addition of the dye.

Instruments and measurements

Absorption spectra were measured on a Shimadzu UV-3101PC UV-vis-NIR spectrometer. Steady-state fluorescence spectra were measured using a Photon Technology International MP-1 spectrometer; measurements were corrected for the detection system response. Excitation was provided by a 75 W xenon-arc lamp and a single grating monochromator. Fluorescence was collected at 90^o to the excitation beam. Fluorescence was detected via a single grating monochromator and an R928 photomultiplier tube operating in

the single photon counting mode.

Fluorescence decay measurements were performed by the time-correlated single-photon-counting method (TC-SPC). The excitation source was a fiber supercontinuum laser based on a passive modelocked fiber laser and a high-nonlinearity photonic crystal fiber supercontinuum generator (Fianium SC450). The laser provides 6-ps pulses at a repetition rate variable between 0.1 – 40 MHz. The laser output was sent through an Acousto-Optical Tunable Filer (Fianium AOTF) to obtain excitation pulses at desired wavelength. Fluorescence emission was detected at the magic angle using a double grating monochromator (Jobin Yvon Gemini-180) and a microchannel plate photomultiplier tube (Hamamatsu R3809U-50). The instrument response function was 35-55 ps. The spectrometer was controlled by software based on the LabView programming language and data acquisition was done using a single photon counting card (Becker-Hickl, SPC-830). Fluorescence anisotropy decays were obtained by changing the detection polarization of the fluorescence path parallel or perpendicular to the polarization of the excitation light. The anisotropy decays then were calculated according to eq. 1, where $I_{VV}(t)$ (or $I_{VH}(t)$) is the fluorescence decay when the excitation light is vertically polarized and only the vertically (or horizontally) polarized portion of fluorescence is detected, denoting that the first and second subscripts represent excitation and detection polarization, respectively. The factor G which is equal to the ratio of the sensitivities of the detection system for vertically and horizontally polarized light can be determined either by so-called tail matching of $I_{VV}(t)$ and $I_{VH}(t)$ or by $I_{HV}(t)/I_{HH}(t)$.

$$r(t) = \frac{I_{VV}(t) - GI_{VH}(t)}{I_{VV}(t) + 2GI_{VH}(t)} \quad (1)$$

The femtosecond transient absorption apparatus consisted of a kilohertz pulsed laser source and a pump-probe optical setup. Laser pulses of 100 fs at 800 nm were generated from an amplified, mode-locked Titanium Sapphire kilohertz laser system (Millennia/Tsunami/Spitfire, Spectra Physics). Part of the laser pulse energy was sent through an optical delay line and focused on to a 3 mm sapphire plate to generate a white light continuum for the probe beam. The remainder of the pulse energy was used to pump an optical parametric amplifier (Spectra Physics) to generate excitation pulses, which were selected using a mechanical chopper. The white light generated was then compressed by prism pairs (CVI) before passing through the sample. The polarization of pump beam was set to the magic angle (54.7°) relative to the probe beam and its intensity adjusted using a continuously variable neutral density filter. The white light probe is dispersed by a spectrograph (300 line grating) onto a charge-coupled device (CCD) camera (DU420, Andor Tech.). The final spectral resolution was about 2.3 nm for over a nearly 300 nm spectral region. The instrument response function was ca. 150 fs.

The nanosecond-millisecond transient absorption measurements were made with excitation from an optical parametric oscillator driven by the third harmonic of a Nd:YAG laser (Ekspla NT342B). The pulse width was ~4-5 ns, and the repetition rate was 10 Hz. The detection portion of the spectrometer (Proteus) was manufactured by Ultrafast Systems. The instrument response function was ca. 4.8 ns.

All TC-SPC and transient absorption data were globally analyzed using locally written software (ASUFIT) (Availible at: www.pulic.asu.edu/~laserweb/asufit/asufit.html) developed under MATLAB (Mathworks Inc.) environment. The model and procedure for global fitting have been described in detail in reference [239]). These global analysis procedures

have been extensively reviewed and random errors associated with the reported lifetimes obtained from fluorescence and transient absorption measurements are typically ≤ 5%.

Transmission Electron Microscopy (TEM) were collected using a Philips CM200 TEM at 200kV/ Cs 1.2 mm/ PTP Resolution: 0.25nm/ Focused Probe: 0.5nm/ Imaging Modes: TEM/STEM.

Multivariate Curve Resolution (MCR). MCR with alternating least squares (MCR-ALS) procedures were applied using a Matlab based routine developed by R. Tauler and A. de Juan. The software is available for free at www.ub.es/gesq/mcr/als2004.htm. Non-negativity (measured and estimated absorbances and concentrations in an experiment will always be non-negative) and closure (sum of concentrations is forced to be equal to a constant value at each stage) constrains were used to obtain a unique solution. More details on the application of the method and program use can be found in the operating manual at http://www.ub.edu/mcr/als2004/manual.pdf.

Results and Discussion

Dyes' structure and energetics

The molecular structures of the perylene derivatives used as sensitizers in this work are shown in Scheme 1a. All dyes have two anhydride groups that are subject to hydrolysis under basic conditions (see Scheme 1b) or in the presence of TiO_2 nanoparticles to yield the corresponding dicarboxylate groups [239]. In their hydrolyzed "open form" the dyes are able to bind to the surface of TiO_2 nanoparticles through the dicarboxylate anchoring group by chemical bonding and/or electrostatic attraction

[239,253,254] to yield the open bound dye species. The redox properties of the dyes were tuned by the attachment of electron donating or withdrawing groups at the bay positions. Scheme 1c shows the energy diagram of the dye-TiO_2 system taken from reference [239]. In this diagram the energy for the conduction band edge (E_{CB}) of the TiO_2 nanoparticles was estimated as the flat band potential (V_{fb}) of polycrystalline TiO_2 in water at pH=2 ($V_{fb,W/pH=2}$ = -0.52 V, vs SCE) to account for the concentration of protons inside the micelle water pool (where the TiO_2 NPs were synthesized) [239,255]. On the other hand, the TiO_2 NPs used for the experiments described in this work are suspended in a THF solution which contains trace amounts of acidic water. The V_{fb} of TiO_2 in neat THF has been reported as $V_{fb,THF}$ = -2.34 V (vs. SCE) [255]. However the V_{fb} in nonaqueous solutions is mainly determined by the potential establishment of proton adsorption-desorption equilibrium involving solvent molecules and TiO_2 [255]. Since such equilibrium is not possible in nonaqueous aprotic solvents (e.g. THF) the V_{fb} value in these solvents is strongly affected by trace amounts of protic impurities (e.g. the presence of trace amounts of water lead to significantly positive shifts in (V_{fb}) [255]. Considering these factors, the effective E_{CB} value for the TiO_2 NPs used in this work cannot be accurately defined but it is estimated to fall between -0.52 V and -2.34 V (vs. SCE). As it will be discussed, transient-absorption experiments show evidence for P_{eT} in 1-TiO_2 and 2-TiO_2 systems indicating that the effective E_{CB} in these systems must be only slightly more negative than -0.52 V so that P_{eT} from the dyes excited state to the TiO_2 CB is thermodynamically favorable.

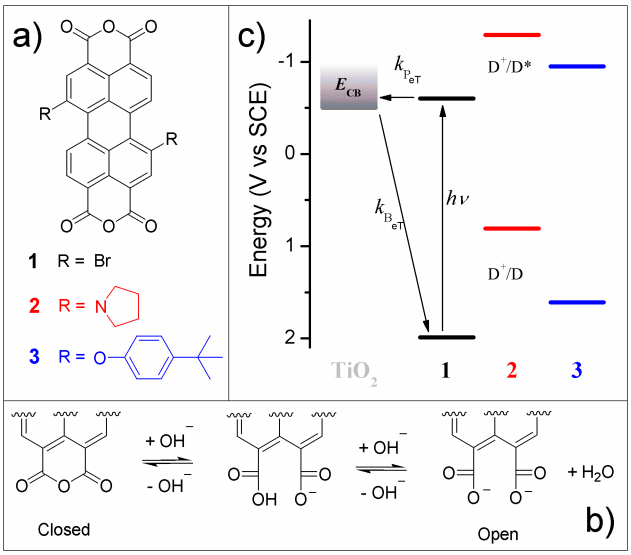

Scheme 1: Panel a shows the three perylene dyes used for this study. The 1,7 di-bromo in black, 1,7 di-pyrrolidine in red and the 1,7 di-(4-tert-butyl phenoxyl) in blue. Panel b shows the mechanistic ring opening reaction of the anhydride to the di-carboxylic perylene. Panel c show the energy levels of each perylene dye with respect to the conduction band of TiO_2.

Dye-TiO_2 nanoassemblies

Steady state absorption

The binding of the dyes to TiO_2 NPs was followed by monitoring over time the shift of their absorption spectra in the presence of nanoparticles. This is possible because upon opening of the anhydride ring and binding to TiO_2 the absorption spectra of the dyes shift to higher energies [195,248,256-258]. This shift can be associated to a reduction of the effective conjugation length of the chromophore [186,248,256,259] and has been previously characterized for the dyes used in this work in ethanolic solution and upon binding of 1 and 2 to TiO_2 [239]). Figure 1 shows the absorption spectra as a function of time following addition of dye to a TiO_2 NP suspension in THF. For the 1-TiO_2 system a significant absorbance shift was observed after 12 hrs (Figure 1a) indicating that binding of the dye is slow under the studied conditions. In contrast, significant changes in the absorption occurred within 30 min for the 2-TiO_2 system (Figure 1b, insert). The magnitude of the absorption shift (~70 nm) observed upon incubation of dye 2 with surfactant-free ("naked") TiO_2 nanoparticles (2-TiO_2) is significantly larger than that previously observed upon incubation with TiO_2 NP covered by a layer of surfactant molecules (2-TiO_2@micelle) (~24 nm) [239]. Additionally, the absorption shift observed for the 2-TiO_2 system is similar to that previously observed upon exhaustive basic hydrolysis of dye 2 in ethanol solution (where presumably both anhydride groups are hydrolyzed yielding a maximum absorption shift of ~130 nm) [239]. These observations are consistent with the idea that binding of dye 2 to naked TiO_2 NPs can occur at least partly through both dicarboxylic acid groups (product of the hydrolysis of both anhydride rings) whereas dye 2 binds to TiO_2@micelle NPs via one dicarboxylic acid moiety (resulting from hydrolysis

of only one anhydride ring). The surfactant molecules on the TiO_2@micelle NPs presumably preclude the formation of dye-NP geometries where both anhydride rings are close enough to the NP surface (and/or remaining water pool) to hydrolyze and bind simultaneously. Thus, dye-NP binding geometries involving both dicarboxylic groups in one particle and others where the dye acts as a bridge between two nanoparticles are in principle possible for naked TiO_2 NPs but very unlikely for TiO_2@micelle NPs.

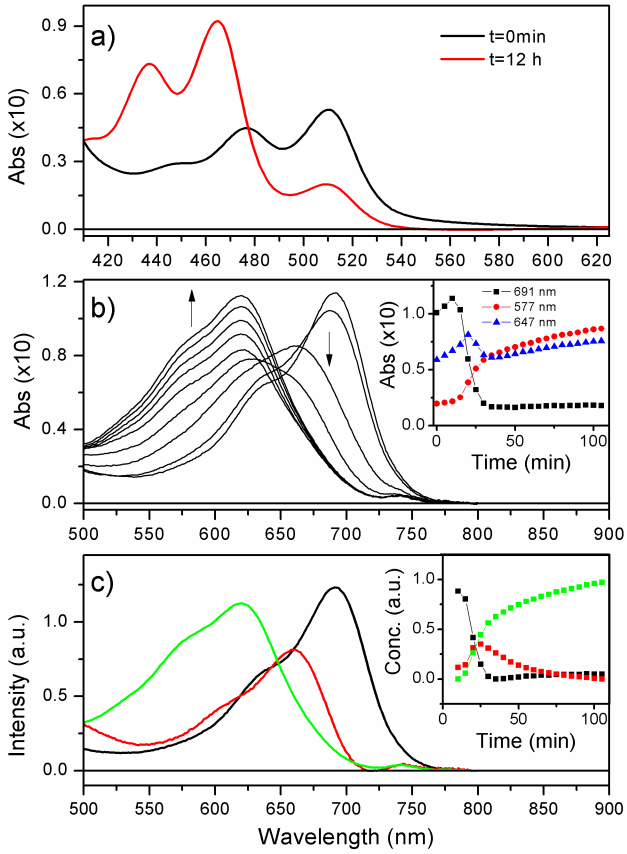

Figure 1: a) Time sequence of absorption spectra collected after addition of 1 to a suspension of TiO_2 NPs in THF. [Dye] = ~ 10^{-6} M, estimated [NP] = ~ 0.1 mg/mL. b) Same as (a) for dye 2. The first and last spectra were collected at 0 min and 105 min, respectively. The insert displays kinetic traces at specific wavelengths. c) Species spectra obtained by MCR analysis of data in (b). The insert shows the concentration time evolution for each species (color coded).

In order to identify the spectra of the different species present upon hydrolysis and subsequent binding of 2 to TiO_2 NPs we used MCR techniques. Analysis of the absorption spectra time sequence shown in Figure 1b using the MCR-ALS method (Multivariate curve resolution software mcr-als gui. Available at: (http://www.ub.edu/mcr/web_mcr/download.html.) is shown in Figure 1c. The results indicate the presence of three species with distinct peak absorptions at 691 nm (Species A), 658 nm (Species B) and 620 nm (Species C) that can be in principle associated with the hydrolysis of none, one and both anhydride rings, respectively. The insert shows the concentration of each species as a function of time indicating a stepwise interconversion between species, i.e. A ↔ B ↔ C. The assignment of A, B and C species to the closed, mono-hydrolyzed and di-hydrolyzed dye species is further supported by MCR analysis of data corresponding to the basic hydrolysis of 2 in ethanol (see Figure S2a in Supplemental Materials) which also shows the presence of three inter-converting species (driven by basic titration) with spectral features analogous to the species shown in Figure 1C. Similar analysis of the data corresponding to the incubation of dye 2 with TiO_2@micelle NPs [239] yields only two species with peak absorptions at 688 nm and 664 nm (see Figure S2b in the Supplementary Materials) presumably corresponding to the closed and mono-hydrolyzed species.

In contrast to the spectral shift observed for 1 and 2 in the presence of TiO_2 NPs, the absorption spectrum of dye 3 did not significantly shift over time under the same conditions (see Figure S3 in the Supplementary Materials). This result suggests that dye 3 does not bind to naked TiO_2 nanoparticles and thus no additional experiments to investigate P_{eT} were performed with this dye-TiO_2 NP system. Further evidence and

discussion for the lack of binding of 3 is given in the time resolved fluorescence anisotropy section (see below).

Steady state and Time resolved emission

Recently we reported a large quenching of dye emission (due to P_{eT}) upon binding of 1 and 2 to TiO_2 in a micellar system [239]. Attempts to quantitatively determine dye emission quenching for 1 and 2 in solution by steady state fluorescence measurements with and without naked TiO_2 NPs failed due to the presence of unattached dyes and of dye aggregates (see time resolved fluorescence measurements below) which partially dissolve over time and then bind to the TiO_2 NPs.

Transient fluorescence measurements (TC-SPC) were performed to investigate the kinetics of the emission of dyes 1 and 2 in the presence of TiO_2 NPs (see Figures S4a and S4b, respectively in the Supplementary Materials). Results for solutions of 1 incubated with TiO_2 NPs show fluorescence Decay Associated Spectra (DAS) with three components of 100 ps, 850 ps, and 3.9 ns ($\chi^2 = 1.18$). The 100 ps and 850 ps components could be associated with dye aggregates where the dye is in the closed form suspended in solution and showing significant auto-quenching. It is well known that perylenes are prone to aggregate and crystallize to afford typically weakly luminescent particles. The main driving force for aggregation comes from strong intermolecular π−π-stacking interactions resulting from the extended π-system and large quadrupole moment of perylenes. The fluorescence quenching mechanism most likely involves enhancement in the rate of internal conversion to the ground state due to exciton (dipole-dipole) interactions. Alternatively the 100 ps and 850 ps components could be associated to the

emission of the dye when physisorbed on the surface of nanoparticles in its closed form and thus with a low electronic coupling for P_{eT}. Further evidence for dye aggregates is shown in the time resolved fluorescence anisotropy measurements (see below). The 3.9 ns component is associated to the emission from 1 in its closed form and non-aggregated in solution. On the other hand, the fluorescence DAS of solutions of 2 incubated with TiO_2 NPs yielded two fluorescence DAS components ($\chi^2 = 1.12$) with lifetimes of 71 ps and 2.5 ns. The 71 ps component with maximum at 740 nm could be associated with aggregates of 2 closed species which show a short fluorescence lifetime due to auto-quenching. The 2.5 ns component is associated with 2 in its closed form and non-aggregated in solution.

Time resolved fluorescence anisotropy

To further investigate the diffusion rotational properties of the emitting species in the studied samples we performed time resolved fluorescence anisotropy measurements. Figure 2 shows time resolved fluorescence anisotropy decays of the dyes in THF solutions with and without the addition of TiO_2 NPs. As seen in Figure 2a the decay of dye 1 in solution can be fitted with a single exponential lifetime of 115 ps similar to that observed in n-heptane (81 ps) [239]. In the presence of TiO_2 NPs the anisotropy decay can only be satisfactorily fitted with two exponential components (115 ps and 890 ps). The shorter component can be associated with the reorientation dynamics of free dye in solution or energy transfer among dyes in aggregates since both situations are possible and create a fast depolarization effect in the emission. The 890 ps component can be ascribed to the presence of dye molecules physisorbed on the surface of TiO_2 NPs or covalently bound to surface defects such that the effective dye-TiO_2 electronic coupling

(H) for P_{eT} is very small and consequently the dye fluorescence is not significantly quenched. These putative dye-TiO_2 assemblies are significantly larger than a free dye in solution and consequently have much slower reorientation dynamics. Thus the 890 ps anisotropy component can be associated with the rotational correlation time of a sphere with a radius of 1.2 nm (see Supplementary Materials) which is in close agreement with the size of our TiO_2 nanoparticles (diameter 4±1 nm). An analogous situation, but with longer time constants, is observed for dye 2 (see Figure 2b). The free dye in solution shows a mono-exponential decay with a lifetime of 253 ps and in the presence of NPs it shows a bi-exponential decay with 253 ps and 1.36 ns components. These results are consistent with the larger molecular size of 2 vs. 1 [239] and consequently slower reorientation. In contrast to this, dye 3 shows fast mono-exponential decays for both situations, the free dye in solution (265 ps) and in the presence of TiO_2 NPs (188 ps) (see Figure 2c). The results indicate that dye 3 does not physisorbe or bind to TiO_2 NPs which is consistent with the lack of absorption shift observed when the dye is incubated in the presence of NPs (see Figure S3 in the Supplementary Materials). The lack of binding of dye 3 to TiO_2@micelles NPs was previously reported by our group and rationalized invoking strong steric interactions between surfactant molecules and the bulky t-butylphenoxy groups of the dye which prevented the formation of geometries where one anhydride ring was close enough to the TiO_2 surface to achieve binding [239]. The new results presented herein indicate that even in absence of micelles in the system, the t-butylphenoxy groups present strong steric hindrance to reach dye-TiO_2 NPs geometries necessary for efficient attachment.

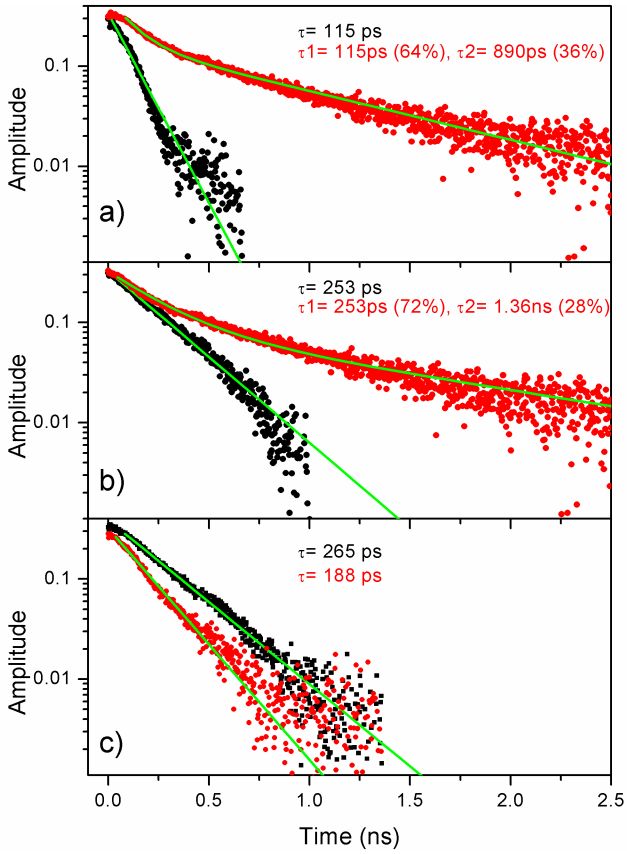

Figure 2: a) Fluorescence anisotropy decays (data points) of 1 in THF without (black) and with TiO_2 NPs (red). Green smooth lines show exponential fits to the data. Samples were excited and emission collected at the following wavelengths: λ_{ex}= 450 nm λ_{em}= 550 nm. b) Same as (a) for dye 2: λ_{ex}= 600 nm λ_{em}= 760 nm. c) Same as (a) for dye 3: λ_{ex}= 450 nm and λ_{em}= 550 nm. Dye concentration was ~ 10^{-6} M for all samples.

Time resolved absorption

Time resolved transient absorption techniques were used to investigate the kinetics of P_{eT} in the dye-TiO_2 nanoassemblies. Measurements in the femtosecond to nanosecond (pump-probe) and nanosecond to microsecond (flash-photolysis) time-ranges were performed in an attempt to measure the kinetics of formation and recombination, respectively, of the dye$^{\bullet+}$-TiO_2(e–) charge separated state.

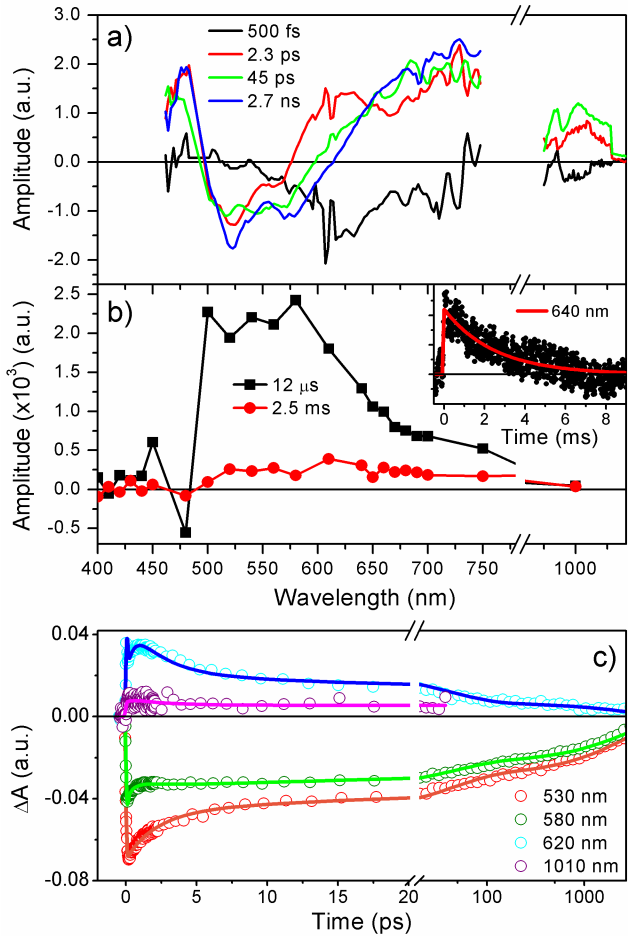

Figure 3: a) DAS spectra of 1-TiO_2 nano-assemblies in THF solution measured by pump-probe (fs to ns range). Data was acquired with pump laser excitation at λ_{ex} = 490 nm..b) Same as (a) measured by flash-photolysis (ns to µs range) upon λ_{ex} = 440 nm.. c) Kinetics traces (data points) and fits (smooth lines) at selected wavelengths corresponding to the data shown in (a).

Figures 3a and 3c show pump-probe results for the 1-TiO_2 system with excitation at 490 nm. Global analysis of the kinetic data shows four decay components with lifetimes of ~ 500 fs, 2.3 ps, 45 ps, and 2.7 ns (see Figure 3a). The decay associated spectra (DAS) of the 500 fs component can be attributed to P_{eT} from 1 open bound species to TiO_2 to form the $1^{\bullet+}$-TiO_2(e−) state. The following spectral features support this assignment: a) decay of stimulated emission (negative amplitude) corresponding to 1 open bound at ~ 520 nm (see Figure S5a, red dashed line in the Supplemental Materials), b) formation of 1 radical cation (negative amplitude) with characteristic induced absorption at ~ 630 nm, and c) formation of free carriers (injected electrons) in the TiO_2 semiconductor (TiO_2(e–)) (negative amplitude) with absorption around 1000 nm. The 2.3 and 45 ps components show a mixture of two main processes: (a) decay of singlet excited state of the 1 closed species (as seen in the TC-SPC data, Figure S4a in the Supplementary Materials) and (b) decay of the $1^{\bullet+}$-TiO_2(e−) charge separated state with positive amplitudes at ~ 630 nm ($1^{\bullet+}$ absorption) and 850−1000 nm (TiO_2(e−) absorption). The last 2.7 ns DAS can be attributed mostly to the decay of singlet excited state of 1 closed form (presumably free in solution), showing ground state bleaching and stimulated emission from ~ 520 nm to 570 nm, and induced absorption at 470 nm and 750 nm.

Transient absorption measurements on the 1-TiO_2 system in the nanosecond to millisecond time range were performed to complement the pump-probe data; the results are shown in Figure 3b. Global analysis of the kinetics in argon saturated solution yields two components, 2.5 ms and 12 μs (excitation at 440 nm). The 2.5 ms component is associated with the decay of the $1^{\bullet+}$-TiO_2(e−) state showing positive amplitude signals

around 630 nm ($1^{\bullet+}$ absorption, see kinetic trace in Figure 3b insert) and up to ~ 950 nm ($TiO_2(e-)$). The 12 μs component is oxygen sensitive and it is associated with the decay of triplet excited states of 1 (in open and closed forms) showing transient absorption in the ~ 500−700 nm range and ground state bleaching at 450 nm and 520 nm (small dip).

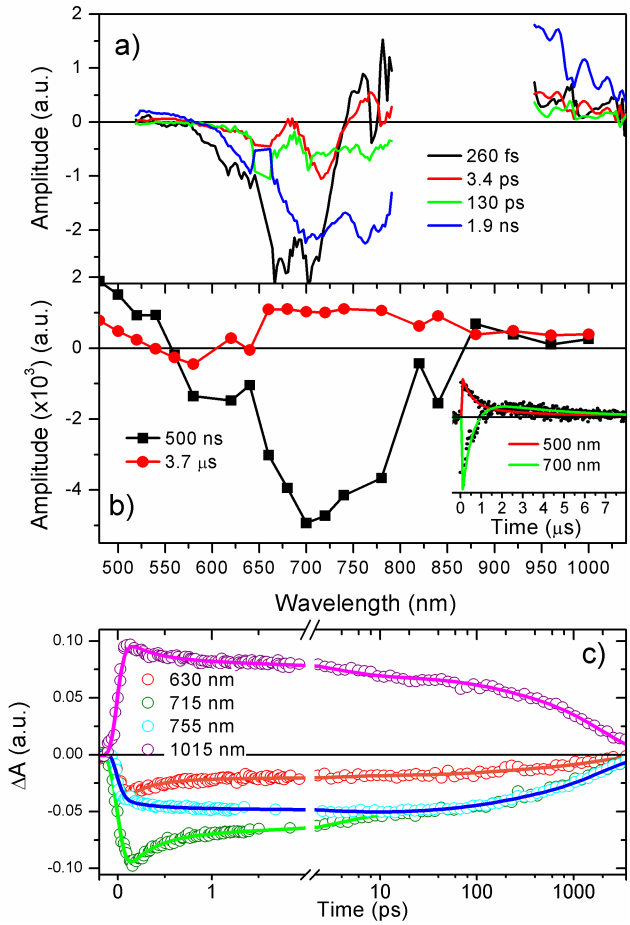

Figure 4: a) DAS spectra of 2-TiO_2 nano-assemblies in THF solution measured by pump-probe (fs to ns range). Data was acquired with pump laser excitation at λ_{ex} = 650 nm. b) Same as (a) measured by flash-photolysis (ns to μs range). λ_{ex} = 640 nm. c) Kinetic traces (data points) and fits (smooth line) at selected wavelengths corresponding to the data shown in (a).

Figure 4a and 4c show pump-probe results with excitation at 650 nm for 2-TiO_2 nanoassemblies. Global fit to the data yields four decay associated spectra components of 260 fs, 3.4 ps, 130 ps, and 1.9 ns (see Figure 4a). The 260 fs component is mainly associated with singlet energy transfer from the open form of the dye to the closed one and possibly, to some extent, to the formation of the $2^{\bullet+}$-TiO_2(e–) charge separated state. This component shows the following spectral features: a) stimulated emission decay (negative amplitude) of 2 open species in the 660 nm to 730 nm region (consistent with the red dashed spectra in Figure S5b in the Supplementary Materials), b) formation of stimulated emission of the dye in its closed form with a positive amplitude around 760 nm and c) $2^{\bullet+}$ transient absorption formation (negative amplitude) above 650 nm. In addition to this, the ground state bleaching of open dye 2 (around 600 nm) decays to some extent with the same lifetime (260 fs) and there is no rise with 260 fs at 1000 nm. Therefore we do not have strong spectral evidence of $2^{\bullet+}$-TiO_2(e–) formation on the time scales measured. It is likely that charge separation is very fast and occurs in less than 150 fs (instrument response time of our apparatus). Transient absorption at 1015 nm supports this assumption showing a kinetic trace with instantaneous rise, limited by instrument response (see Figure 4c, violet data points). The 3.4 ps DAS component is assigned to solvation-induced band-shift of the emission band of 2 closed species. The 130 ps and 1.9 ns components show a mixture of two main processes: (a) recovery of ground state bleaching and stimulated emission of 2 closed species (presumably slightly aggregated and/or physisorbed on the NPs) consistent with its close temporal match to the emission DAS components shown in Figure S4b in the Supplementary Materials (71 ps and 2.5 ns) and (b) recovery of ground state bleaching of the open-bound form of 2 (due to

recombination of the $2^{\bullet+}$-TiO_2(e–) state) showing negative amplitude in the region around 640 nm.

Figure 4b shows flash-photolysis results with excitation at 640 nm for the 2-TiO_2 system. Global analysis of the data yields two DAS components of ~ 500 ns and 3.7 μs. The shorter component is associated with the triplet state of the dye in its closed and open forms showing ground state absorption bleaching recovery (negative amplitude) from 570 nm to ~ 800 nm (2 closed species, see Figure 4a solid black spectrum) and triplet state transient absorption decay (positive amplitude) below 550 nm. The 3.7 μs component is associated with the decay of the $2^{\bullet+}$-TiO_2(e–) charge separated state. This long component shows ground state bleaching of 2 fully open bound species in the 500 nm to 650 nm region (consistent with the solid red spectra Figure S5b in the Supplementary Materials) and $2^{\bullet+}$ transient absorption above 650 nm (consistent with previously reported transient features of $2^{\bullet+}$ [239].

A comparison of the dynamics of P_{eT} in dye-TiO_2@micelle NPs vs dye-TiO_2 systems shows that the P_{eT} rate (k_{PeT} Scheme 1c) for 1-TiO_2 (k_{PeT} (1, naked) = 1/500 fs) is slower than that for 1-TiO_2@micelle (k_{PeT} (1, micelle) = 1/210 fs). On the other hand, for both the 2-TiO_2@micelle and 2-TiO_2 systems the corresponding k_{PeT} rates are faster than the time resolution of our pump-probe instrument, so no comparison can be made in this case. Regarding the kinetics of recombination of the dye$^{\bullet+}$-TiO_2(e–) state (k_{BeT}, Scheme 1c), k_{BeT} (1, naked) = 1/2.5 ms is slower than k_{BeT} (1, micelle) ~ 1/1.5 ms and k_{BeT} (2, naked) = 1/3.7 μs is faster than k_{BeT} (2, micelle) ~1/30 ms.

The measured P_{eT} rate constants can be discussed in terms of Equation 2 [145,260-264]

where ρ (E) is the effective density of states at the energy E relative to the conduction band edge (E_{CB}), f(E) represents the Fermi distribution function, $\overline{H}(E)$ is the average electronic coupling between the dye excited state and all k states in the semiconductor, λ is the total reorganization energy, and $\Delta G^0 = E_{CB} - E(D^+/D^*)$. To a first approximation $\overline{H}(E)$ and λ are assumed to be the same for all the dye-TiO_2 systems given the analogous structure of the dyes and their expected identical binding modes to the TiO_2 surface.

(2) $$k_{PeT} = \frac{2\pi}{\hbar}\int_{-\infty}^{\infty} \rho(E)\left(1 - f(E)\right)\left|\overline{H}(E)\right|^2 \left(4\pi\lambda k_B T\right)^{-1/2} e^{-\frac{(\lambda+\Delta G^0+E)^2}{4\lambda k_B T}} dE$$

As was discussed before, the E_{CB} (naked) is more negative than E_{CB} (micelle), thus $|\Delta G^0(\text{naked})| < |\Delta G^0(\text{micelle})|$ and $k_{PeT}(\text{naked}) < k_{PeT}(\text{micelle})$ (assuming P_{eT} in the normal Marcus region [265] which is consistent with the experimental results.

Since models for k_{BeT} involve charge trapping and transport effects, which are not well, defined in our nanoparticles no detailed analysis is presented for this case.

Conclusions

The main objective of this work was to study the sensitization effect of perylene dyes in surfactant-free TiO_2 NPs with small average size and relatively narrow size distribution in THF. In principle, these particles present the opportunity to construct simple dye-TiO_2 systems, as compared to the previously reported dye-TiO_2@micelle assemblies, to investigate P_{eT} processes. The added surfactant layer in the later systems presumably affects the dye-TiO_2 PeT processes due to the highly directional electric field produced by the surfactant polar groups and corresponding counterions. Thus, in this

sense the dye-TiO_2@micelle systems are complex ones characterized by a larger number of variables as compared to the dye-TiO_2 systems used in this work. However, problems related to dye aggregation in THF and the potential formation of dye-NP aggregates in which two NPs can be linked by bridging perylenes (due to its ability to function as bifuntional anchors) created unanticipated complications in the formation of the dye-TiO_2 systems studied herein. In the case of bridging, the micelle structure provides an organizing scaffold that prevents the formation of NPs aggregates. The results of this study highlight the importance of several factors including solubility, the presence of multiple anchoring groups, and steric hindrance of bay groups that affect binding geometries that must be considered in the design of perylene derivative dyes as P_{eT} sensitizers for inorganic semiconductor nanoparticles.

Acknowledgments

This work has been supported in part by the National Science Foundation, USA, DMR-0908656 (synthetic studies) and as part of the Center for Bio-Inspired Solar Fuel Production, an Energy Frontier Research Center funded by the U.S. Department of Energy, Office of Science, Office of Basic Energy Sciences under Award Number DE-SC0001016 (transient spectroscopic studies). Additional support was given by grants from: the Agencia Nacional de Promoción Científica y Tecnológica (ANPCyT), Argentina (PICT 140/08, 2213/07, 2691/11 and PRH23 PME01); the Consejo Nacional de Investigaciones Científicas y Técnicas (CONICET), Argentina (PIP 11220090100839/10, 11220100100284/11 and CIAM/09); the Secretaría de Ciencia y Técnica, UNRC Argentina; the Ministerio de Ciencia y Tecnología Cordoba, Argentina (PID 2010). We also thank funding from he National Science and Engineering Research

Council (Canada) and a Tomlinson Award, McGill University. R.E.P. is permanent research staff of CONICET.

Supplementary Information

Figures S1 to S6 can be found at DOI: 10.1562/2013-xxxxxx.s1.

CHAPTER 5

SYNTHESIS AND RESULTS

Phthalocyanines bearing carboxylic acid anchoring groups on both their axial and peripheral positions have been synthesized. Compounds **12** and **13** (figures 1 and 2) have the carboxylic acid on the axial position via a Si-O-C ether linkage. Both of these Pcs have shown photocurrent in Grätzel type solar cells (see figures 5 and 6). The dye loading for **13** was higher than that of **12** on TiO_2 electrodes as seen in figures 6a and 4, respectively. This is presumably because of the spacing between the anchoring group and the macrocycle. As seen in compound **12** the carboxylic acid only has one methylene that would space the Pc from the electrode (figure 1), and with the butoxy groups being in close proximity, they could potentially block the interaction of the acid with the TiO_2 surface. Moreover, compound **13** bears a phenyl ring (figure 2) that provides more space between the macrocycle and the electrode. When compound **11** is adsorbed onto a TiO_2 electrode, a higher dye loading is observed than with compounds **12** (figure 4) and **13** **(**figure 6a). This is attributed to the fact that the anchoring group is on the peripheral of the Pc (figure 3). Therefore, the spatial geometry of the dye on the surface is perpendicular, yielding a system capable of packing more Pc within a given area of the surface (figure 7). In contrast, the axial Pcs in the same area of the surface, would bear fewer Pcs per electrode area because they adsorb parallel or flat to the surface (figure 7).

Interestingly, **11** shows a lower photocurrent than that of **13**, even though more dye is adsorbed to the surface (figure 6b and c). This is presumably due to energy transfer from Pc to Pc along the surface of the electrode instead of forward electron injection into TiO_2 as seen in figure 7. One important aspect that affects the efficiency of the dual-

threshold photoelectrochemical cell is the absorption of red photons that lead to photocurrent by the cathodic dye. As seen in figure 6d, compound **11** yields lower incident photon to current efficiency than compound **13**. The axial Pc **13** has produced the best dye loading and photocurrents of the molecules tested herein.

The synthetic steps to obtain compound **8** can be seen in scheme 1. First, meso-free dipyrromethane, **1**, was obtained by following a literary procedure from Laha et al. [266]. Reacting compounds **1**, **2** and **3** in a standard Lindsey type condensation reaction using boron trifluoride and ethanol in chloroform followed by oxidation using 2,3-dichloro-5,6-dicyano-1,4-benzoquinoe (DDQ) yielded porphyrin **4**. A standard S_N2 nucleophilic substitution reaction was performed to yield porphyrin **5** by reacting **4** with diethyl malonate, sodium hydride was used as the base with tetrahydrofuran as the solvent. The next step in the sysntesis was bromonation of the meso-postitons, which was done using N-bromosuccinimide as the bromine source, pyridine as the base and chloroform as the solvent to yield porphyrin **6**. A Suzuki palladium cross-coupling reaction was utilized to place the pyridyl groups on porphyrin **7**. This was done by reacting porphyrin **6** with 4-pyridineboronic acid pinacol ester, palladium triphenylphosphine and potassium carbonate in dioxane. For the final steps, porphyrin **7** was reacted with methyl iodide in dimethylformamide followed by base hydrolysis using potassium hydroxide in tetrahydrofuran and water to yield porphyrin **8**.

The synthesis of compound **11** was executed by starting with a substituted phthalonitile **9** (scheme 2). Compound **9** was prepared from the starting material, 3,6-dihydroxyphthalonitile which was bromonated using NBS under standard conditions to yield the mono and di bromo substituted phthalonitile. The mixture of mono and di

bromo phthalonitiles proved difficult to separate, therefore the next step in scheme 1 was carried out. The next step was the formation of the butoxy groups; this was done following a literature procedure [267]. The butoxylation was carried out in methyl ethyl ketone as solvent along with potassium carbonate as base, followed by the addition of iodobutane. Interestingly, the 4-bromo-3,6-dibutoxyphthalonitrile and the 4,5-dibromo-3,6-dibutoxyphthalonitrile were difficult to separate as well, therefore the mixture was taken on to the next step. A Suzuki cross-coupling reaction was used to form the carbon-carbon bond between 4-(ethoxycarbonyl)phenylboronicacid and the mixture of phthalonitriles. At this stage the purification of the mono and di substituted phthalonitiles was achieved to yield compound **9** (scheme 2). Compound **9** was reacted with 3 equivalents of 3,6-dibutoxyphthalonitile in butanol along with lithium metal to yield phthalocyanine **10**. Upon purification of **10**, it was clear that a transesterifaction reaction had occurred between the ethyl group on the ester and the solvent (scheme 3). Phthalocyanine **10** was reacted with potassium hydroxide in tetrahydrofuran, ethanol and water to yield the carboxylic acid Pc **11** (scheme 4).

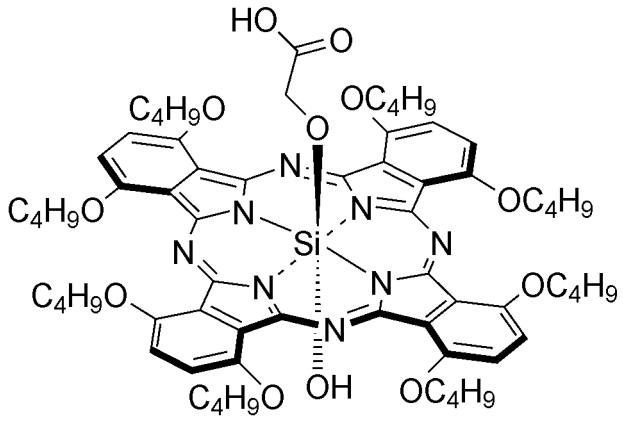

Figure 1: Structure of compound **12**.

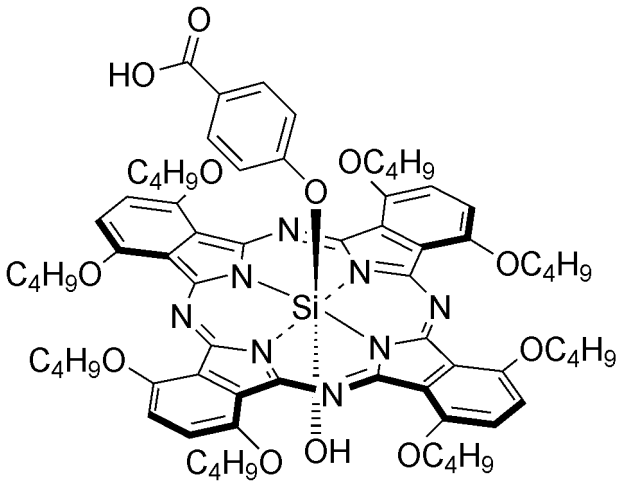

Figure 2: Structure of compound **13**.

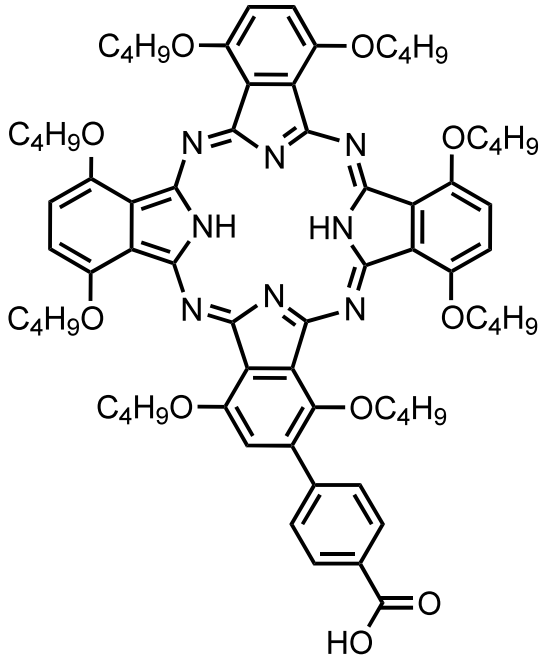

Figure 3: Structure of compound **11**.

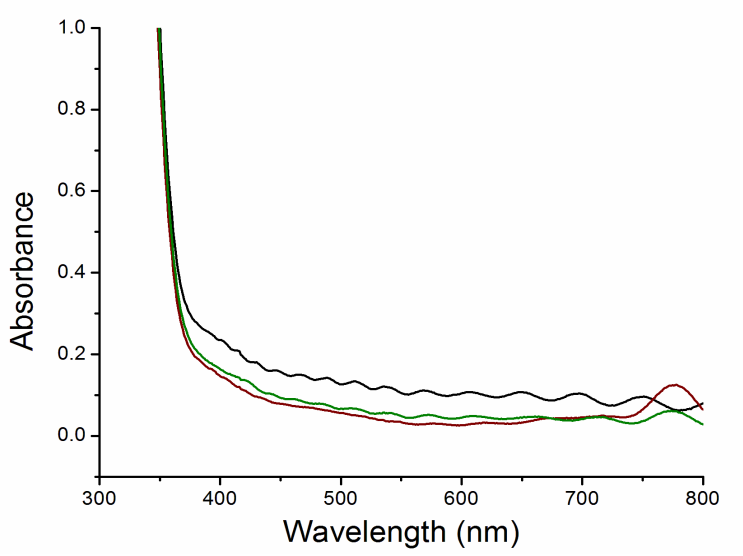

Figure 4: UV-Vis ground state absorption spectra of compound **12** adsorbed onto a TiO_2 electrode. Three different adsorption conditions were used. Dye **12** was dissolved in ethanol (black), dichloromethane/methanol 50:50 (green) and dichloromethane (red). As seen the highest dye loading was achieved using dichloromethane. The absorption at ~780 as seen in the red curve, is the Q-band of the Pc. The green and black curves show considerable scattering from the electrode throughout the spectra due to lack of Pc adsorbed. Therfore, the solvent used to adsorb the Pc is very important to achieve high dye loadings.

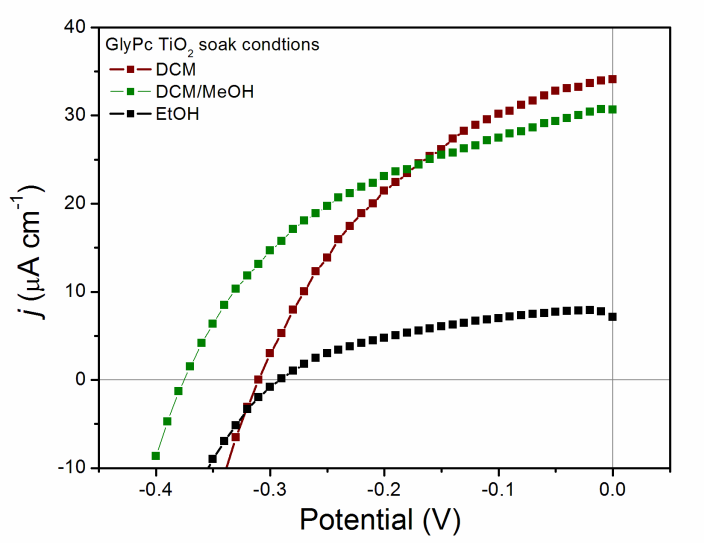

Figure 5: Photocurrent trace showing current density vs. applied potential of compound **12** in a Grätzel type solar cell. Three different TiO_2 electrodes were used from three different soak conditions.

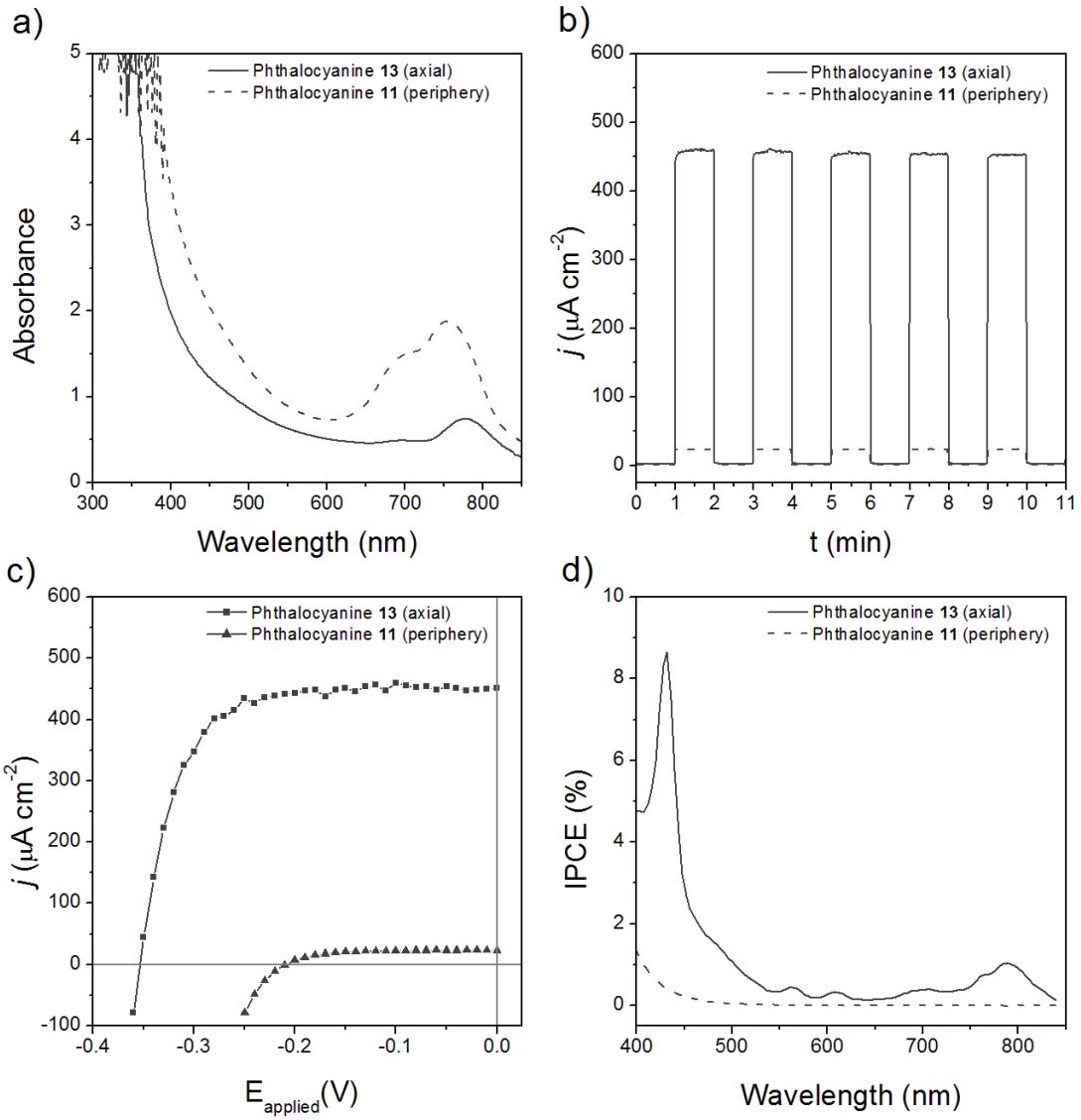

Figure 6: Comparison of axial Pc **13** (solid line) and peripheral Pc **11** (dashed line). Panel a) shows the ground state UV-Vis absorption spectra of Pcs adsorbed onto TiO_2 electrodes from a dichloromethane solution. Panel b) shows photocurrent traces with light and dark iterations, starting in the dark at time zero with one-minute intervals of light on/off. Panel c) shows a j/V plot with applied potential on the x-axis and current density of the y-axis. Panel d) shows an incident photon to current efficiency (IPCE) plot.

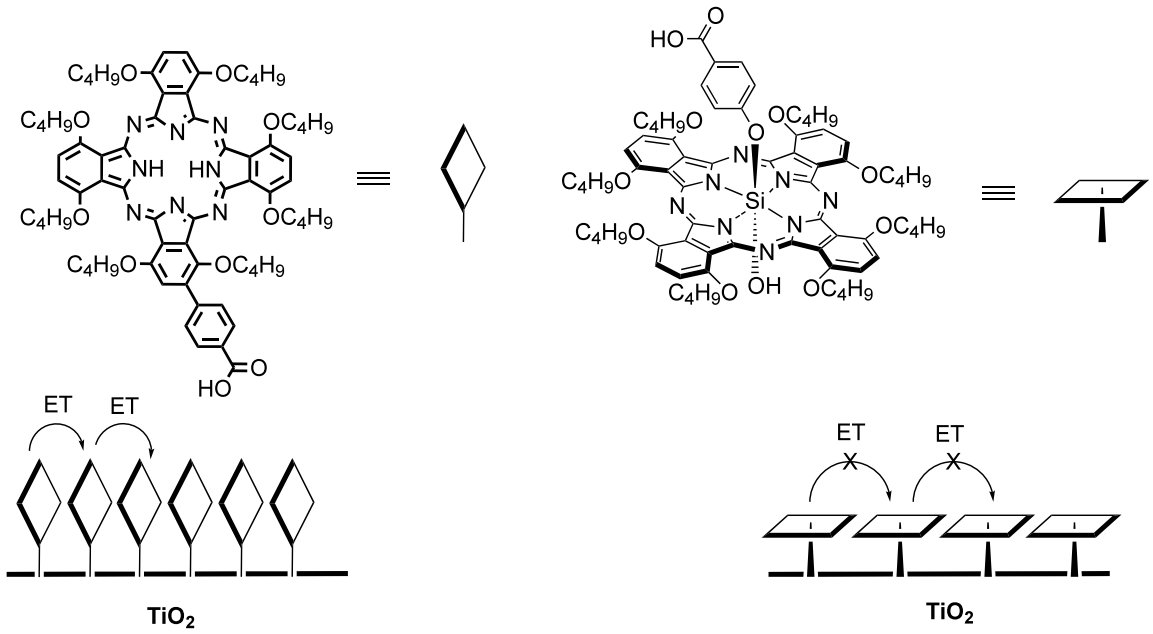

Figure 7: Schematic drawing showing presumable orientations of both axial and peripheral Pc on the electrode.

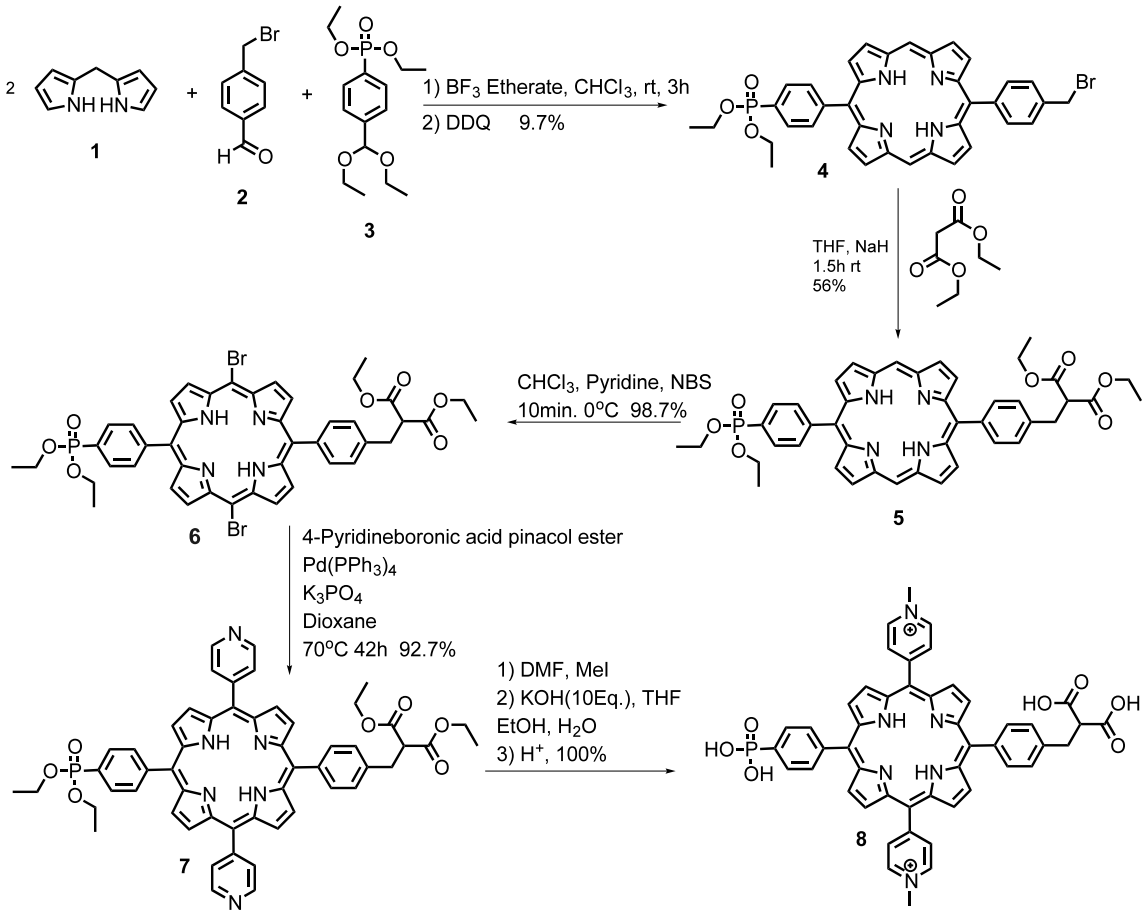

Scheme 1: Synthetic steps for obtaining compound **8**.

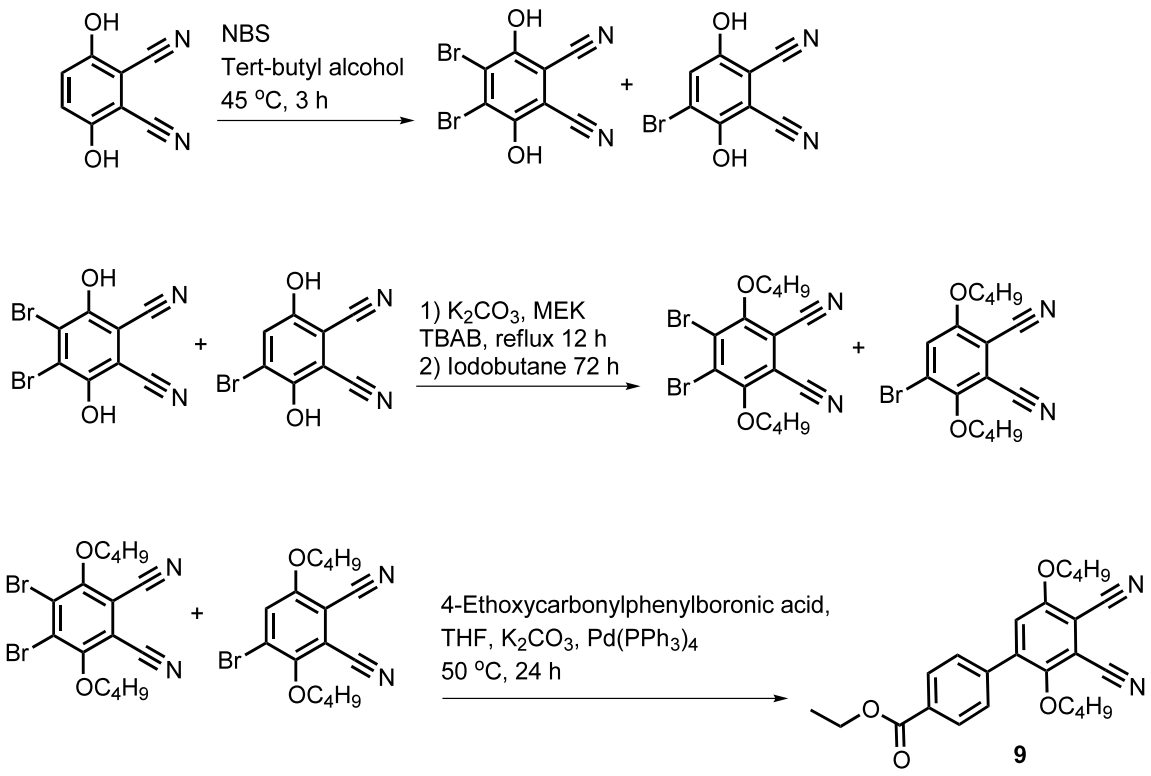

Scheme 2: Synthetic steps to obtain compound **9**. The diphenylester phthalonitrile was obtained as well but in much lower yield than compound **9**.

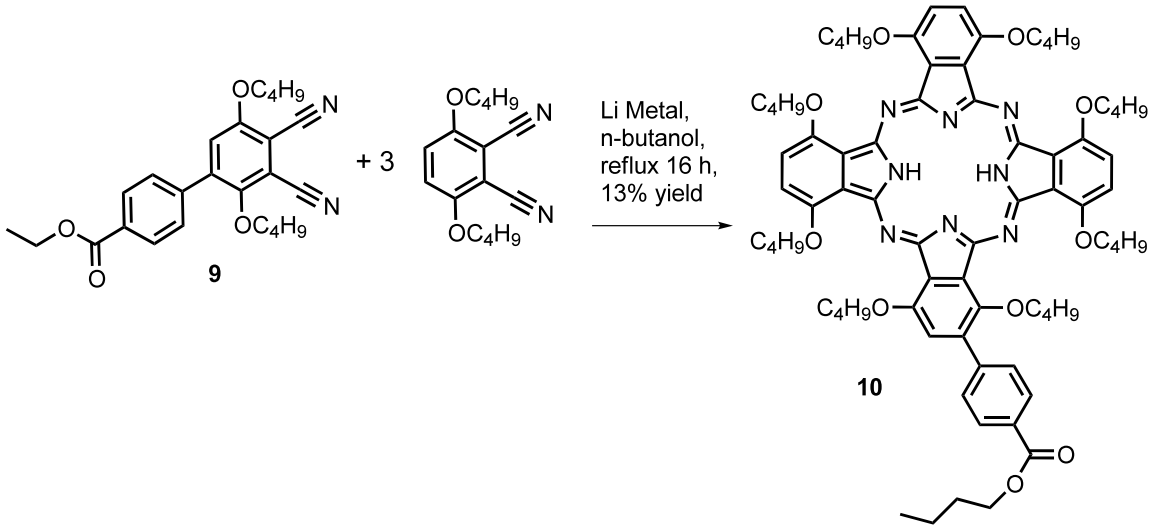

Scheme 3: Synthetic step to obtain compound **10**.

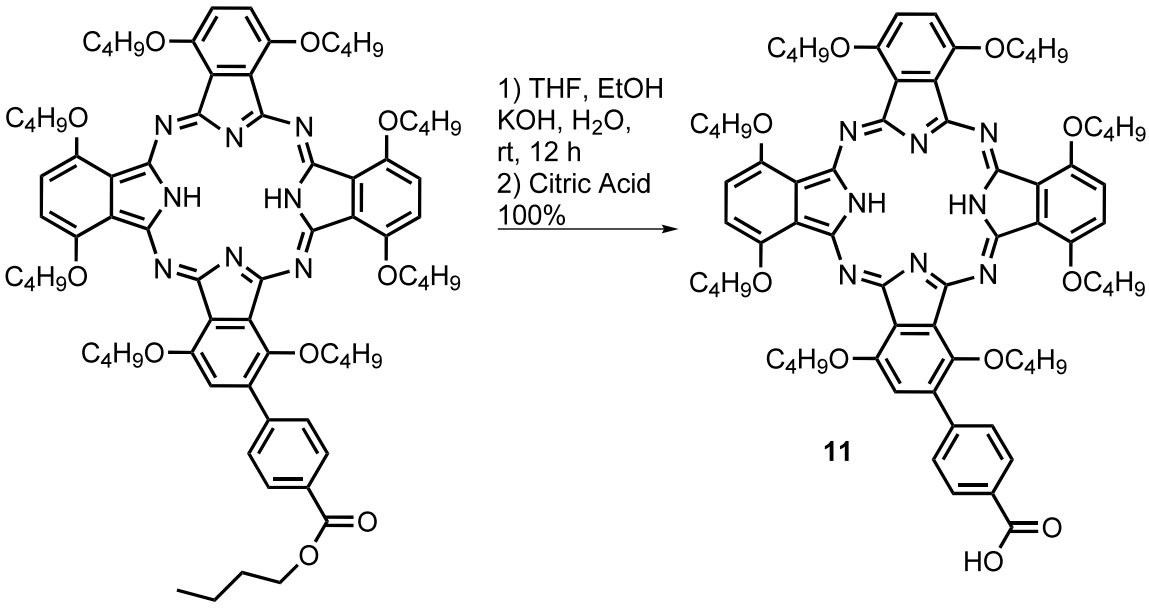

Scheme 4: Synthetic step to obtain compound **11**.

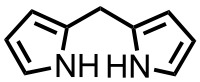

Di(1*H*-pyrrol-2-yl)methane (1): Followed reference [266]

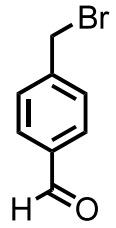

4-(Bromomethyl)benzaldehyde (2): This preparation followed a previously published procedure [268]. A 500 ml round bottom flask was charged with α-bromo-*p*-tolunitrile (5 g, 25.5 mmol) and freshly distilled toluene (50 ml). The solution was cooled to 0 ^{o}C and degassed with nitrogen for 15 min. To this was added dropwise a 1 M in hexane DIBAL-H solution (32 ml, 35 mmol) and allowed to react for 1 h at 0 ^{o}C. To this was added chloroform (~80 ml) followed by the addition of a 10% hydrochloric acid solution (~150 ml), the mixture was allowed to stir at room temperature for an additional 1 h. The organic layer was washed with deionized (DI) water, dried over sodium sulfate and evaporated under reduced pressure. This crude solid was filtered, washed with cold hexane and dried under high vacuum to afford a white solid. Yield: 4.02 g (89.7%). ^{1}H NMR (400 MHz; $CDCl_3$; 0.03% Me_4Si): δ_H, ppm 4.50 (2H, s, CH_2), 7.54 (2H, d, Ar), 7.85 (2H, d, Ar), 10.03 (1H, s, CHO)

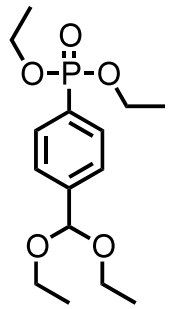

Diethyl (4-(diethoxymethyl)phenyl)phosphonate (3): Into a dry 50 ml round bottom flask was added 1-bromo-4-(diethoxymethyl)benzene (3.00 g, 11.6 mmol), diethylphosphite (1.92 g, 13.9 mmol), dry toluene (5 ml) and dry triethylamine (5 ml) and this solution was degassed with argon for 20 min. To this was added tetrakis(triphenylphosphine)palladium(0) (134 mg, 10 mol%) and allowed to react at 80 ^{o}C for 24 h. The solution was evaporated under reduced pressure and the crude solid extracted with dichloromethane, which was washed with DI water, dried over sodium sulfate and concentrated. This was then subjected to column chromatography using silica gel and ethyl acetate/dichloromethane (70:30) to afford slight yellow oil. Yield: 1.91 g (52%). ^{1}H NMR (400 MHz; $CDCl_3$; 0.03% Me_4Si): δ_H, ppm 7.98 (m, 1H) ppm 7.68 (m, 1H) ppm 7.55 (m, 1H) ppm 7.49 (m, 1H) ppm 5.95 (s, 1H) ppm 4.15 (m, 4H) ppm 3.72 (m, 4H) ppm 1.36 (t, 6H, J=7.1Hz) ppm 1.24 (t, 6H, J=7.2Hz)

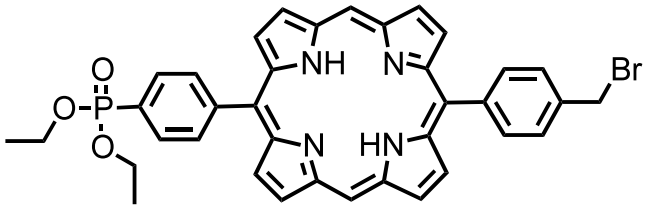

5-(4-Diethyl phenylphosphonate)-10-(4-bromomethylphenyl)porphyrin (4): Into a 1000 ml round bottom flask was placed meso-free dipyrromethane **(1)** (1.5 g, 0.01 mol), diethyl (4-(diethoxymethyl)phenyl)phosphonate **(3)** (1.58 g, 5 mmol), 4-(bromomethyl)benzaldehyde **(2)** (1.0 g, 5 mmol) along with chloroform (760 ml) stabilized with 0.75% ethanol, this solution was degassed with argon for 25 min at room temperature. To this was added boron trifluoride diethyl etherate in chloroform solution (315 μl in 1 ml of chloroform) and allowed to react for 3 h at room temperature. To this was added 2,3-dichloro-5,6-dicyano-1,4-benzoquinone (2.5 g) and allowed to react for 2 h at room temperature. The solution was dried down under reduced pressure and re re-suspended in dichloromethane, which was washed with DI water, dried over sodium sulfate and concentrated. The crude mixture was passed through a pad of silica gel using dichloromethane (100%) slowly changing to acetone/dichloromethane (10:90) as eluent. The porphyrin mixture was subjected to column chromatography using silica gel and dichloromethane/acetone (93:7) to afford a purple solid. Yield 0.334 g (9.7%) ^{1}H NMR (400 MHz; $CDCl_3$; 0.03% Me_4Si): δ_H, ppm 10.35 (s, 2H) ppm 9.42 (dd, 4H, J=2.6Hz, J=4.6Hz) ppm 9.09 (d, 2H, J=4.6Hz) ppm 9.04 (d, 2H, J=4.6Hz) ppm 8.40 (m, 2H,) ppm 8.26 (dd, 4H, J=6.6Hz, J=14.5Hz) ppm 7.85 (d, 2H, J=8.0Hz) ppm 4.89 (s, 2H) ppm 4.41 (m, 4H,) ppm 1.55 (t, 6H, J=7.1Hz) ppm -3.29 (s, 2H). MS (MALDI-TOF): *m/z* calcd. for $C_{37}H_{32}BrN_4O_3P$ 691.55, obsd. 691.55.

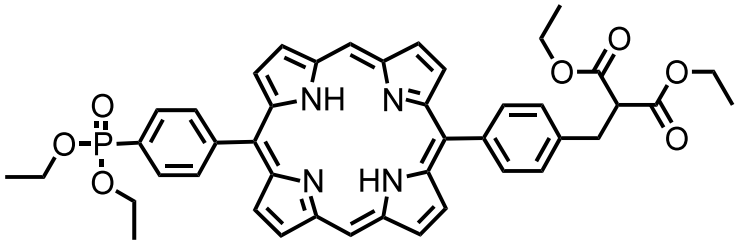

5-(4-Diethyl phenylphosphonate)-10-(diethyl 2-(benzylmalonate)porphyrin (5): Into two double necked round bottom flacks was placed freshly distilled dry tetrahydrofuran (15 ml), cooled to 0 ^{o}C and degassed with argon for 15 min. Into one flask was added sodium hydride (13.3 mg, 0.552 mmol) and allowed to stir for 10 min, followed by the dropwise addition of diethylmalonate (73.6 mg, 0.460 mmol) and this was allowed to react for 45 min and 0 ^{o}C. Into the other flask was place 5-(4-diethyl phenylphosphonate)-10-(4-bromomethylphenyl)porphyrin **(4)** (100 mg, 0.144 mmol) and further degassed with argon while maintaining 0 ^{o}C. The contents of the flasks were combined into one by cannula transfer and allowed to react for 1.5 h while slowly warming to room temperature. The reaction mixture was poored into an ice-cold saturated ammonium chloride solution for ~ 1 min, then extracted with dichloromethane. The organic layer was washed with DI water, dried over sodium sulfate and evaporated under reduced pressure. The crude solid was subjected to column chromatography using silica gel and dichloromethane/acetone (90:10) as eluent to afford a purple solid. Yield 62 mg (56%), ^{1}H NMR (400 MHz; $CDCl_3$; 0.03% Me_4Si): δ_H, ppm 9.41 (dd, 4H, J=4.7Hz, J=7.0Hz) ppm 9.05 (dd, 4H, J=4.6Hz, J=11.4Hz) ppm 8.40 (dd, 2H, J=4.0Hz, J=8.0Hz) ppm 8.27 (dd, 2H, J=8.0Hz, J=13.1Hz) ppm 8.19 (d, 2H, J=7.9Hz) ppm 7.67 (d, 2H, J=7.9Hz) ppm 4.38 (m, 8H,) ppm 4.00 (t, 1H, J=7.9Hz) ppm 3.61 (d, 2H, J=7.8Hz) ppm

1.55 (t, 6H, J=7.1Hz) ppm 1.39 (t, 6H, J=7.1Hz) ppm -3.13 (s, 2H). MS (MALDI-TOF): *m/z* calcd. for $C_{44}H_{43}N_4O_7P$ 770.81, obsd. 770.80.

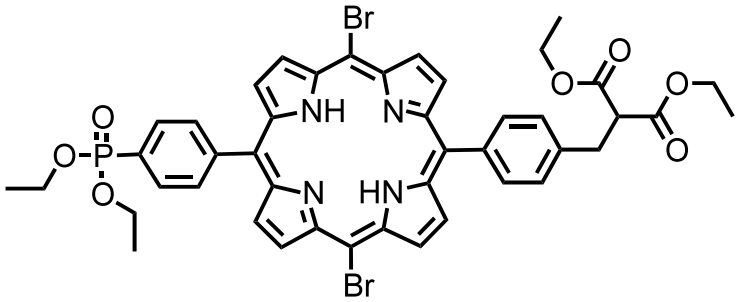

5,15-Dibromo-10-(4-diethyl phenylphosphonate)-20-(diethyl 2-(benzylmalonate)porphyrin (6): Into a 100 ml round bottom flask was placed 5-(4-diethyl phenylphosphonate)-10-(diethyl 2-(benzylmalonate)porphyrin **(5)** (62 mg, 0.080 mmol), chloroform (30 ml), pyridine (0.1 ml) and solution was cooled to 0 ^{o}C. To this was added *N*-bromosuccinimide (27 mg, 0.152 mmol) and the mixture was allowed to react for 10 min. Acetone (5 ml) was added to quench the reaction and the mixture was evaporated under reduced pressure. The crude solid was purified via column chromatography using silica gel and dichloromethane/acetone (95:5) as eluent to afford a purple/brown solid. Yield 73.7 mg (99%) ^{1}H NMR (400 MHz; $CDCl_3$; 0.03% Me_4Si): δ_H, ppm 9.62 (dd, 4H, J=5.0Hz, J=6.9Hz) ppm 8.79 (dd, 4H, J=4.5Hz, J=13.9Hz) ppm 8.25 (m, 4H) ppm 8.07 (d, 2H, J=8.0Hz) ppm 7.63 (d, 2H, J=8.0Hz) ppm 4.39 (m, 8H) ppm 3.99 (t, 1H, J=7.8Hz) ppm 3.60 (d, 2H, J=7.8Hz) ppm 1.55 (t, 6H, J=7.1Hz) ppm 1.39 (t, 6H, J=7.1Hz) ppm -2.75 (s, 2H). MS (MALDI-TOF): *m/z* calcd. for $C_{44}H_{41}Br_2N_4O_7P$ 928.60, obsd. 927.96.

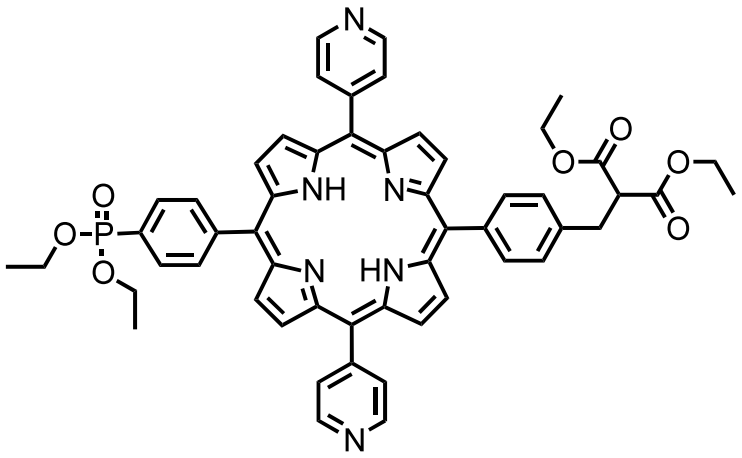

5,15-Bis(4-pyridyl)-10-(4-diethyl phenylphosphonate)-20-(diethyl 2-(benzylmalonate)porphyrin (7): Into a 100 ml round bottom flask was placed 5,15-dibromo-10-(4-diethyl phenylphosphonate)-20-(diethyl 2-(benzylmalonate)porphyrin **(6)** (73.7 mg, 0.0737 mmol), 4-pyridineboronic acid pinacol ester (325 mg, 1.58 mmol), potassium phosphate (673 mg, 3.17 mmol), and dioxane (40 ml). The resulting solution was degassed for 20 min with argon. To this was added tetrakis-(triphenylphosphine) palladium (0) (18.3 mg, 0.0159 mmol) and was allowed to stir at 70 ^{o}C for 42 h. After cooling to room temperature the crude mixture was filtered and the solid was washed with dichloromethane and organics were evaporated under reduced pressure. The crude solid was purified via silica gel column chromatography using dichloromethane/methanol (91:9) as eluent to afford a purple solid. Yield 68 mg (93%) ^{1}H NMR (400 MHz; $CDCl_3$; 0.03% Me_4Si): δ_H, ppm 9.05 (d, 4H, J=5.9Hz) ppm 8.84 (m, 8H) ppm 8.32 (dd, 2H, J=4.0Hz, J=8.2Hz) ppm 8.23 (dd, 2H, J=8.2Hz, J=13.1Hz) ppm 8.16 (d, 4H, J=5.9Hz) ppm 8.12 (d, 2H, J=8.0Hz) ppm 7.62 (d, 2H, J=8.0Hz) ppm 4.37 (m, 8H) ppm 3.97 (t, 1H, J=7.8Hz) ppm 3.58 (d, 2H, J=7.8Hz) ppm 1.53 (t, 6H, J=7.1Hz) ppm 1.36 (t, 6H,

J=7.1Hz) ppm -2.87 (s, 2H). MS (MALDI-TOF): *m/z* calcd. for $C_{54}H_{49}N_6O_7P$ 924.98, obsd. 924.54.

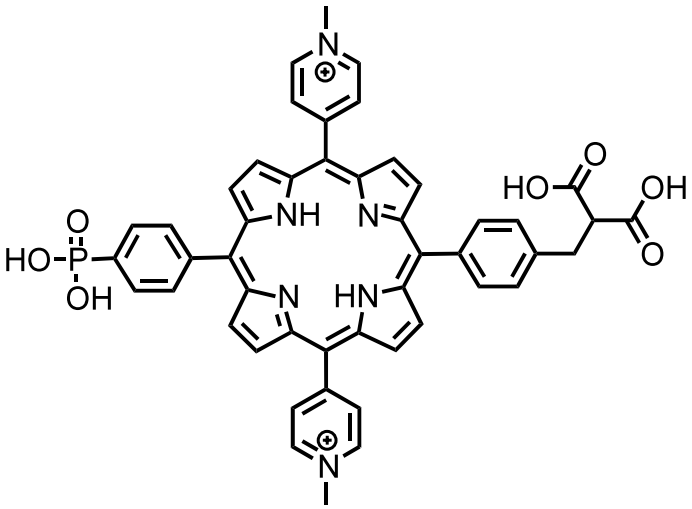

5,15-Bis(N-Methyl-4-pyridyl)-10-(4-phenylphosphonic acid)-20-(2-(benzylmalonic acid)porphyrin (8): (Methylation was done following previously published work [269]. Into a 50 ml round bottom flask was placed dimethylformamide (5 ml), 5,15-bis(4-pyridyl)-10-(4-diethyl phenylphosphonate)-20-(diethyl 2-(benzylmalonate)porphyrin **(7)** (16 mg, 0.0173 mmol) and the solution was degassed with argon for 10 min. To this was added 4 drops of methyl iodide and stirred at room temperature for 24 h. After this time MALDI-TOF mass spectrum was obtained which showed mono and di methylated porphyrin. Therefore, 4 more drops of methyl iodide were added and the solution was stirred at 55 ^{o}C for another 24 h. After this the mass spectrum showed one peak for the dimethylated porphyrin. The solution was evaporated to dryness under reduced pressure to afford a purple solid. Yield 16.5 mg (100%). NMR was attempted in D_6-DMSO to show inner pyrrole protons at ppm -2.99, the rest of the spectrum was broad due to low solubility. This porphyrin (16.5 mg 0.0173 mmol) was dissolved in tetrahydrofuran (10 ml), ethanol (4 ml), and DI water (2 ml). To this was added potassium hydroxide (9.7 mg, 0.173 mmol) and the resulting solution was allowed to stir at room temperature for 48 h. After which, citric acid was added until the solution was slightly acidic (by litmus paper)

then the solution was evaporated under reduced pressure. MS (MALDI-TOF): *m/z* calcd. for $C_{48}H_{39}N_6O_7P$ 842.8319, obsd. 842.833.

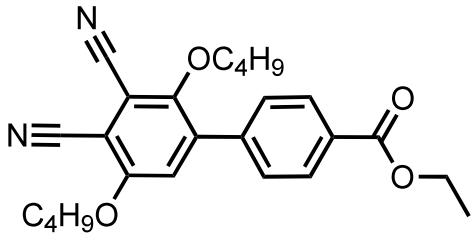

Ethyl 2',5'-dibutoxy-3',4'-dicyanobiphenyl-4-carboxylate (9). A mixture of 4,5-dibromo-3,6-dibutoxyphthalonitrile and 4-bromo-3,6-dibutoxyphthalonitrile (0.50 g, 1.2 mmol) (prepared following previously published procedure [267] was placed into a two neck round bottom flask along with 150 mL of freshly distilled tetrahydrofuran. To this was added potassium carbonate (3.32 g, 24 mmol) and 4-(ethoxycarbonyl)phenylboronic acid (2.25 g, 12 mmol) and the solution was degassed with argon for 15 min. After degassing, tetrakis(triphenylphospine)palladium (0) (0.28 g, 0.24 mmol) was added and the solution heated to 50 ^{0}C and stirred for 24 h under argon. The solvent was removed under reduced pressure and the crude solid was taken up in ethyl acetate and washed twice with water. The organic phase was dried with sodium sulfate and concentrated. The mixture was purified via silica gel column chromatography using 2% ethyl acetate in DCM as eluent. Yield 251 mg (3.2%, percent yield calculated from the starting material 3,6-dihydroxyphthalonitile, see scheme 2). ^{1}H-NMR (500 MHz; $CDCl_3$; 0.03% Me_4Si) ppm 8.15 (d, 2H, J=8.3Hz) ppm 7.61 (d, 2H, J=8.3Hz) ppm 7.13 (s, 1H) ppm 4.43 (q, 2H, J=7.2Hz) ppm 4.12 (t, 2H, J=6.3Hz) ppm 3.65 (t, 2H, J=6.5Hz) ppm 1.85 (m, 2H) ppm 1.54 (m, 6H) ppm 1.43 (t, 3H, J=7.1Hz) ppm 0.99 (t, 3H, J=7.4Hz) ppm 0.79 (t, 3H, J=7.4Hz)

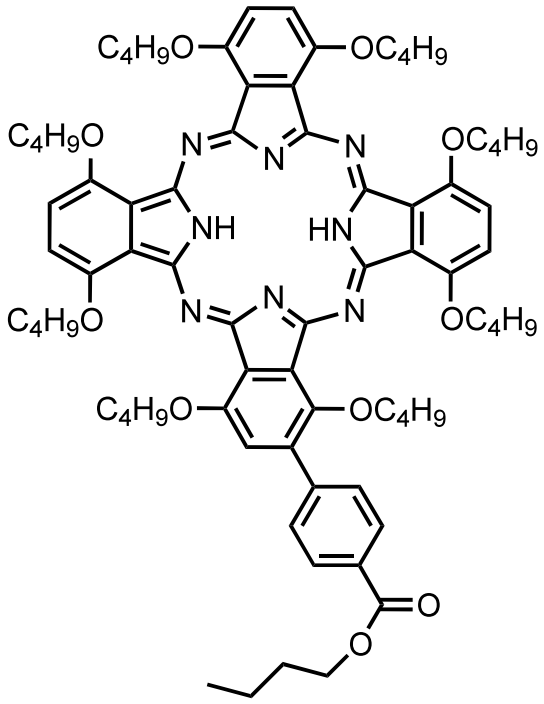

2-(4-Butyl benzoate)-1,4,8,11,15,18,22,25-octabutoxy-29*H*,31*H*-phthalocyanine(10): A portion of ethyl 2',5'-dibutoxy-3',4'-dicyanobiphenyl-4-carboxylate **(9)** (0.251 g, 0.597 mmol) along with 3,6-dibutoxyphthalonitrile (0.348 g, 1.28 mmol) was dissolved in dry n-butanol and the solution was degassed with argon for 10 min. To this was added freshly cut lithium metal (~150 mg) that changed the color of the solution to an intense green, and the reaction mixture was refluxed for 16 h. The solution was allowed to cool to room temperature and a mixture of DCM (~15 ml) and acetic acid (5 ml) was added, this was allowed to stir for 30 min. This was followed by the addition of H_2O (20 ml and the solution was stirred for an additional 30 min. DCM (~100 ml) was added and the organic phase was separated, dried with sodium sulfate and concentrated. The mixture was purified via a number of column chromatography steps using silica gel. First toluene/ethyl acetate (60:40) as eluent was used to isolate the un-substituted free base Pc,

the polar bands from this column were then ran on a second column with toluene/ethyl acetate/acetone/methanol (70:20:5:5) as eluent and the second band was collected. This was passed through a pad of silica gel with 2% ethyl acetate in DCM to remove blue fluorescent impurities. This mixture of Pc was then finally purified using toluene/ethyl acetate/acetone (70:20:10) as eluent to afford a green solid. Yield 100.3 mg (13%) ^{1}H-NMR (400 MHz; $CDCl_3$; 0.03% Me_4Si) ppm 8.34 (d, 2H, J=8.2Hz) ppm 8.15 (d, 2H, J=8.2Hz) ppm 7.64 (d, 2H, J=3.0Hz) ppm 7.62 (d, 2H, J=2.5Hz) ppm 7.60 (s, 1H) ppm 7.59 (d, 2H, J=2.9Hz) ppm 4.86 (m, 16H) ppm 4.72 (t, 2H, J=7.4Hz) ppm 2.40 (td, 2H, J=7.5Hz, J=15.2Hz) ppm 2.23 (m, 16H) ppm 1.67 (m, 16H) ppm 1.45 (m, 2H) ppm 1.21 (t, 3H, J=7.4Hz) ppm 1.09 (m, 21H) ppm 0.57 (t, 3H, J=7.3Hz). MS (MALDI-TOF): *m/z* calcd. for $C_{75}H_{94}N_8O_{10}$ 1267.60, obsd. 1267.60, 1209.63 (M-butyl).

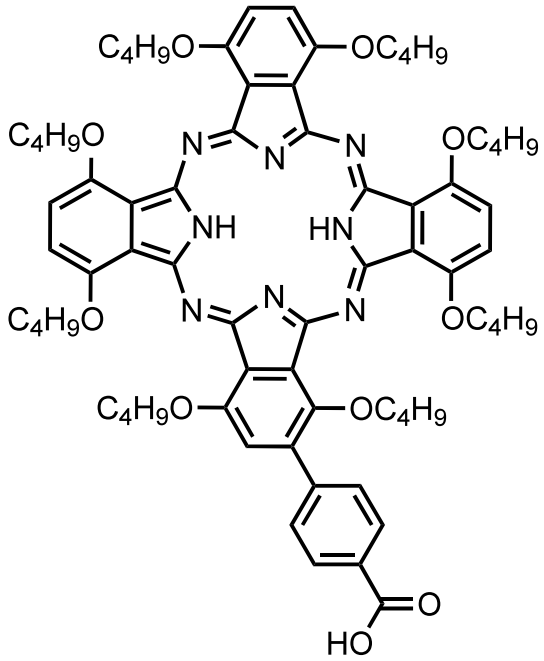

2-(4-Carboxyphenyl)-1,4,8,11,15,18,22,25-octabutoxy-29*H*,31*H*-phthalocyanine(11): A portion of 2-(4-butyl benzoate)-1,4,8,11,15,18,22,25-octabutoxy-29*H*,31*H*-phthalocyanine **11** (10 mg, 0.0078 mmol) was placed into a 10 ml round bottom flask along with potassium hydroxide (10 mg, 0.18 mmol), tetrahydrofuran (5 ml), water (1 ml) and ethanol (2 ml) and the solution was allowed to stir overnight at room temperature. After which the solution was evaporated under reduced pressure and crude solid taken up with dichloromethane and water. This solution was acidified with citric acid (3 mg) and extracted with dichloromethane to yield a green solid. Yield 9.5 mg (100%) MS (MALDI-TOF): *m/z* calcd. for $C_{71}H_{86}N_8O_{10}$ 1211.49, obsd. 1212.37 (M+H)

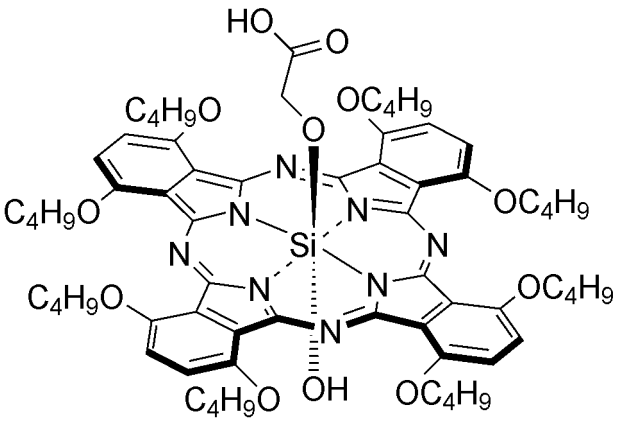

2-(Oxyacetic acid)hydroxy-1,4,8,11,15,18,22,25-octabutoxyphthalocyaninatosilicon(IV) (12). A portion of $SiPc(OH)_2$ (30 mg, 0.026 mmol) was dissolved in dry pyridine and the solution was degassed for 5 min with argon. Glycolic acid (9.8 mg, 0.13 mmol) was added and the resulting solution was stirred at 55 ^oC, under argon for 3 days. The pyridine was evaporated under reduced pressure and the resulting residue was taken up in DCM and washed with DI H_2O (20 mL). The organic phase was dried over sodium sulfate and evaporated under reduced pressure. Column chromatography was done using silica gel in two purification steps; first, toluene/ethyl acetate/methanol (60:38:2) was used as eluent followed by a second column using chloroform/ethyl acetate/methanol (78:20:2) as eluent, which afforded a green solid. Yield 7 mg (22%), ^{1}H-NMR (400 MHz; $CDCl_3$; 0.03% Me_4Si): δ_H, ppm 7.63 (s, 8H, Pc-H) ppm 4.86 (t, 16H, -C*H*$_2$-CH_2-CH_2-CH_3, J=7.4Hz) ppm 2.20 (p, 16H, -CH_2-C*H*$_2$-CH_2-CH_3) ppm 1.66 (sex, 16H, -CH_2-CH_2-C*H*$_2$-CH_3) ppm 1.08 (t, 24H, -CH_2-CH_2-CH_2-C*H*$_3$) ppm -1.40 (s, 2H, CH_2-Glycolic). MS (MALDI-TOF): *m/z* calcd. for $C_{66}H_{84}N_8O_{12}Si$ 1209.50, obsd. 1209.49, 1149.58 (M-Glycolic).

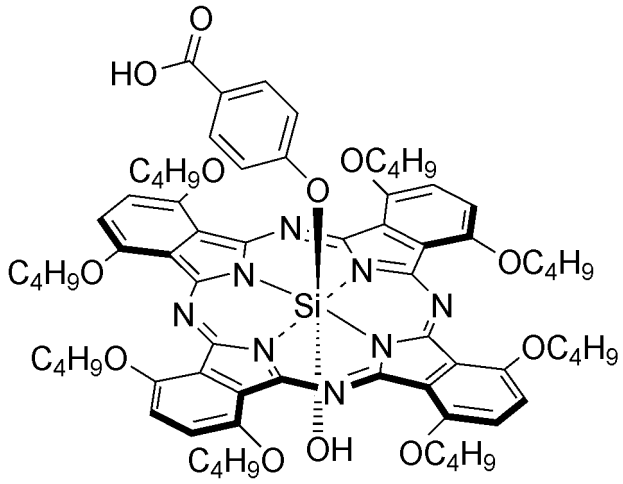

4-(Carboxyphenyl)phenolatehydroxy-1,4,8,11,15,18,22,25-octabutoxyphthalocyaninatosilicon(IV) (13): Into a dry 10 ml round bottom flask was placed $SiPc(OH)_2$ (20 mg, 0.0174 mmol), 4-hydroxybenzoic acid (12 mg, 0.0869 mmol), dry dichloromethane (4 ml), and pyridine (4 drops). This solution was allowed to stir at room temperature for 4 days. The solution was evaporated under reduced pressure and the crude solid was washed with DI water, dried with sodium sulfate and concentrated. The crude product was purified via silica gel column chromatography using toluene/ethyl acetate (65:35) as eluent to afford a green solid. Yield 5.3 mg (24%). ^{1}H-NMR (400 MHz; $CDCl_3$; 0.03% Me_4Si): δ_H, ppm 7.63 (s, 8H) ppm 6.40 (d, 2H, J=8.8Hz) ppm 4.78 (m, 16H) ppm 2.86 (d, 2H, J=8.8Hz) ppm 2.14 (p, 16H) ppm 1.63 (sex, 16H) ppm 1.04 (t, 24H, J=7.4Hz). MS (MALDI-TOF): *m/z* calcd. for $C_{71}H_{86}N_8O_{12}Si$ 1271.57, obsd. 1272.43 (M+H), 1149.58 (M-benzoic).

CHAPTER 6

CONCLUSIONS

This dissertation has provided a discussion on some of the latest advancements in our group for the synthesis and application of porphyrin, phthalocyanine and perylene chromophores for solar energy conversion. While the studies presented within this dissertation are steps in the right direction for the production of a system capable of solar energy conversion that leads to producing a fuel such as hydrogen, there is still much room for improvement. This includes studying and fine-tuning the appropriate steps of assembling all of the individual components into the final dual-threshold photoelectrochemical cell. Studies have demonstrated that high potential palladium porphyrins can drive the iridium oxide catalyst electrochemically, although for use in a photocell one will need to use non-heavy metal porphyrins due to their tendency for phosphorescence from the triplet state. A series of phthalocyanines have been synthesized and studied in Grätzel type photocells and have demonstrated good photocurrents. The controlling of both redox potential and the absorption properties of phthalocyanines by particular functional groups have been utilized to produce near IR absorbing dyes for use in the dual-threshold photoelectrochemical cell. The synthesis of multiple perylene dyes for electron transfer studies within TiO_2 assemblies have yielded insights into the energetic properties of nano-particulate TiO_2 vs bulk TiO_2 which could have impacts for the topic of semi-conductors used in the construction of dye sensitized solar cells.

This dissertation has outlined a variety of projects ranging from synthesis to electrochemical and photochemical measurements, with the common theme being organic synthetic chemistry. Future work will likely focus on fine tuning the individual

components as well as, finding the appropriate steps for assembling the final dual-threshold photoelectrochemical cell.

REFERENCES

(1) Barber, J. Photosystem II: an enzyme of global significance. *Biochem. Soc. Trans.* **2006**, *34*, 619–631.

(2) Kalyanasundaram, K.; Graetzel, M. Artificial photosynthesis: biomimetic approaches to solar energy conversion and storage. *Current Opinion in Biotechnology* **2010**, *21*, 298–310.

(3) Blankenship, R. E. *Molecular mechanisms of photosynthesis*; Wiley-Blackwell, 2002.

(4) Gust, D.; Moore, T. A.; Moore, A. L. Molecular mimicry of photosynthetic energy and electron transfer. *Acc. Chem. Res.* **1993**, *26*, 198–205.

(5) Sauer, K. Photosynthetic membranes. *Acc. Chem. Res.* **1978**, *11*, 257–264.

(6) Cogdell, R. J.; Frank, H. A. How carotenoids function in photosynthetic bacteria. *Biochim. Biophys. Acta* **1987**, *895*, 63–79.

(7) Kirmaier, C.; Holten, D. Primary photochemistry of reaction centers from the photosynthetic purple bacteria. *Photosyn. Res.* **1987**, *13*, 225–260.

(8) McEvoy, J. P.; Brudvig, G. W. Structure-based mechanism of photosynthetic water oxidation. *Phys. Chem. Chem. Phys.* **2004**, *6*, 4754.

(9) RAPPAPORT, F.; DINER, B. Primary photochemistry and energetics leading to the oxidation of the (Mn)4Ca cluster and to the evolution of molecular oxygen in Photosystem II. *Coordination Chemistry Reviews* **2008**, *252*, 259–272.

(10) Barber, J. Photosynthetic reaction centres: a common link. *Trends in Biochemical Sciences* **1987**, *12*, 321–326.

(11) Michel, H.; Deisenhofer, J. Relevance of the photosynthetic reaction center from purple bacteria to the structure of photosystem II. *Biochemistry* **1988**, *27*, 1–7.

(12) Umena, Y.; Kawakami, K.; Shen, J.-R.; Kamiya, N. Crystal structure of oxygen-evolving photosystem II at a resolution of 1.9 Å. *Nature* **2011**, *473*, 55–60.

(13) Lubitz, W.; Isaacson, R. A.; Okamura, M. Y.; Abresch, E. C.; Plato, M.; Feher, G. ENDOR studies of the intermediate electron acceptor radical anion I-. in Photosystem II reaction centers. *Biochim. Biophys. Acta* **1989**, *977*, 227–232.

(14) Nabedryk, E.; Andrianambinintsoa, S.; Berger, G.; Leonhard, M.; Mäntele, W.; Breton, J. Characterization of bonding interactions of the intermediary electron acceptor in the reaction center of Photosystem II by FTIR spectroscopy. *Biochimica et Biophysica Acta (BBA) - Bioenergetics* **1990**, *1016*, 49–54.

(15) Tetenkin, V. L.; Gulyaev, B. A.; Seibert, M.; Rubin, A. B. Spectral properties of stabilized D1/D2/cytochrome b-559 photosystem II reaction center complex Effects of Triton X-100, the redox state of pheophytin, and β-carotene. *FEBS Letters* **1989**, *250*, 459–463.

(16) Rutherford, A. W.; Stevens, S. E.; Bryant, D. A. Light Energy Transduction in Photosynthesis: Higher Plant and Bacterial Models. *The American Society of Plant Physiologists* **1988**, 163–177.

(17) Groot, M. L.; Pawlowicz, N. P.; van Wilderen, L. J. G. W.; Breton, J.; van Stokkum, I. H. M.; van Grondelle, R. Initial electron donor and acceptor in isolated Photosystem II reaction centers identified with femtosecond mid-IR spectroscopy. *Proceedings of the National Academy of Sciences* **2005**, *102*, 13087–13092.

(18) Holzwarth, A. R.; Müller, M. G.; Reus, M.; Nowaczyk, M.; Sander, J.; Rögner, M. Kinetics and mechanism of electron transfer in intact photosystem II and in the isolated reaction center: pheophytin is the primary electron acceptor. *Proceedings of the National Academy of Sciences* **2006**, *103*, 6895–6900.

(19) Kok, B.; Forbush, B.; McGloin, M. Cooperation of charges in photosynthetic O2 evolution-I. A linear four step mechanism. *Photochem. Photobiol.* **1970**, *11*, 457–475.

(20) FORBUSH, B.; KOK, B.; McGLOIN, M. P. COOPERATION OF CHARGES IN PHOTOSYNTHETIC O 2EVOLUTION-II. DAMPING OF FLASH YIELD OSCILLATION, DEACTIVATION. *Photochem. Photobiol.* **1971**, *14*, 307–321.

(21) Blankenship, R. E.; Tiede, D. M.; Barber, J.; Brudvig, G. W.; Fleming, G.; Ghirardi, M.; Gunner, M. R.; Junge, W.; Kramer, D. M.; Melis, A.; Moore, T. A.; Moser, C. C.; Nocera, D. G.; Nozik, A. J.; Ort, D. R.; Parson, W. W.; Prince, R. C.; Sayre, R. T. Comparing Photosynthetic and Photovoltaic Efficiencies and Recognizing the Potential for Improvement. *Science* **2011**, *332*, 805–809.

(22) Hoppe, H.; Sariciftci, N. S. Organic solar cells: An overview. *Journal of Materials Research* **2004**, *19*, 1924–1945.

(23) Solomon, S.; Qin, D.; Manning, M.; Chen, Z. Climate change 2007: Synthesis

Report. Contribution of Working Group I, II and III to the Fourth Assessment Report of the Intergovernmental Panel on Climate Change …. ... *Group I* **2007**.

(24) Sherman, B. D.; Vaughn, M. D.; Bergkamp, J. J.; Gust, D.; Moore, A. L.; Moore, T. A. Evolution of reaction center mimics to systems capable of generating solar fuel. *Photosyn. Res.* **2013**, 1–12.

(25) Lewis, N. S.; Nocera, D. G. Powering the planet: chemical challenges in solar energy utilization. *Proceedings of the National Academy of Sciences* **2006**, *103*, 15729–15735.

(26) Grätzel, M. Photoelectrochemical cells. *Nature* **2001**, *414*, 338–344.

(27) Grätzel, M. Dye-sensitized solar cells. *Journal of Photochemistry and Photobiology C: Photochemistry Reviews* **2003**, *4*, 145–153.

(28) Hagfeldt, A.; Grätzel, M. Molecular Photovoltaics. *Acc. Chem. Res.* **2000**, *33*, 269–277.

(29) Barbé, C. J.; Arendse, F.; Comte, P.; Jirousek, M.; Lenzmann, F.; Shklover, V.; Grätzel, M. Nanocrystalline Titanium Oxide Electrodes for Photovoltaic Applications. *Journal of the American Ceramic Society* **2005**, *80*, 3157–3171.

(30) Vinodgopal, K.; Bedja, I.; Kamat, P. V. Nanostructured Semiconductor Films for Photocatalysis. Photoelectrochemical Behavior of SnO 2/TiO 2Composite Systems and Its Role in Photocatalytic Degradation of a Textile Azo Dye. *Chem. Mater.* **1996**, *8*, 2180–2187.

(31) Subramanian, V.; Wolf, E.; Kamat, P. V. Semiconductor−Metal Composite Nanostructures. To What Extent Do Metal Nanoparticles Improve the Photocatalytic Activity of TiO 2Films? *J Phys Chem B* **2001**, *105*, 11439–11446.

(32) Youngblood, W. J.; Lee, S.-H. A.; Maeda, K.; Mallouk, T. E. Visible Light Water Splitting Using Dye-Sensitized Oxide Semiconductors. *Acc. Chem. Res.* **2009**, *42*, 1966–1973.

(33) Youngblood, W. J.; Lee, S.-H. A.; Kobayashi, Y.; Hernandez-Pagan, E. A.; Hoertz, P. G.; Moore, T. A.; Moore, A. L.; Gust, D.; Mallouk, T. E. Photoassisted Overall Water Splitting in a Visible Light-Absorbing Dye-Sensitized Photoelectrochemical Cell. *J. Am. Chem. Soc.* **2009**, *131*, 926–927.

(34) Sherman, B. D.; Pillai, S.; Kodis, G.; Bergkamp, J.; Mallouk, T. E.; Gust, D.; Moore, T. A.; Moore, A. L. A porphyrin-stabilized iridium oxide water oxidation catalyst. *Can. J. Chem.* **2011**, *89*, 152–157.

(35) Moore, G. F.; Blakemore, J. D.; Milot, R. L.; Hull, J. F.; Song, H.-E.; Cai, L.; Schmuttenmaer, C. A.; Crabtree, R. H.; Brudvig, G. W. A visible light water-splitting cell with a photoanode formed by codeposition of a high-potential porphyrin and an iridium water-oxidation catalyst. *Energy Environ. Sci.* **2011**, *4*, 2389.

(36) Bergkamp, J. J.; Sherman, B. D.; Mariño-Ochoa, E.; Palacios, R. E.; Cosa, G.; Moore, T. A.; Gust, D.; Moore, A. L. Synthesis and characterization of silicon phthalocyanines bearing axial phenoxyl groups for attachment to semiconducting metal oxides. *J. Porphyrins Phthalocyanines* **2011**, *15*, 943–950.

(37) Feldt, S. M.; Wang, G.; Boschloo, G.; Hagfeldt, A. Effects of Driving Forces for Recombination and Regeneration on the Photovoltaic Performance of Dye-Sensitized Solar Cells using Cobalt Polypyridine Redox Couples. *J. Phys. Chem. C* **2011**, *115*, 21500–21507.

(38) Hoertz, P. G.; Kim, Y.-I.; Youngblood, W. J.; Mallouk, T. E. Bidentate Dicarboxylate Capping Groups and Photosensitizers Control the Size of IrO 2Nanoparticle Catalysts for Water Oxidation †. *J Phys Chem B* **2007**, *111*, 6845–6856.

(39) Nozik, A. J.; Memming, R. Physical chemistry of semiconductor-liquid interfaces. *J. Phys. Chem.* **1996**.

(40) Rockström, J.; Steffen, W.; Noone, K.; Persson, A.; Chapin, F. S.; Lambin, E. F.; Lenton, T. M.; Scheffer, M.; Folke, C.; Schellnhuber, H. J.; Nykvist, B.; de Wit, C. A.; Hughes, T.; van der Leeuw, S.; Rodhe, H.; Sörlin, S.; Snyder, P. K.; Costanza, R.; Svedin, U.; Falkenmark, M.; Karlberg, L.; Corell, R. W.; Fabry, V. J.; Hansen, J.; Walker, B.; Liverman, D.; Richardson, K.; Crutzen, P.; Foley, J. A. A safe operating space for humanity. *Nature* **2009**, *461*, 472–475.

(41) Armaroli, N.; Balzani, V. The future of energy supply: Challenges and opportunities. *Angew. Chem. Int. Ed. Engl.* **2007**, *46*, 52–66.

(42) Gust, D.; Moore, T. A.; Moore, A. L. Solar Fuels via Artificial Photosynthesis. *Acc. Chem. Res.* **2009**, *42*, 1890–1898.

(43) Bard, A. J.; Fox, M. A. Artificial Photosynthesis: Solar Splitting of Water to Hydrogen and Oxygen. *Acc. Chem. Res.* **1995**, *28*, 141–145.

(44) Sorensen, B. S. *Renewable energy, fourth edition: physics, engineering, environmental impacts, economics & planning*; Academic Press, 2010.

(45) Ito, A. A historical meta-analysis of global terrestrial net primary productivity:

are estimates converging? *Global Change Biol* **2011**, *17*, 3161–3175.

(46) Archer, M. D.; Barber, J. *Molecular to Global Photosynthesis*; Imperial College Press, 2004.

(47) Cramer, W.; Kicklighter, D. W.; Bondeau, A.; Iii, B. M.; Churkina, G.; Nemry, B.; Ruimy, A.; Schloss, A. L.; Intercomparison, T. P. O. T. P. Comparing global models of terrestrial net primary productivity (NPP): overview and key results. *Global Change Biol* **1999**, *5*, 1–15.

(48) Field, C.; Behrenfeld, M.; Randerson, J.; Falkowski, P. Primary production of the biosphere: integrating terrestrial and oceanic components. *Science* **1998**, *281*, 237–240.

(49) Haberl, H.; Erb, K. H.; Krausmann, F.; Gaube, V.; Bondeau, A.; Plutzar, C.; Gingrich, S.; Lucht, W.; Fischer-Kowalski, M. Quantifying and mapping the human appropriation of net primary production in earth's terrestrial ecosystems. *Proceedings of the National Academy of Sciences* **2007**, *104*, 12942–12947.

(50) Barnosky, A. D.; Hadly, E. A.; Bascompte, J.; Berlow, E. L.; Brown, J. H.; Fortelius, M.; Getz, W. M.; Harte, J.; Hastings, A.; Marquet, P. A.; Martinez, N. D.; Mooers, A.; Roopnarine, P.; Vermeij, G.; Williams, J. W.; Gillespie, R.; Kitzes, J.; Marshall, C.; Matzke, N.; Mindell, D. P.; Revilla, E.; Smith, A. B. Approaching a state shift in Earth's biosphere. *Nature* **2012**, *486*, 52–58.

(51) IPCC *Special report on renewable energy sources and climate change mitigation.*; IPCC, Ed. United Kingdom and New York, NY, USA, 2011; pp. 1–1088.

(52) Gust, D.; Moore, T. A. Mimicking photosynthesis. *Science* **1989**, *244*, 35–41.

(53) Moore, T. A.; Gust, D.; Mathis, P.; Mialocq, J. C.; Chachaty, C.; Bensasson, R. V.; Land, E. J.; Doizi, D.; Liddell, P. A.; Lehman, W. R. Photodriven charge separation in a carotenoporphyrin–quinone triad. *Nature* **1984**, *307*, 630–632.

(54) Gust, D.; Moore, T. A.; Liddell, P. A.; Nemeth, G. A.; Makings, L. R.; Moore, A. L.; Barrett, D.; Pessiki, P. J.; Bensasson, R. V. Charge separation in carotenoporphyrin-quinone triads: synthetic, conformational, and fluorescence lifetime studies. *J. Am. Chem. Soc.* **1987**, *109*, 846–856.

(55) Kuciauskas, D.; Liddell, P. A.; Lin, S.; Stone, S. G.; Moore, A. L.; Moore, T. A.; Gust, D. Photoinduced electron transfer in carotenoporphyrin−fullerene triads: temperature and solvent effects. *J Phys Chem B* **2000**, *104*, 4307–4321.

(56) Kodis, G.; Liddell, P. A.; Moore, A. L.; Moore, T. A.; Gust, D. Synthesis and photochemistry of a carotene–porphyrin–fullerene model photosynthetic

reaction center. *Journal of Physical Organic Chemistry* **2004**, *17*, 724–734.

(57) Gust, D.; Moore, T. A.; Moore, A. L.; Gao, F.; Luttrull, D.; DeGraziano, J. M.; Ma, X. C.; Makings, L. R.; Lee, S. J. Long-lived photoinitiated charge separation in carotene-diporphyrin triad molecules. *J. Am. Chem. Soc.* **1991**, *113*, 3638–3649.

(58) Liddell, P. A.; Kuciauskas, D.; Sumida, J. P.; Nash, B.; Nguyen, D.; Moore, A. L.; Moore, T. A.; Gust, D. Photoinduced charge separation and charge recombination to a triplet state in a carotene−porphyrin−fullerene triad. *J. Am. Chem. Soc.* **1997**, *119*, 1400–1405.

(59) Gust, D.; Moore, T. A.; Moore, A. L.; Barrett, D.; Harding, L. O.; Makings, L. R.; Liddell, P. A.; De Schryver, F. C.; Van der Auweraer, M.; et al Photoinitiated charge separation in a carotenoid-porphyrin-diquinone tetrad: enhanced quantum yields via multistep electron transfers. *J. Am. Chem. Soc.* **1988**, *110*, 321–323.

(60) Gust, D.; Moore, T. A.; Moore, A. L.; Makings, L. R.; Seely, G. R.; Ma, X.; Trier, T. T.; Gao, F. A carotenoid-diporphyrin-quinone model for photosynthetic multistep electron and energy transfer. *J. Am. Chem. Soc.* **1988**, *110*, 7567–7569.

(61) Gust, D.; Moore, T. A.; Moore, A. L.; Lee, S. J.; Bittersmann, E.; Luttrull, D. K.; Rehms, A. A.; Degraziano, J. M.; Ma, X. C.; Gao, F.; Belford, R. E.; Trier, T. T. Efficient multistep photoinitiated electron transfer in a molecular pentad. *Science* **1990**, *248*, 199–201.

(62) Gust, D.; Moore, T. A.; Moore, A. L.; Macpherson, A. N.; Lopez, A.; DeGraziano, J. M.; Gouni, I.; Bittersmann, E.; Seely, G. R. Photoinduced electron and energy transfer in molecular pentads. *J. Am. Chem. Soc.* **1993**, *115*, 11141–11152.

(63) Liddell, P. A.; Sumida, J. P.; Macpherson, A. N.; Noss, L.; Seely, G. R.; Clark, K. N.; Moore, A. L.; Moore, T. A.; Gust, D. Preparation and photophysical studies of porphyrin-C60 dyads. *Photochem. Photobiol.* **1994**, *60*, 537–541.

(64) Imahori, H.; Hagiwara, K.; Aoki, M.; Akiyama, T.; Taniguchi, S.; Okada, T.; Shirakawa, M.; Sakata, Y. Linkage and solvent dependence of photoinduced electron transfer in zincporphyrin-C60 dyads. *J. Am. Chem. Soc.* **1996**, *118*, 11771–11782.

(65) Kodis, G.; Liddell, P. A.; la Garza, de, L.; Clausen, P. C.; Lindsey, J. S.; Moore, A. L.; Moore, T. A.; Gust, D. Efficient energy transfer and electron transfer in an artificial photosynthetic antenna−reaction center complex. *J.*

Phys. Chem. A **2002**, *106*, 2036–2048.

(66) Bahr, J.; Kuciauskas, D.; Liddell, P.; Moore, A.; Moore, T.; Gust, D. Driving force and electronic coupling effects on photoinduced electron transfer in a fullerene-based molecular triad. *Photochem. Photobiol.* **2000**, *72*, 598–611.

(67) Steinberg-Yfrach, G.; Liddell, P. A.; Hung, S.-C.; Moore, A. L.; Gust, D.; Moore, T. A. Conversion of light energy to proton potential in liposomes by artificial photosynthetic reaction centres. *Nature* **1997**, *385*, 239–241.

(68) Steinberg-Yfrach, G.; Rigaud, J. L.; Durantini, E. N.; Moore, A. L.; Gust, D.; Moore, T. A. Light-driven production of ATP catalysed by F0F1-ATP synthase in an artificial photosynthetic membrane. *Nature* **1998**, *392*, 479–482.

(69) Kuciauskas, D.; Liddell, P. A.; Lin, S.; Johnson, T. E.; Weghorn, S. J.; Lindsey, J. S.; Moore, A. L.; Moore, T. A.; Gust, D. An Artificial Photosynthetic Antenna-Reaction Center Complex. *J. Am. Chem. Soc.* **1999**, *121*, 8604–8614.

(70) Kodis, G.; Terazono, Y.; Liddell, P. A.; Andréasson, J.; Garg, V.; Hambourger, M.; Moore, T. A.; Moore, A. L.; Gust, D. Energy and photoinduced electron transfer in a wheel-shaped artificial photosynthetic antenna-reaction center complex. *J. Am. Chem. Soc.* **2006**, *128*, 1818–1827.

(71) Terazono, Y.; Kodis, G.; Liddell, P. A.; Garg, V.; Moore, T. A.; Moore, A. L.; Gust, D. Multiantenna Artificial Photosynthetic Reaction Center Complex. *J Phys Chem B* **2009**, *113*, 7147–7155.

(72) Müller, P.; Li, X.-P.; Niyogi, K. K. Non-photochemical quenching. a response to excess light energy. *Plant Physiol.* **2001**, *125*, 1558–1566.

(73) Horton, P.; Ruban, A. V.; Walters, R. G. REGULATION OF LIGHT HARVESTING IN GREEN PLANTS. *Annu. Rev. Plant Physiol. Plant Mol. Biol.* **1996**, *47*, 655–684.

(74) Straight, S. D.; Kodis, G.; Terazono, Y.; Hambourger, M.; Moore, T. A.; Moore, A. L.; Gust, D. Self-regulation of photoinduced electron transfer by a molecular nonlinear transducer. *Nature Nanotech* **2008**, *3*, 280–283.

(75) Seta, P.; Bienvenue, E.; Moore, A. L.; Mathis, P. Photodriven transmembrane charge separation and electron transfer by a carotenoporphyrin–quinone triad. *Nature* **1985**.

(76) Bennett, I. M.; Farfano, H. M. V.; Bogani, F.; Primak, A.; Liddell, P. A.; Otero, L.; Sereno, L.; Silber, J. J.; Moore, A. L.; Moore, T. A.; Gust, D. Active transport of Ca2+ by an artificial photosynthetic membrane. *Nature* **2002**, *420*, 398–401.

(77) Faller, P.; Goussias, C.; Rutherford, A. W.; Un, S. Resolving intermediates in biological proton-coupled electron transfer: a tyrosyl radical prior to proton movement. *Proceedings of the National Academy of Sciences* **2003**, *100*, 8732–8735.

(78) Moore, G. F.; Hambourger, M.; Gervaldo, M.; Poluektov, O. G.; Rajh, T.; Gust, D.; Moore, T. A.; Moore, A. L. A bioinspired construct that mimics the proton coupled electron transfer between P680*+ and the Tyr(Z)-His190 pair of photosystem II. *J. Am. Chem. Soc.* **2008**, *130*, 10466–10467.

(79) Moore, G. F.; Hambourger, M.; Kodis, G.; Michl, W.; Gust, D.; Moore, T. A.; Moore, A. L. Effects of protonation state on a tyrosine-histidine bioinspired redox mediator. *J Phys Chem B* **2010**, *114*, 14450–14457.

(80) Megiatto, J. D.; Antoniuk-Pablant, A.; Sherman, B. D.; Kodis, G.; Gervaldo, M.; Moore, T. A.; Moore, A. L.; Gust, D. Mimicking the electron transfer chain in photosystem II with a molecular triad thermodynamically capable of water oxidation. *Proc. Natl. Acad. Sci. U.S.A.* **2012**, *109*, 15578–15583.

(81) Zhao, Y.; Swierk, J. R.; Megiatto, J. D.; Sherman, B.; Youngblood, W. J.; Qin, D.; Lentz, D. M.; Moore, A. L.; Moore, T. A.; Gust, D.; Mallouk, T. E. Improving the efficiency of water splitting in dye-sensitized solar cells by using a biomimetic electron transfer mediator. *Proceedings of the National Academy of Sciences* **2012**, *109*, 15612–15616.

(82) Wee, T.-L.; Sherman, B. D.; Gust, D.; Moore, A. L.; Moore, T. A.; Liu, Y.; Scaiano, J. C. Photochemical synthesis of a water oxidation catalyst based on cobalt nanostructures. *J. Am. Chem. Soc.* **2011**, *133*, 16742–16745.

(83) Harriman, A.; THOMAS, J. M.; MILWARD, G. R. Catalytic and structural properties of iridium-iridium dioxide colloids. *New J. Chem.* **1987**, *11*, 757–762.

(84) Harriman, A.; Pickering, I. J.; Thomas, J. M.; Christensen, P. A. Metal oxides as heterogeneous catalysts for oxygen evolution under photochemical conditions. *J. Chem. Soc., Faraday Trans. 1* **1988**, *84*, 2795–2806.

(85) Nahor, G. S.; Neta, P.; Hambright, P.; Thompson, A. N., Jr; Harriman, A. Metalloporphyrin-sensitized photooxidation of water to oxygen on the surface of colloidal iridium oxides: photochemical and pulse radiolytic studies. *J. Phys. Chem.* **1989**, *93*, 6181–6187.

(86) Petit, M. A.; Plichon, V. Anodic electrodeposition of iridium oxide films. *Journal of Electroanalytical Chemistry* **1998**, *444*, 247–252.

(87) Yagi, M.; Tomita, E.; Sakita, S.; Kuwabara, T.; Nagai, K. Self-assembly of active IrO2 colloid catalyst on an ITO electrode for efficient electrochemical water oxidation. *J Phys Chem B* **2005**, *109*, 21489–21491.

(88) Kuwabara, T.; Tomita, E.; Sakita, S.; Hasegawa, D.; Sone, K.; Yagi, M. Characterization and Analysis of Self-Assembly of a Highly Active Colloidal Catalyst for Water Oxidation onto Transparent Conducting Oxide Substrates. *J. Phys. Chem. C* **2008**, *112*, 3774–3779.

(89) Nakagawa, T.; Beasley, C. A.; Murray, R. W. Efficient Electro-Oxidation of Water near Its Reversible Potential by a Mesoporous IrO xNanoparticle Film. *J. Phys. Chem. C* **2009**, *113*, 12958–12961.

(90) Nakagawa, T.; Bjorge, N. S.; Murray, R. W. Electrogenerated IrO(x) nanoparticles as dissolved redox catalysts for water oxidation. *J. Am. Chem. Soc.* **2009**, *131*, 15578–15579.

(91) Wen, L.; Li, M.; Schlenoff, J. B. Polyporphyrin Thin Films from the Interfacial Polymerization of Mercaptoporphyrins. *J. Am. Chem. Soc.* **1997**, *119*, 7726–7733.

(92) Yokomatsu, T.; Minowa, T.; Murano, T.; Shibuya, S. Enzymatic desymmetrization of prochiral 2-benzyl-1,3-propanediol derivatives: A practical chemoenzymatic synthesis of novel phosphorylated tyrosine analogues. *Tetrahedron* **1998**, *54*, 9341–9356.

(93) Scalise, I.; Durantini, E. N. Photodynamic effect of metallo 5-(4-carboxyphenyl)-10,15,20-tris(4-methylphenyl) porphyrins in biomimetic AOT reverse micelles containing urease. *Journal of Photochemistry and Photobiology A: Chemistry* **2004**, *162*, 105–113.

(94) Guldi, D. M.; Zilbermann, I.; Anderson, G.; Li, A.; Balbinot, D.; Jux, N.; Hatzimarinaki, M.; Hirsch, A.; Prato, M. Multicomponent redox gradients on photoactive electrode surfaces. *Chem. Commun. (Camb.)* **2004**, 726–727.

(95) Brimblecombe, R.; Koo, A.; Dismukes, G. C.; Swiegers, G. F.; Spiccia, L. Solar Driven Water Oxidation by a Bioinspired Manganese Molecular Catalyst. *J. Am. Chem. Soc.* **2010**, *132*, 2892–2894.

(96) Ranta, J.; Viljanen, R.; Lemmetyinen, H.; Efimov, A. A novel, one-pot method for the synthesis of dimeric and monomeric phthalocyanine silicon complexes from free-base phthalocyanines. *Dyes and Pigments* **2009**, *83*, 317–323.

(97) Aoudia, M.; Cheng, G.; Kennedy, V. O.; Kenney, M. E.; Rodgers, M. A. Synthesis of a series of octabutoxy-and octabutoxybenzophthalocyanines and

photophysical properties of two members of the series. *J. Am. Chem. Soc.* **1997**, *119*, 6029–6039.

(98) Hambourger, M.; Moore, G. F.; Kramer, D. M.; Gust, D.; Moore, A. L.; Moore, T. A. Biology and technology for photochemical fuel production. *Chem. Soc. Rev.* **2009**, *38*, 25–35.

(99) Khaselev, O.; Turner, J. A monolithic photovoltaic-photoelectrochemical device for hydrogen production via water splitting. *Science* **1998**, *280*, 425–427.

(100) Walter, M. G.; Rudine, A. B.; Wamser, C. C. Porphyrins and phthalocyanines in solar photovoltaic cells. *J. Porphyrins Phthalocyanines* **2010**, *14*, 759–792.

(101) Martínez-Díaz, M. V.; la Torre, de, G.; Torres, T. Lighting porphyrins and phthalocyanines for molecular photovoltaics. *Chem. Commun.* **2010**, *46*, 7090.

(102) Muthukumaran, K.; Loewe, R. S.; Ambroise, A.; Tamaru, S.-I.; Li, Q.; Mathur, G.; Bocian, D. F.; Misra, V.; Lindsey, J. S. Porphyrins Bearing Arylphosphonic Acid Tethers for Attachment to Oxide Surfaces. *J. Org. Chem.* **2004**, *69*, 1444–1452.

(103) Loewe, R. S.; Ambroise, A.; Muthukumaran, K.; Padmaja, K.; Lysenko, A. B.; Mathur, G.; Li, Q.; Bocian, D. F.; Misra, V.; Lindsey, J. S. Porphyrins Bearing Mono or Tripodal Benzylphosphonic Acid Tethers for Attachment to Oxide Surfaces. *J. Org. Chem.* **2004**, *69*, 1453–1460.

(104) Hanna, M. C.; Nozik, A. J. Solar conversion efficiency of photovoltaic and photoelectrolysis cells with carrier multiplication absorbers. *J. Appl. Phys.* **2006**, *100*, 074510.

(105) Çoşut, B.; Yeşilot, S.; Durmuş, M.; Kılıç, A.; Ahsen, V. Synthesis and properties of axially-phenoxycyclotriphosphazenyl substituted silicon phthalocyanine. *Polyhedron* **2010**, *29*, 675–682.

(106) O'Regan, B. C.; López-Duarte, I.; Martínez-Díaz, M. V.; Forneli, A.; Albero, J.; Morandeira, A.; Palomares, E.; Torres, T.; Durrant, J. R. Catalysis of Recombination and Its Limitation on Open Circuit Voltage for Dye Sensitized Photovoltaic Cells Using Phthalocyanine Dyes. *J. Am. Chem. Soc.* **2008**, *130*, 2906–2907.

(107) Cook, M. J.; Dunn, A. J.; Daniel, M. F.; Hart, R.; Richardson, R. M.; Roser, S. J. Fabrication of ordered Langmuir-Blodgett multilayers of octa-n-alkoxy phthalocyanines. *Thin Solid Films* **1988**, *159*, 395–404.

(108) Ke, M.-R.; Huang, J.-D.; Weng, S.-M. Comparison between non-peripherally and peripherally tetra-substituted zinc (II) phthalocyanines as photosensitizers: Synthesis, spectroscopic, photochemical and photobiological properties. *Journal of Photochemistry and Photobiology A: Chemistry* **2009**, *201*, 23–31.

(109) Ermilov, E. A.; Tannert, S.; Werncke, T.; Choi, M. T. M.; Ng, D. K. P.; Röder, B. Photoinduced electron and energy transfer in a new porphyrin–phthalocyanine triad. *Chemical Physics* **2006**, *328*, 428–437.

(110) Joyner, R. D.; Cekada, J., Jr; Linck, R. G.; Kenney, M. E. Diphenoxysilicon phthalocyanine. *Journal of Inorganic and Nuclear Chemistry* **1960**, *15*, 387–388.

(111) Belabassi, Y.; Alzghari, S.; Montchamp, J.-L. Revisiting the Hirao cross-coupling: improved synthesis of aryl and heteroaryl phosphonates. *Journal of Organometallic Chemistry* **2008**, *693*, 3171–3178.

(112) Li, Z.; Lieberman, M. Axial Reactivity of Soluble Silicon(IV) Phthalocyanines. *Inorg. Chem.* **2001**, *40*, 932–939.

(113) Huang, J.-D.; Jiang, X.-J.; Shen, X.-M.; Tang, Q.-Q. Synthesis and photobiological properties of novel silicon (IV) phthalocyanines axially modified by paracetamol and 4-hydroxyphenylacetamide. *J. Porphyrins Phthalocyanines* **2009**, *13*, 1227–1232.

(114) Maree, M. D.; Nyokong, T.; Suhling, K.; Phillips, D. Effects of axial ligands on the photophysical properties of silicon octaphenoxyphthalocyanine. *J. Porphyrins Phthalocyanines* **2002**, *6*, 373–376.

(115) Maree, M. D.; Nyokong, T. Synthesis, spectroscopy and electrochemistry of octaphenoxyphthalocyaninato silicon complexes. *J. Porphyrins Phthalocyanines* **2001**, *05*, 555–563.

(116) Leng, X.; Ng, D. K. P. Axial Coordination of Porphyrinatocobalt(II) Complexes with Bis(pyridinolato)silicon(IV) Phthalocyanines. *Eur. J. Inorg. Chem.* **2007**, *2007*, 4615–4620.

(117) Koyama, T.; Suzuki, T.; Hanabusa, K.; Shirai, H.; Kobayashi, N. A comparison of the loop-current effect of silicon phthalocyanine and silicon naphthalocyanine rings on their axial ligands. *Inorganica Chimica Acta* **1994**, *218*, 41–45.

(118) Janson, T. R.; Kane, A. R.; Sullivan, J. F.; Knox, K.; Kenney, M. E. Ring-current effect of the phthalocyanine ring. *J. Am. Chem. Soc.* **1969**, *91*, 5210–5214.

(119) Davison, J. B.; Wynne, K. J. Silicon phthalocyanine-siloxane polymers: Synthesis and 1H nuclear magnetic resonance study. *Macromolecules* **1978**, *11*, 186–191.

(120) Palacios, R. E.; Kodis, G.; Herrero, C.; Ochoa, E. M.; Gervaldo, M.; Gould, S. L.; Kennis, J. T. M.; Gust, D.; Moore, T. A.; Moore, A. L. Tetrapyrrole Singlet Excited State Quenching by Carotenoids in an Artificial Photosynthetic Antenna †. *J Phys Chem B* **2006**, *110*, 25411–25420.

(121) Zhao, Z.; Cammidge, A. N.; Hughes, D. L.; Cook, M. J. Modular Face-to-Face Assembly of Multichromophore Arrays That Absorb Across the Complete UV−Visible Spectrum and into the Near-IR. *Org. Lett.* **2010**, *12*, 5138–5141.

(122) Dürr, M.; Rosselli, S.; Yasuda, A.; Nelles, G. Band-Gap Engineering of Metal Oxides for Dye-Sensitized Solar Cells. *J Phys Chem B* **2006**, *110*, 21899–21902.

(123) Anderson, N. A.; Lian, T. Ultrafast electron transfer at the molecule-semiconductor nanoparticle interface. *Annu Rev Phys Chem* **2005**, *56*, 491–519.

(124) Argazzi, R.; Iha, N. Y. M.; Zabri, H.; Odobel, F.; Bignozzi, C. A. *Coord. Chem. Rev.* **2004**, *248*, 1299.

(125) Neouze, M. A.; Schubert, U. *Monatsh. Chem.* **2008**, *139*, 183.

(126) Stipkala, J. M.; Castellano, F. N.; Heimer, T. A.; Kelly, C. A.; Livi, K. J. T.; Meyer, G. J. *Chem. Mater.* **1997**, *9*, 2341.

(127) Zhang, J. Z. *J Phys Chem B* **2000**, *104*, 7239.

(128) Zhang, Y. Y.; Galoppini, E. *ChemSusChem* **2010**, *3*, 410.

(129) Clifford, J. N.; Martinez-Ferrero, E.; Viterisi, A.; Palomares, E. *Chem. Soc. Rev.* **2011**, *40*, 1635.

(130) Grätzel, M. *J. Photochem. Photobiol., C* **2003**, *4*, 145.

(131) Grätzel, M. *Acc. Chem. Res.* **2009**, *42*, 1788.

(132) Hagfeldt, A.; Boschloo, G.; Sun, L. C.; Kloo, L.; Pettersson, H. *Chem. Rev.* **2010**, *110*, 6595.

(133) Listorti, A.; O'Regan, B.; Durrant, J. R. *Chem. Mater.* **2011**, *23*, 3381.

(134) Escalada, J. P.; Pajares, A.; Gianotti, J.; Massad, W. A.; Bertolotti, S.; Amat-

Guerri, F.; Garcia, N. A. *Chemosphere* **2006**, *65*, 237.

(135) Henderson, M. A. *Surf. Sci. Rep.* **2011**, *66*, 185.

(136) Jin, Z. L.; Zhang, X. J.; Lu, G. X.; Li, S. B. *J. Mol. Catal. A: Chem.* **2006**, *259*, 275.

(137) Kamat, P. V. *Prog. React. Kinet.* **1994**, *19*, 277.

(138) Kumar, S. G.; Devi, L. G. *J. Phys. Chem. A* **2011**, *115*, 13211.

(139) Pei, D. H.; Luan, J. F. *Int. J. Photoenergy* **2012**.

(140) Beltran-Perez, G.; Lopez-Huerta, F.; Munoz-Aguirre, S.; Castillo-Mixcoatl, J.; Palomino-Merino, R.; Lozada-Morales, R.; Portillo-Moreno, O. *Sens. Actuators, B* **2006**, *120*, 74.

(141) Stux, A. M.; Meyer, G. J. *J. Fluoresc.* **2002**, *12*, 419.

(142) Tokudome, H.; Yamada, Y.; Sonezaki, S.; Ishikawa, H.; Bekki, M.; Kanehira, K.; Miyauchi, M. *Appl. Phys. Lett.* **2005**, *87*, 213901.

(143) Yimit, A.; Itoh, K.; Murabayashi, M. *Sens. Actuators, B* **2003**, *88*, 239.

(144) Yusoff, N. H.; Salleh, M. M.; Yahaya, M. *Sains Malays.* **2008**, *37*, 249.

(145) Anderson, N. A.; Lian, T. Q. *Annu Rev Phys Chem* **2005**, *56*, 491.

(146) Gundlach, L.; Ernstorfer, R.; Willig, F. *Prog. Surf. Sci.* **2007**, *82*, 355.

(147) Hilgendorff, M.; Sundström, V. *J Phys Chem B* **1998**, *102*, 10505.

(148) Katoh, R.; Furube, A.; Barzykin, A. V.; Arakawa, H.; Tachiya, M. *Coord. Chem. Rev.* **2004**, *248*, 1195.

(149) Prezhdo, O. V.; Duncan, W. R.; Prezhdo, V. V. *Acc. Chem. Res.* **2008**, *41*, 339.

(150) Stergiopoulos, T.; Bernard, M. C.; Goff, A. H. L.; Falaras, P. *Coord. Chem. Rev.* **2004**, *248*, 1407.

(151) Bell, T. D. M.; Pagba, C.; Myahkostupov, M.; Hofkens, J.; Piotrowiak, P. *J Phys Chem B* **2006**, *110*, 25314.

(152) Durrant, J. R.; Haque, S. A.; Palomares, E. *Coord. Chem. Rev.* **2004**, *248*, 1247.

(153) Haque, S. A.; Palomares, E.; Cho, B. M.; Green, A. N. M.; Hirata, N.; Klug, D. R.; Durrant, J. R. *J. Am. Chem. Soc.* **2005**, *127*, 3456.

(154) Tachibana, Y.; Nazeeruddin, M. K.; Grätzel, M.; Klug, D. R.; Durrant, J. R. *Chem. Phys.* **2002**, *285*, 127.

(155) Anandan, S.; Yoon, M. *Spectrochim. Acta, Part A* **2004**, *60*, 885.

(156) Chen, C.; Qi, X.; Zhou, B. *J. Photochem. Photobiol., A* **1997**, *109*, 155.

(157) He, J.; Chen, F.; Zhao, J.; Hidaka, H. *Colloids Surf., A* **1998**, *142*, 49.

(158) He, J.; Zhao, J.; Shen, T.; Hidaka, H.; Serpone, N. Photosensitization of Colloidal Titania Particles by Electron Injection from an Excited Organic Dye−Antennae Function. *J Phys Chem B* **1997**, *101*, 9027–9034.

(159) Huang, H.; Zhou, J.; Zhou, Y.; Feng, Y. *Int. J. Photoenergy* **2010**, *2010*, 1.

(160) Huber, R.; Moser, J. E.; Grätzel, M.; Wachtveitl, J. *Chem. Phys.* **2002**, *285*, 39.

(161) Joselevich, E.; Willner, I. *J. Phys. Chem.* **1994**, *98*, 7628.

(162) Kamat, P. V.; Chauvet, J. P.; Fessenden, R. W. *J. Phys. Chem.* **1986**, *90*, 1389.

(163) Kamat, P. V.; Fox, M. A. *Chem. Phys. Lett.* **1983**, *102*, 379.

(164) Kathiravan, A.; Anbazhagan, V.; Asha Jhonsi, M.; Renganathan, R. *Spectrochim. Acta, Part A* **2008**, *70*, 615.

(165) Kathiravan, A.; Chandramohan, M.; Renganathan, R.; Sekar, S. *Spectrochim. Acta, Part A* **2009**, *71*, 1783.

(166) Kathiravan, A.; Chandramohan, M.; Renganathan, R.; Sekar, S. *Spectrochim. Acta, Part A* **2009**, *72*, 496.

(167) Kathiravan, A.; Kumar, P. S.; Renganathan, R.; Anandan, S. *Colloids Surf., A* **2009**, *333*, 175.

(168) Kathiravan, A.; Renganathan, R. *Spectrochim. Acta, Part A* **2008**, *71*, 1106.

(169) Kathiravan, A.; Renganathan, R. *Spectrochim. Acta, Part A* **2008**, *71*, 1080.

(170) Kathiravan, A.; Renganathan, R. *J Colloid Interface Sci* **2009**, *331*, 401.

(171) Moser, J.; Graetzel, M. *J. Am. Chem. Soc.* **1984**, *106*, 6557.

(172) Prashant, K., V *J. Photochem.* **1985**, *28*, 513.

(173) Qu, P.; Zhao, J.; Zang, L.; Shen, T.; Hidaka, H. *Colloids Surf., A* **1998**, *138*, 39.

(174) Rath, M. C.; Palit, D. K.; Mukherjee, T.; Ghosh, H. N. *J. Photochem. Photobiol., A* **2009**, *204*, 209.

(175) Sant, P. A.; Kamat, P. V. *Phys. Chem. Chem. Phys.* **2002**, *4*, 198.

(176) Walters, K. A.; Gaal, D. A.; Hupp, J. T. *J Phys Chem B* **2002**, *106*, 5139.

(177) Wang, C. Y.; Liu, C. Y.; Wang, W. Q.; Shen, T. *J. Photochem. Photobiol., A* **1997**, *109*, 159.

(178) Wang, C. Y.; Liu, C. Y.; Wang, Y.; Shen, T. *J Colloid Interface Sci* **1998**, *197*, 126.

(179) Wu, T.; Xu, S. J.; Shen, J. Q.; Chen, S.; Zhang, M. H.; Shen, T. *J. Photochem. Photobiol., A* **2000**, *137*, 191.

(180) Zang, L.; Liu, C. Y.; Ren, X. M. *J. Photochem. Photobiol., A* **1995**, *88*, 47.

(181) Zang, L.; Qu, P.; Zhao, J.; Shen, T.; Hidaka, H. *Chem. Lett.* **1997**, *26*, 791.

(182) Zhang, H.; Zhou, Y.; Zhang, M.; Shen, T.; Xiang, J.; Feng, J. *J Colloid Interface Sci* **2003**, *263*, 669.

(183) Zhou, Z. X.; Qian, S. P.; Yao, S. D.; Zhang, Z. Y. *Dyes Pigm.* **2001**, *51*, 137.

(184) Zuo, P.; Li, C.; Wu, Y. S.; Ai, X. C.; Wang, X. S.; Zhang, B. W.; Zhang, J. P. *J. Photochem. Photobiol., A* **2006**, *183*, 138.

(185) Avlasevich, Y.; Li, C.; Müllen, K. *J. Mater. Chem.* **2010**, *20*, 3814.

(186) Cappel, U. B.; Karlsson, M. H.; Pschirer, N. G.; Eickemeyer, F.; Schöneboom, J.; Erk, P.; Boschloo, G.; Hagfeldt, A. *J. Phys. Chem. C* **2009**, *113*, 14595.

(187) Edvinsson, T.; Li, C.; Pschirer, N.; Schöneboom, J.; Eickemeyer, F.; Sens, R.; Boschloo, G.; Herrmann, A.; Müllen, K.; Hagfeldt, A. *J. Phys. Chem. C* **2007**, *111*, 15137.

(188) Ferrere, S.; Gregg, B. A. *New J. Chem.* **2002**, *26*, 1155.

(189) Ferrere, S.; Zaban, A.; Gregg, B. A. *J Phys Chem B* **1997**, *101*, 4490.

(190) Fortage, J.; Séverac, M.; Houarner-Rassin, C.; Pellegrin, Y.; Blart, E.; Odobel, F. *J. Photochem. Photobiol., A* **2008**, *197*, 156.

(191) Li, C.; Liu, Z.; Schöneboom, J.; Eickemeyer, F.; Pschirer, N. G.; Erk, P.; Herrmann, A.; Müllen, K. *J. Mater. Chem.* **2009**, *19*, 5405.

(192) Li, C.; Yum, J. H.; Moon, S. J.; Herrmann, A.; Eickemeyer, F.; Pschirer, N. G.; Erk, P.; Schöneboom, J.; Müllen, K.; Grätzel, M. *ChemSusChem* **2008**, *1*, 573.

(193) Mathew, S.; Imahori, H. *J. Mater. Chem.* **2011**, *21*, 7166.

(194) Planells, M.; Céspedes-Guirao, F. J.; Forneli, A.; Sastre-Santos, Á.; Fernández-Lázaro, F.; Palomares, E. Interfacial photo-induced charge transfer reactions in perylene imide dye sensitised solar cells. *J. Mater. Chem.* **2008**, *18*, 5802–5808.

(195) Shibano, Y.; Umeyama, T.; Matano, Y.; Imahori, H. Electron-Donating Perylene Tetracarboxylic Acids for Dye-Sensitized Solar Cells. *Org. Lett.* **2007**, *9*, 1971–1974.

(196) Szarko, J. M.; Neubauer, A.; Bartelt, A.; Socaciu-Siebert, L.; Birkner, F.; Schwarzburg, K.; Hannappel, T.; Eichberger, R. *J. Phys. Chem. C* **2008**, *112*, 10542.

(197) Planells, M.; Cespedes-Guirao, F. J.; Forneli, A.; Sastre-Santos, A.; Fernandez-Lazaro, F.; Palomares, E. *J. Mater. Chem.* **2008**, *18*, 5802.

(198) Shibano, Y.; Umeyama, T.; Matano, Y.; Imahori, H. *Org. Lett.* **2007**, *9*, 1971.

(199) Nilsing, M.; Persson, P.; Lunell, S.; Ojamae, L. *J. Phys. Chem. C* **2007**, *111*, 12116.

(200) Liu, H. B.; Xu, J. L.; Li, Y. J.; Li, Y. L. *Acc. Chem. Res.* **2010**, *43*, 1496.

(201) Liu, H. B.; Zuo, Z. C.; Guo, Y. B.; Li, Y. J.; Li, Y. L. *Angew. Chem. Int. Ed.* **2010**, *49*, 2705.

(202) Zheng, H. Y.; Li, Y. J.; Liu, H. B. A.; Yin, X. D.; Li, Y. L. *Chem. Soc. Rev.* **2011**, *40*, 4506.

(203) Dubey, R. K.; Efimov, A.; Lemmetyinen, H. *Chem. Mater.* **2011**, *23*, 778.

(204) Kohl, C.; Weil, T.; Qu, J. Q.; Müllen, K. *Chem. Eur. J.* **2004**, *10*, 5297.

(205) Crans, D. C.; Levinger, N. E. *Acc. Chem. Res.* **2012**, *45*, 1637.

(206) Lakowicz, J. R. *Principles of Fluorescence Spectroscopy*; 3, Ed. 2006.

(207) Rasband, W. S. *ImageJ*; 1997.

(208) Frisch, M. J.; Trucks, G. W.; Schlegel, H. B.; Scuseria, G. E.; Robb, M. A.; Cheeseman, J. R.; Scalmani, G.; Barone, V.; Mennucci, B.; Petersson, G. A. *Gaussian 09*; 2009.

(209) Fukuda, T.; Homma, S.; Kobayashi, N. *Chem. Eur. J.* **2005**, *11*, 5205.

(210) Mack, J.; Asano, Y.; Kobayashi, N.; Stillman, M. J. *J. Am. Chem. Soc.* **2005**, *127*, 17697.

(211) Mack, J.; Bunya, M.; Lansky, D.; Goldberg, D. P.; Kobayashi, N. *Heterocycles* **2008**, *76*, 1369.

(212) Clark, A. E.; Qin, C. Y.; Li, A. D. Q. *J. Am. Chem. Soc.* **2007**, *129*, 7586.

(213) Francl, M. M.; Pietro, W. J.; Hehre, W. J.; Binkley, J. S.; Gordon, M. S.; Defrees, D. J.; Pople, J. A. *J. Chem. Phys.* **1982**, *77*, 3654.

(214) Harihan, P. C.; Pople, J. A. *Theor. Chim. Acta* **1973**, *28*, 213.

(215) Rassolov, V. A.; Pople, J. A.; Ratner, M. A.; Windus, T. L. *J. Chem. Phys.* **1998**, *109*, 1223.

(216) Shibano, Y.; Imahori, H.; Adachi, C. *J. Phys. Chem. C* **2009**, *113*, 15454.

(217) Barone, V.; Cossi, M. *J. Phys. Chem. A* **1998**, *102*, 1995.

(218) Cossi, M.; Rega, N.; Scalmani, G.; Barone, V. *J. Comput. Chem.* **2003**, *24*, 669.

(219) Weng, Y. X.; Li, L.; Liu, Y.; Wang, L.; Yang, G. Z. *J Phys Chem B* **2003**, *107*, 4356.

(220) Sakata, T.; Hashimoto, K.; Hiramoto, M. *J. Phys. Chem.* **1990**, *94*, 3040.

(221) Redmond, G.; Fitzmaurice, D. *J. Phys. Chem.* **1993**, *97*, 1426.

(222) Wang, Y.; Herron, N. *J. Phys. Chem.* **1991**, *95*, 525.

(223) Bawendi, M. G.; Steigerwald, M. L.; Brus, L. E. *Annu Rev Phys Chem* **1990**,

41, 477.

(224) Monticone, S.; Tufeu, R.; Kanaev, A. V.; Scolan, E.; Sanchez, C. *Appl. Surf. Sci.* **2000**, *162–163*, 565.

(225) Kaniyankandy, S.; Ghosh, H. N. *J. Mater. Chem.* **2009**, *19*, 3523.

(226) Vayssieres, L.; Persson, C.; Guo, J. H. *Appl. Phys. Lett.* **2011**, 99.

(227) Hegazy, A.; Prouzet, E. *Chem. Mater.* **2012**, *24*, 245.

(228) Yacaman, M. J.; Ascencio, J. A.; Liu, H. B.; Gardea-Torresdey, J. *J. Vac. Sci. Technol., B* **2001**, *19*, 1091.

(229) Falaras, P. *Sol. Energy Mater. Sol. Cells* **1998**, *53*, 163.

(230) Finnie, K. S.; Bartlett, J. R.; Woolfrey, J. L. *Langmuir* **1998**, *14*, 2744.

(231) Neubauer, A.; Szarko, J. M.; Bartelt, A. F.; Eichberger, R.; Hannappel, T. *J. Phys. Chem. C* **2011**, *115*, 5683.

(232) Pankove, J. I. *Optical Processes in Semiconductors*; 2010.

(233) Atik, S. S.; Thomas, J. K. *J. Am. Chem. Soc.* **1981**, *103*, 3543.

(234) Stockwell, D.; Yang, Y.; Huang, J.; Anfuso, C.; Huang, Z. Q.; Lian, T. Q. *J. Phys. Chem. C* **2010**, *114*, 6560.

(235) Gao, Y. Q.; Georgievskii, Y.; Marcus, R. A. *J. Chem. Phys.* **2000**, *112*, 3358.

(236) Ai, X.; Anderson, N. A.; Guo, J. C.; Lian, T. Q. *J Phys Chem B* **2005**, *109*, 7088.

(237) Ai, X.; Guo, J. C.; Anderson, N. A.; Lian, T. Q. *J Phys Chem B* **2004**, *108*, 12795.

(238) Lundqvist, M. J.; Nilsing, M.; Lunell, S.; Akermark, B.; Persson, P. *J Phys Chem B* **2006**, *110*, 20513.

(239) Hernández, L. I.; Godin, R.; Bergkamp, J. J.; Llansola Portolés, M. J.; Sherman, B. D.; Tomlin, J.; Kodis, G.; Méndez-Hernández, D. D.; Bertolotti, S.; Chesta, C. A.; Mariño-Ochoa, E.; Moore, A. L.; Moore, T. A.; Cosa, G.; Palacios, R. E. Spectral Characteristics and Photosensitization of TiO 2Nanoparticles in Reverse Micelles by Perylenes. *J Phys Chem B* **2013**, *117*, 4568–4581.

(240) Grätzel, M. Recent Advances in Sensitized Mesoscopic Solar Cells. *Acc. Chem. Res.* **2009**, *42*, 1788–1798.

(241) Anikeeva, P.; Madigan, C.; Halpert, J.; Bawendi, M.; Bulović, V. Electronic and excitonic processes in light-emitting devices based on organic materials and colloidal quantum dots. *Phys. Rev. B* **2008**, *78*, 085434.

(242) ZHU, X. Electronic structure and electron dynamics at molecule?metal interfaces: implications for molecule-based electronics. *Surface Science Reports* **2004**, *56*, 1–83.

(243) Lindstrom, C. D.; Zhu, X.-Y. Photoinduced electron transfer at molecule-metal interfaces. *Chem. Rev.* **2006**, *106*, 4281–4300.

(244) Zhu, X.-Y. Charge Transport at Metal−Molecule Interfaces: A Spectroscopic View. *J Phys Chem B* **2004**, *108*, 8778–8793.

(245) Coropceanu, V.; Cornil, J.; da Silva Filho, D. A.; Olivier, Y.; Silbey, R.; Brédas, J.-L. Charge transport in organic semiconductors. *Chem. Rev.* **2007**, *107*, 926–952.

(246) Tulevski, G. S.; Myers, M. B.; Hybertsen, M. S.; Steigerwald, M. L.; Nuckolls, C. Formation of catalytic metal-molecule contacts. *Science* **2005**, *309*, 591–594.

(247) Moser, J.; Graetzel, M. Photosensitized electron injection in colloidal semiconductors. *J. Am. Chem. Soc.* **1984**, *106*, 6557–6564.

(248) Li, C.; Yum, J.-H.; Moon, S.-J.; Herrmann, A.; Eickemeyer, F.; Pschirer, N. G.; Erk, P.; Schöneboom, J.; Müllen, K.; Grätzel, M.; Nazeeruddin, M. K. An improved perylene sensitizer for solar cell applications. *ChemSusChem* **2008**, *1*, 615–618.

(249) Shibano, Y.; Imahori, H.; Adachi, C. Organic Thin-Film Solar Cells Using Electron-Donating Perylene Tetracarboxylic Acid Derivatives. *J. Phys. Chem. C* **2009**, *113*, 15454–15466.

(250) Mutin, P. H.; Vioux, A. Nonhydrolytic Processing of Oxide-Based Materials: Simple Routes to Control Homogeneity, Morphology, and Nanostructure. *Chem. Mater.* **2009**, *21*, 582–596.

(251) Arnal, P.; Corriu, R. J. P.; Leclercq, D.; Mutin, P. H.; Vioux, A. A Solution Chemistry Study of Nonhydrolytic Sol−Gel Routes to Titania. *Chem. Mater.* **1997**, *9*, 694–698.

(252) Vioux, A. Nonhydrolytic Sol−Gel Routes to Oxides. *Chem. Mater.* **1997**, *9*, 2292–2299.

(253) Nilsing, M.; Persson, P.; Lunell, S.; Ojamäe, L. Dye-Sensitization of the TiO2 Rutile (110) Surface by Perylene Dyes: Quantum-Chemical Periodic B3LYP Computations. *J. Phys. Chem. C* **2007**, *111*, 12116–12123.

(254) Weng, Y.-X.; Li, L.; Liu, Y.; Wang, L.; Yang, G.-Z. Surface-Binding Forms of Carboxylic Groups on Nanoparticulate TiO2 Surface Studied by the Interface-Sensitive Transient Triplet-State Molecular Probe. *J Phys Chem B* **2003**, *107*, 4356–4363.

(255) Redmond, G.; Fitzmaurice, D. Spectroscopic determination of flatband potentials for polycrystalline titania electrodes in nonaqueous solvents. *J. Phys. Chem.* **1993**, *97*, 1426–1430.

(256) Edvinsson, T.; Li, C.; Pschirer, N.; Schöneboom, J.; Eickemeyer, F.; Sens, R.; Boschloo, G.; Herrmann, A.; Müllen, K.; Hagfeldt, A. Intramolecular Charge-Transfer Tuning of Perylenes: Spectroscopic Features and Performance in Dye-Sensitized Solar Cells. *J. Phys. Chem. C* **2007**, *111*, 15137–15140.

(257) Ferrere, S.; Gregg, B. A. New perylenes for dye sensitization of TiO2. *New J. Chem.* **2002**, *26*, 1155–1160.

(258) Fortage, J.; Séverac, M.; Houarner-Rassin, C.; Pellegrin, Y.; Blart, E.; Odobel, F. Synthesis of new perylene imide dyes and their photovoltaic performances in nanocrystalline TiO2 dye-sensitized solar cells. *Journal of Photochemistry and Photobiology A: Chemistry* **2008**, *197*, 156–169.

(259) Li, C.; Liu, Z.; Schöneboom, J.; Eickemeyer, F. Perylenes as sensitizers in hybrid solar cells: how molecular size influences performance. *Journal of Materials …* **2009**.

(260) Sakata, T.; Hashimoto, K.; Hiramoto, M. New aspects of electron transfer on semiconductor surface: dye-sensitization system. *J. Phys. Chem.* **1990**, *94*, 3040–3045.

(261) Stockwell, D.; Yang, Y.; Huang, J.; Anfuso, C.; Huang, Z.; Lian, T. Comparison of Electron-Transfer Dynamics from Coumarin 343 to TiO2, SnO2, and ZnO Nanocrystalline Thin Films: Role of Interface-Bound Charge-Separated Pairs. *J. Phys. Chem. C* **2010**, *114*, 6560–6566.

(262) Gao, Y. Q.; Georgievskii, Y.; Marcus, R. A. On the theory of electron transfer reactions at semiconductor electrode/liquid interfaces. *The Journal of Chemical Physics* **2000**, *112*, 3358–3369.

(263) Ai, X.; Anderson, N. A.; Guo, J.; Lian, T. Electron injection dynamics of Ru polypyridyl complexes on SnO2 nanocrystalline thin films. *J Phys Chem B* **2005**, *109*, 7088–7094.

(264) Ai, X.; Guo, J.; Anderson, N. A.; Lian, T. Ultrafast Electron Transfer from Ru Polypyridyl Complexes to Nb2O5 Nanoporous Thin Films. *J Phys Chem B* **2004**, *108*, 12795–12803.

(265) Kuciauskas, D.; Freund, M. S.; Gray, H. B.; Winkler, J. R.; Lewis, N. S. Electron Transfer Dynamics in Nanocrystalline Titanium Dioxide Solar Cells Sensitized with Ruthenium or Osmium Polypyridyl Complexes. *J Phys Chem B* **2001**, *105*, 392–403.

(266) Laha, J. K.; Dhanalekshmi, S.; Taniguchi, M.; Ambroise, A.; Lindsey, J. S. A Scalable Synthesis of Meso-Substituted Dipyrromethanes. *Org. Process Res. Dev.* **2003**, *7*, 799–812.

(267) Cook, M. J.; Heeney, M. J. Phthalocyaninodehydroannulenes. *Chemistry* **2000**, *6*, 3958–3967.

(268) Minkenberg, C. B.; Florusse, L.; Eelkema, R.; Koper, G. J. M.; van Esch, J. H. Triggered Self-Assembly of Simple Dynamic Covalent Surfactants. *J. Am. Chem. Soc.* **2009**, *131*, 11274–11275.

(269) Yamaguchi, H.; Tsubouchi, K.; Kawaguchi, K.; Horita, E.; Harada, A. Peroxidase Activity of Cationic Metalloporphyrin-Antibody Complexes. *Chem. Eur. J.* **2004**, *10*, 6179–6186.

APPENDIX A

OVERSIZED FIGUERS & TABLES

Table 1. Final charge separated state lifetimes, quantum yield for the formation of the final charge separated state, and experimental conditions for selected artificial reaction centers.

Compound	Solvent	τ[a]	Φ[a]	$\lambda_{excitation}$ (nm)	Reference
1	dichloromethane	170 ns	0.04	600	Moore et al. 1984
	dichloromethane[b]	2.5 μs	0.25	600	Moore et al. 1984
2	2-methyltetrahydrofuran	60 ns	0.96	590	Bahr et al. 2000
3	2-methyltetrahydrofuran	57 ns	0.95	600	Kodis et al. 2004
4	2-methyltetrahydrofuran	170 ns	0.14	590	Liddell et al. 1997
	2-methyltetrahydrofuran[c]	1.5 μs	0.10	590	Liddell et al. 1997
5	2-methyltetrahydrofuran	340 ns	0.88	590	Kuciauskas et al. 2000
6	2-methyltetrahydrofuran	1.3 ns	0.69	560	Kuciauskas et al. 1999
7	2-methyltetrahydrofuran	240 ns	0.86	560	Kodis et al. 2002
8[d]	2-methyltetrahydrofuran	8.9 ns	0.80	480	Kodis et al. 2006
8[e]	2-methyltetrahydrofuran	15.3 ns	0.96	480	Kodis et al. 2006
9	1,2-difluorobenzene	230 ps	~1	480	Terazono et al. 2009
11	benzonitrile	3.8 μs	0.52	740	Megiatto et al. 2012

[a] lifetime and quantum yield given for the final charge separated state of the respective reaction center

[b] saturated with tetra-n-butylammonium tetrafluoroborate

[c] 77 K (all other values in table at room temperature)

[d] M = 2H (freebase form, see Fig. 5)

[e] M = Zn (Zn inserted form, see Fig. 5)

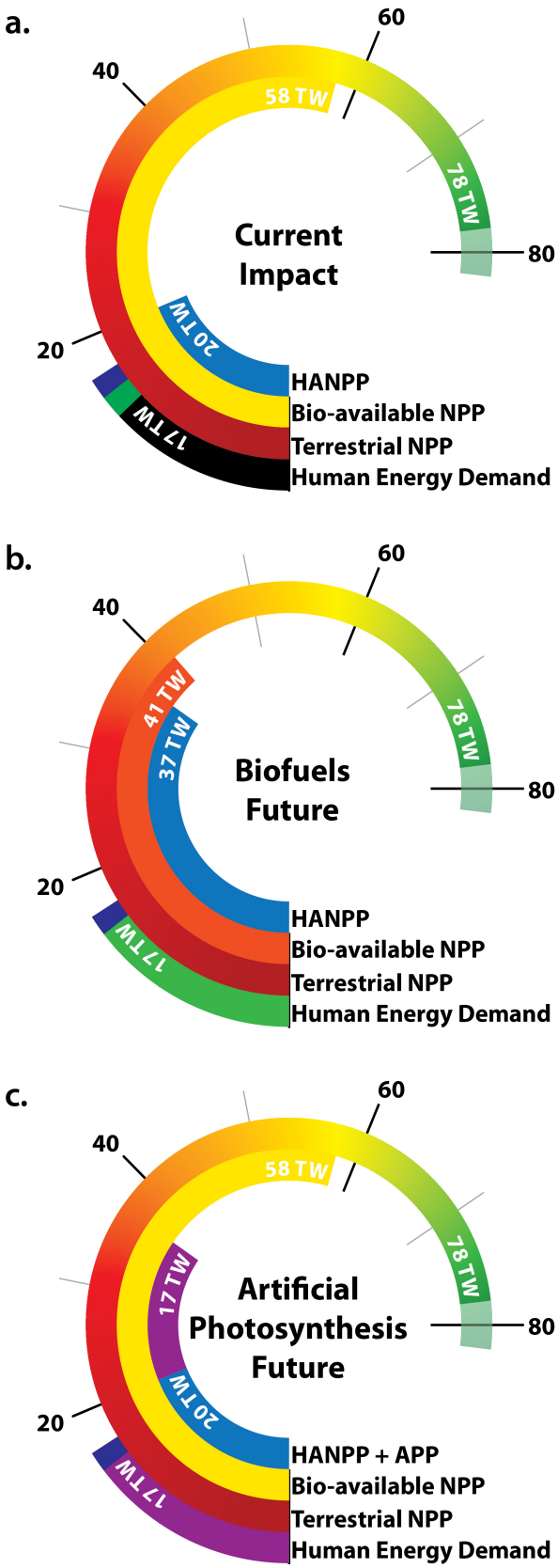
a.
60
40
58 TW
78 TW
80
Current
Impact
20
20 TW
17 TW
HANPP
Bio-available NPP
Terrestrial NPP
Human Energy Demand
b.
60
40
41 TW
37 TW
78 TW
80
Biofuels
Future
20
17 TW
HANPP
Bio-available NPP
Terrestrial NPP
Human Energy Demand
c.
60
40
58 TW
78 TW
17 TW
Artificial
Photosynthesis
Future
80
20
20 TW
17 TW
HANPP + APP
Bio-available NPP
Terrestrial NPP
Human Energy Demand

Figure 2: Impact of human society on the NPP and the biosphere. a.) Current impact of human society. NPP is estimated from a consensus of recent models [45] (NPP prior to industrialization is indicated by the shaded extension to 82 TW) and transformed into TW using a previous conversion [49]. HANPP is indicated relative to the amount remaining for all biota [49]. Human energy demands are met using primarily fossil reserves (black fill), while current renewable sources are designated as renewable biofuels (green fill) and renewable nonbiofuels (dark blue fill) [51]. b.) Future scenario with complete replacement of fossil fuels by biofuels (green fill), bioavailable NPP is reduced by half, which has catastrophic effects on biodiversity. c.) Future scenario with NPP enhanced by higher efficiency APP deployed within existing footprint of human society, purple fill indicates enhancements to productivity from APP.

APPENDIX B

COPYRIGHTS & PERMISSIONS

Chapter 1: Journal Name: Photosynthesis Research

Sherman, B. D.; Vaughn, M. D.; Bergkamp, J. J.; Gust, D.; Moore, A. L.; Moore, T. A. Evolution of reaction center mimics to systems capable of generating solar fuel. *Photosyn. Res.* **2013**, 1–12.

RightsLink License Number: 3141020905716

Chapter 2: Journal Name: Canadian Journal of Chemistry

Sherman, B. D.; Pillai, S.; Kodis, G.; Bergkamp, J.; Mallouk, T. E.; Gust, D.; Moore, T. A.; Moore, A. L. A porphyrin-stabilized iridium oxide water oxidation catalyst. *Can. J. Chem.* **2011**, *89*, 152–157.

Chapter 3: Journal Name: Journal of Porphyrins and Phthalocyanines

Bergkamp, J. J.; Sherman, B. D.; Mariño-Ochoa, E.; Palacios, R. E.; Cosa, G.; Moore, T. A.; Gust, D.; Moore, A. L. Synthesis and characterization of silicon phthalocyanines bearing axial phenoxyl groups for attachment to semiconducting metal oxides. *J. Porphyrins Phthalocyanines* **2011**, *15*, 943–950.

Chapter 4.1: Journal Name: The Journal of Physical Chemistry B

Hernández, L. I.; Godin, R.; Bergkamp, J. J.; Llansola Portolés, M. J.; Sherman, B. D.; Tomlin, J.; Kodis, G.; Méndez-Hernández, D. D.; Bertolotti, S.; Chesta, C. A.; Mariño-Ochoa, E.; Moore, A. L.; Moore, T. A.; Cosa, G.; Palacios, R. E. Spectral Characteristics and Photosensitization of TiO

$_2$Nanoparticles in Reverse Micelles by Perylenes. *J Phys Chem B* **2013**, *117*, 4568–4581.

Chapter 4.2: Journal Name: Photochemistry and Photobiology

Manuel J. Llansola-Portoles, Jesse J. Bergkamp, John Tomlin, Thomas A. Moore, Gerdenis Kodis, Ana L. Moore, Gonzalo Cosa, Rodrigo E Palacios., Photoinduced electron transfer in perylene-TiO_2 nanoassemblies. *J. Photochem. Photobio.*

Publisher: John Wiley and Sons

RightLinks License Number: 3193251165094